PEG-PCL Copolymers Reinstating Human Mesenchymal Stem Cell Potency: Study of Structure-Function Relationship

By

Daniel A. Balikov

Dissertation
Submitted to the Faculty of the
Graduate School of Vanderbilt University
in partial fulfillment of the requirements
for the degree of

DOCTOR OF PHILOSOPHY
in

Biomedical Engineering
May, 2017
Nashville, Tennessee

Approved:

Hak-Joon Sung, Ph.D.

Todd D. Giorgio, Ph.D., P.E.

Justin H. Turner, M.D., Ph.D.

Matthew J. Lang, Ph.D.

Aaron B. Bowman, Ph.D.

DEDICATION

The foundation of every state is the education of its youth.

~ Diogenes

To the greatest generation:

Melvin H. Balikov, Ph.D. (May 3, 1923 – March 5, 2000)

Helen Balikov (July 24, 1924 – December 8, 2014)

Harriett Rosenberg (May 10, 1918 – February 6, 2004)

William Rosenberg, M.D. (May 10, 1915 -)

ACKNOWLEDGEMENTS

Three years can seem like a long time when immersed in the crucible of research. Through thick and thin, I would not be where I am today without having the ability to lean on others for guidance and assistance, nor able to enjoy the adventure that is graduate school without my friends and colleagues.

First and foremost I thank my thesis advisor, Dr. Hak-Joon Sung for taking the risk of accepting me into his lab, entrusting me with a key project in his portfolio, and imparting the knowledge and experience I have absorbed.

I also thank my committee members, Dr. Todd Giorgio, Dr. Justin Turner, Dr. Matthew Lang, and Dr. Aaron Bowman for the continued guidance and collaboration. In addition, I acknowledge my terrific collaborators Dr. Sanjeeva Murthy, Dr. Dylan Burnett, Aidan Fenix, Dr. Pampee Young, Dr. Kirill Bolotin, Dr. Dhiraj Prasai, Isaac Pence, and Sonia Brady.

Moreover, it has been an honor to work in the trenches with fellow labmates Dr. Mukesh Gupta, Dr. Xintong Wang, Dr. Young Wook Chun, Dr. Jung Bok Lee, Dr. Kellye Kirkbride, Dr. Charleson Bell, Dr. Eric Dailing, Dr. Brian Evans, Dr. Chris Nelson, Dr. Lucas Hofmeister, Dr. Sue Lee, Dr. Kelsey Mayo, Ricky Rath, Tim Boire, John Martin, Sammy Sarett, Kameron Kilchrist, Thomas Werfel, Taylor Kavanaugh, Meredith Jackson, Bryan Dollinger, Sean Bedingfield, Sinead Miller and Stephanie Dudzinski.

I also want to thank the Vanderbilt Medical Scientist Training Program, Vanderbilt University School of Engineering, Vanderbilt University Graduate School, the

American Heart Association, the National Science Foundation, and the National Institutes of Health for financially supporting this work.

I also thank Dr. Spencer W. Crowder for taking me under his wing when I began, continually collaborating during and after his Vanderbilt tenure, and being a wonderful friend with whom I share a deep appreciation of his life experience, his scientific mind and his unwavering friendship.

Finally, I thank my family. To my parents, Lisa and Howard, and my brother, Robby, the greatest cheerleaders I could ever have. You are all second-to-none.

TABLE OF CONTENTS

Page

LIST OF TABLES

LIST OF EQUATIONS

LIST OF FIGURES

Chapter 1: Introduction and Motivation

Tissue engineering as a platform technology could revolutionize how medical professionals approach combating and treating disease. With evolutionary biology and human physiology serving as the backdrop, the known ability for organisms to heal, or even regenerate, themselves has inspired physicians and scientists to believe that we can better understand these processes and potentially find tools that capitalize on them for clinical application. The field of biomaterials has aimed to address this exact challenge by providing platforms for cells to recreate native structure and function of tissues found in the body.

Biomaterials scientists have the option of employing both naturally-derived and synthetically-derived materials as substrates for two types of cells: somatic cells and stem cells. Both cell types have been found to respond positively to biomaterial technologies. Yet with the accelerating capability of generating any somatic cell type with induced pluripotent stem cells and the ever-improving expertise in harvesting native patient stem cells, the development of biomaterial platforms that promote and maintain a naïve stem cell phenotype is even more appealing. The quintessential stem cell that encapsulates this mindset is the mesenchymal stem cell (**hMSC**), particularly from adipose or bone marrow, as this stem cell variety is easily accessible and present in adults throughout their lifespan.

Many studies have been conducted to learn how material properties alter hMSC phenotype. The majority of these studies try to create micro- and macro-tissues such as cartilage and bone, and translation of these findings have begun to permeate into clinical settings. Yet, far fewer investigations have inquired how biomaterials could recreate stem

cell niches that potentially provide the necessary capabilities of maintaining and expanding stem cell populations outside the body, which is paramount for tissue engineering technologies to have successful impacts on human health. This dissertation project aimed at tackling a small aspect of this problem, namely looking for material compositions that promote hMSC stem cell health for *ex vivo* expansion and probe what the cell-material interface looks like such that future biomaterials can account for new prerequisite design factors. The materials utilized for creating this biomaterial culture platform included polyethylene glycol (**PEG**) and poly(ε-caprolactone) (**PCL**). The following specific aims have been addressed:

Aim 1: Based on preliminary studies, are there any other PEG-PCL copolymer substrates that elicit an improved stemness phenotype in hMSCs compared to a previously identified copolymer composition?

Aim 2: What surface distribution of PEG and PCL is presented by the copolymer compositions that promote the altered phenotype in hMSCs?

Aim 3: Is the increased stemness phenotype of hMSCs reproducible in a larger hMSC donor population, and are there highly responsive cell membrane proteins at the cell-material interface that trigger the phenotype switch?

Aim 4: Can hMSCs be serially passaged on an optimal PEG-PCL copolymer without losing the enhanced stemness phenotype?

Chapter 2: Background

2.1 Human mesenchymal stem cells (**hMSCs**) for Regenerative Medicine

2.1.1 Defining hMSCs and Their Sources

hMSCs were first observed as a subpopulation of bone marrow-derived stromal cells[1] and widely known to undergo directed differentiation[2] into osteogenic,[3-8] chondrogenic,[9-12] and adipogenic[6, 13] lineages. During the same period, however, many studies have continually questioned if hMSCs intrinsically exude a phenotypic plasticity because they have been found in multiple tissue types outside of the bone marrow.[14, 15] (also summarized in Figure 2-1). Hence, the nature and origin of hMSCs are not clear as they change depending on tissue source.

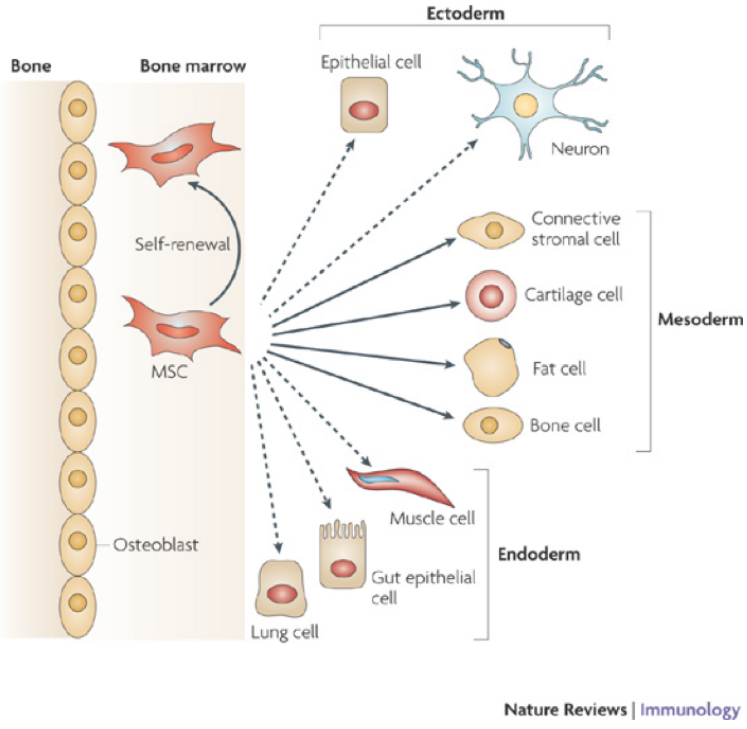

Figure 2-1 Multilineage Potential of hMSCs.
Curved arrow indicates self-renewal. Solid straight arrows represent known mesodermal lineage differentiation while dashed straight arrows represent transdifferentiation into ecto- and endodermal lineages in vitro. Adapted with permission from [16].

Several groups have published findings that adipose tissue, muscle tissue, umbilical cord, synovial fluid, corneal tissue, central nervous system, liver, heart and dental pulp also contain hMSCs.[17-22] Because hMSCs are found in several distinct tissues, the phenotypic markers of hMSCs consequentially overlap with those of other cell types native to the tissue of origin. As a result, the commonly-accepted hMSC profile includes: $CD13^+$, $CD44^+$, $CD49a^+$, $CD49b^+$, $CD63^+$, $CD90^+$, $CD105^+$, $CD146^+$ and $CD11b^-$, $CD34^-$, $CD45^-$, $CD133^-$.[23] Two additional markers that also define undifferentiated, naïve hMSCs from the bone marrow include CD166 and STRO-1.[24, 25]

Moreover, because some of these phenotypic markers overlap with the native tissues hMSCs reside within, the aforementioned differentiation potential these cells have are likely acquired by the surrounding cells and matrix environment.[26-28] This is reflected in the ability of hMSCs to differentiate into mesodermal, ectodermal and endodermal cell lineages, thereby bringing into question is the term 'mesenchymal' is even valid as a scientific label and rather simply historic.[2, 29, 30]

In an effort to try to resolve these contradictions, Nardi and colleagues looked at murine post-natal MSCs to verify tissue origin of MSCs and characterize their long-term culture potential and functional properties.[31] Minimizing contamination from circulating cells in the blood, their findings demonstrated that MSCs are, in fact, found in most all solid organs and within the vessel walls of blood vasculature. MSCs from all the tested solid tissues (brain, spleen, liver, kidney, kidney glomeruli, lung, bone marrow, muscle, thymus and pancreas; examples illustrated in Figure 2-2) were able to generate long-term cultures through self-renewal, but did have differences in surface antigen markers as well as differentiation potential that was likely related to their site of origin.

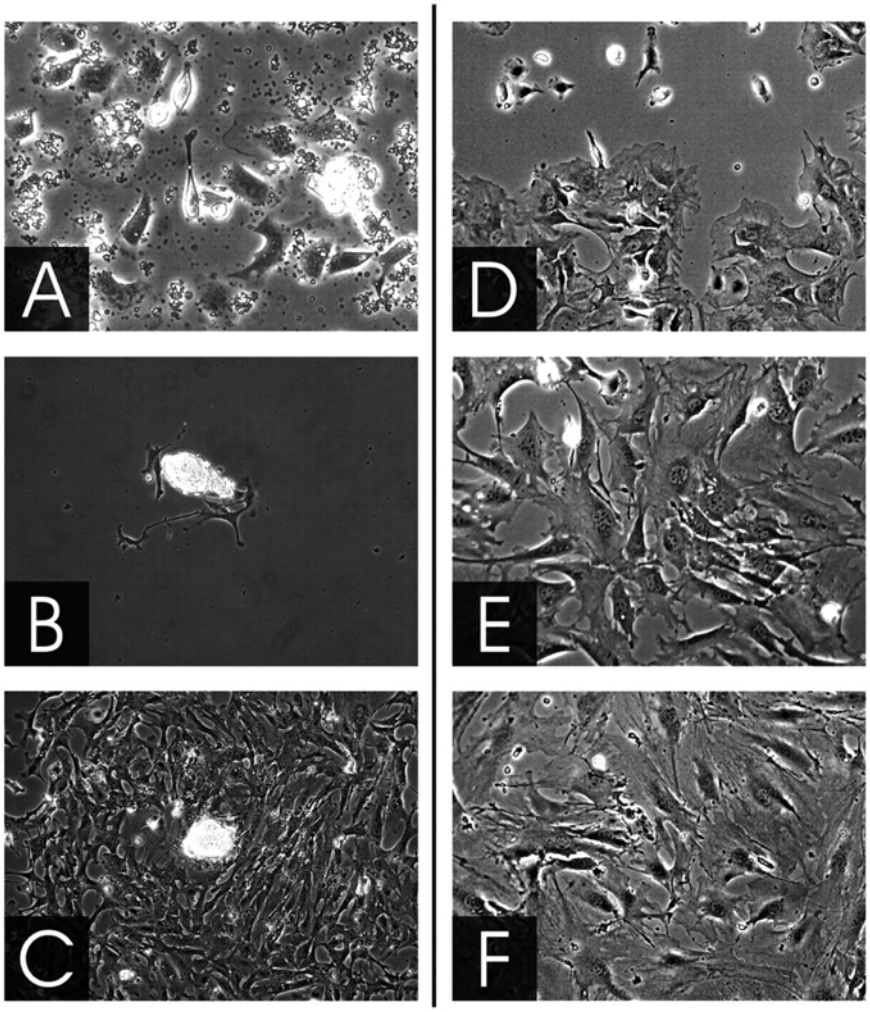

Figure 2-2 Morphology of MSC cultures derived from different organs and tissues. **(A)** Phase-contrast micrographs of MSC-like cells in primary culture of aorta 24 hours after plating. Glomerulus outgrowth on the fourth **(B)** and sixth **(C)** day post-plating. **(D)** Heterogeneity among bone marrow-derived cells at passage 4, with MSC-like cells (lower portion), spindle-shaped and round cells. **(E)** Pancreas-derived MSCs at passage 30. **(F)** Vena-cava-derived MSCs at passage 22. Magnifications, ×100 (B-F); ×200 (A). Reused with permission from [31].

Even with the breadth of this particular study, other groups have contended that cell source of MSCs does play a bigger role in stem cell plasticity, and bone marrow MSCs show the greatest superiority with this respect, which could be speculated as being due to other resident stem cells in the marrow environment.[32] Interestingly, some groups have argued that bone marrow hMSCs can come in two different fractions depending on the method of isolation.[33] However, a more recent study from 2010 vindicated the trends observed by Nardi *et al* where hMSCs from different tissue sources exhibited large transcriptomic variation as well as a few conserved genes.[34] Bone marrow hMSCs were found to have gene networks that contributed more to tissue and organ development in the mesodermal and endodermal lineages, while adipose hMSCs were found to have significantly more immunomodulatory genes. Yet, there will undoubtedly be more follow-up work and contradictory studies given the nebulous nature of this mysterious and powerful stem cell subclass.

2.1.2 hMSCs in Regenerative Medicine and the Issue of the Hayflick Limit

Over the past several decades, hMSCs have become one of the most promising cell sources for regenerative medicine due to their autologous availability, self-renewal capacity, immunomodulatory effects, and multi-lineage differentiation potential.[2] Encouraging results from basic science studies have stimulated a worldwide interest in the use of hMSCs for treating human diseases, and hundreds of clinical trials are currently underway[35, 36] to evaluate their therapeutic efficacy for a range of applications,[36] including attenuation of graft-versus-host disease,[37] Crohn's disease, repair of cardiac tissue following heart attack,[38] protection of tissue in type 1 diabetics, and patients with chronic obstructive pulmonary disease (Osiris Therapeutics, Inc.).

However, despite their promise, scientific consensus regarding the identity, homogeneity, and applicability of this cell type remains elusive, and inherent variations in donor cell quality have further slowed the pace for hMSCs reaching widespread clinical use.[36, 39] The individuals who would gain the most from stem cell-based therapies are typically those of advanced age, and the hMSCs they would otherwise provide as an autologous cell source are accompanied by detrimental abnormalities such as reduced self-renewal and differentiation potentials, thereby limiting their therapeutic efficacy.[40, 41] Furthermore, hMSC-mediated tissue regeneration would require exhaustive *in vitro* expansion to achieve sufficient numbers, and serially-expanded hMSCs demonstrate passage-associated abnormalities before reaching therapeutic mass.[42, 43] These passage-associated abnormalities illustrate a process where cells have an innate limit to their number of population doublings, known as the Hayflick limit (illustrated in Figure 2-3), before their physiological function begins to deteriorate. In 1961, Hayflick and Moorhead were the first publish this limitation in population growth due to aging characteristics at the cellular level utilizing 25 different cell lines from mice. From their work, they demonstrated that morphological changes occurred over many passages through the multi-month experiments including, but not limited to, cellular granularity, cell alignment, membrane contours, adherence, extra chromosome counts, susceptibility to infection and the rate of slowing growth[44]. Over the next many decades, this work set the tone that cells were not immortal and had some mechanism that tracked or injured cells from remaining in a healthy state. In fact, Hayflick himself concluded in 1984, well after the discovery of telomeres by Blackburn and Gall in 1978, that human (fetal) cells had a limit to the number of doublings they could undergo and when frozen the cells still knew

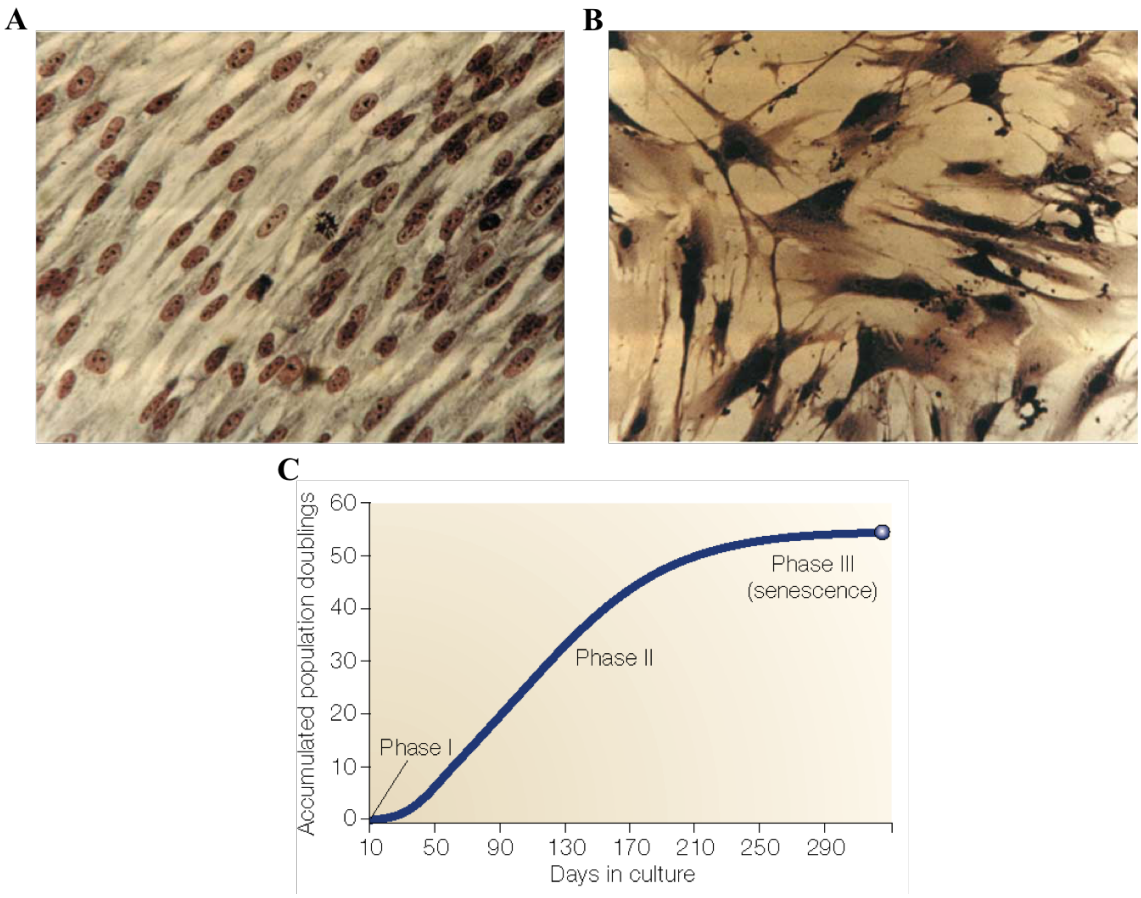

Figure 2-3 Hayflick Limit.

WI-38 human diploid lung fibroblasts at the 20th doubling (A) and the 50th doubling (B), illustrating the visual appearance of senescence in primary cells. The three phases describing the Hayflick limit are shown in (C). Adapted with permission from [45].

how many doublings that could perform before reaching the Haylfick limit.[46, 47] Hayflick likened it to a count-down clock or 'replicometer' where mechanisms in the nucleus were the site of enforcement.[48, 49]

According to Sames and Stolzing, aging is a culmination of multiple events that inhibit the ability of organisms to regenerate themselves after damaging insults.[50] At the cellular scale, senescence is the equivalent process where cell division is no longer possible after the increased level of injury to regenerative processes within the cell.[51] Senescence does not mean that cells are dead, but rather have an abnormal phenotype that is not representative of healthy cells and can exhibit a wide spectrum of functional outputs.[52] To articulate this point, accumulation of intracellular reactive oxygen species (**ROS**) that can damage lipids and proteins,[53] alterations in cell cycle regulation,[43] and susceptibility to carcinogenic agents[54] are all hallmarks of senescence as primary cells undergo excessive expansion *in vitro*.

As it pertains to hMSCs, 'aged' cells are larger, have greater surface area contact with their substrate, and have more articulated actin stress fibers.[55-57] Moreover, the ability to differentiate is altered. Younger cells are able to maintain multipotency (e.g. osteogenic, adipogenic, chondrogenic), but over multiple passages, older cells are only able to differentiate into osteogenic and adipogenic lineages, and eventually only osteogenic lineage.[58] However, there remains continued argument in the field if these *in vitro* findings are relevant to *in vivo* data demonstrating that transplanted MSCs were even less able to adopt the lineage of their host organ tissue environment.[59] Finally, donor variability of hMSCs has also caused differences in *in vitro* aging responses where

population doublings for some donors were higher than others as well as the spindle morphologies being maintained longer for some donors over others.[57, 60-66]

Since hundreds of millions of hMSCs are required to generate meaningful regeneration of bone in large animals, as an example,[67] the few hundred thousand hMSCs that can be isolated from the bone marrow of any typical donor would need to be expanded considerably and break the Hayflick limit in the process. This fact has been present in the literature[42, 43, 68] but often overlooked simply because it is inconvenient when proposing hMSCs for therapeutic applications. This has also happened in spite of what it is widely accepted in that 2D culture on TCPS is not an *in vivo* microenvironment equivalent. Even more, the advent of gerontology research having access to high-level sequencing tools may confound the prerequisite conditions for good hMSC donors before standards for donor quality and predictable response profiles can be articulated.[69] In order to expedite clinical translation, new strategies to maintain or reinstate hMSC fitness following expansion must be developed to counteract this inherent decline in cell health.[68]

2.1.3 Rise of Aggregate Cultures and Their Pitfalls to Meet Clinical Needs

In recent years, investigations of hMSCs cultured as aggregates ("spheroids" or "hanging drops") have revealed an increase in the expression of stemness and anti-inflammatory markers[70, 71] and presented a potential alternative method to producing highly potent stem cells for therapeutic uses, which have been exploited in the clinic in lieu of monolayer-expanded cells[68, 72]. For much of the history of biomedical research, two-dimensional cell culture was utilized due to its ease of use and uniformity, but with these advantages come the tradeoff with reduced likeness of a physical culture

environment reflective of the body (i.e.- lack of physiologically normal cell environment)[73]. Instead, three-dimensional culture is more reflective of normal cell environments as has been shown again and again over the past several decades, including the increased potential of stem cell and progenitor cell differentiation[74].

With respect of hMSCs, these aggregate three-dimensional cultures carry the property of prolonged replication lifespans, delayed senescence and increase gene expression of pluripotency genes like octomer-binding transcription factor 4 A (OCT4A), nanog homeobox (NANOG), and sex determining region Y-box 2 (SOX2)[75-77]. In most experimental setups, hMSCs are seeded into aggregates containing between 500 and 10,000 cells to generate their own *in vivo*-like microenvironments that promote the desired cell phenotype as mentioned above[78, 79]. Methods utilized to make these aggregates range from a variety of user-based precision-controlled techniques such as pro-aggregate hanging drop seeding, cell-repellant surface treatment of wells, and controlled aggregate assembly of cells in microfabricated culture dishes[79-82].

Granted these distinct advantages, aggregate culture of hMSCs does have significant drawbacks for translation, principally based on the technique incurring stresses on the cells that are not balanced or typically present. For example, size-dependent diffusion limits nutrient and waste processing, which can lead to necrotic cores of the aggregates if not carefully monitored[74, 83, 84]. This issue has been well documented in both hanging drop aggregates as well as surface treatments (poly(ethylene glycol)) and artificial membranes (chitosan) coated on well plates[75, 76, 85-87]. With altered viability, gene and protein expression within the hMSCs also becomes abnormal, especially if the

cells are then exposed to the *in vivo* environment and potential inflict harm on the recipient[88].

These studies suggest that a culture environment that provides significantly more cell-cell interactions compared to cell-matrix interactions more closely resembles the physiological compartment of hMSCs *in vivo* and can be exploited for therapeutic gain[89]. Such an approach would bypass the Hayflick limit and at the surface level appear to produce more potent hMSC populations using smaller cell masses compared to traditional *ex vivo* culture systems. However, these methods have relied upon forced aggregation or repellant surfaces to cluster the hMSCs and raises an important criticism: their use for *in vivo* implantation is severely limited since only cell density, culture time, and addition of biochemical factors can be varied. The costs to manage such a system would be prohibitive, and the spheroids couldn't be easily handled and would require massive cell numbers to reach therapeutic levels. Although a few studies have used encapsulation of hMSCs to harness their therapeutic potential while providing a means for handling, such as water-oil emulsions and micro-contact printed islands[90, 91], these studies lack critical investigation into how the technique could be expanded to large-scale efforts as a streamlined method of cell culture for hMSC-based therapies. Hence, if the aggregate method shortfalls are unable to be overcome, traditional *in vitro* expansion would leave the stem cell field with the original problems of cell senescence, decreased differentiation, and reduced paracrine signaling capability that could otherwise aid in healing of damaged tissues at the site of hMSC engraftment[92-97].

2.2 The Relationship Between hMSCs and Pericytes

2.2.1 Are hMSCs and Pericytes the Same Cell?

One of several remaining challenges in regenerative medicine is the ability to provide replacement tissues and organs with a robust vasculature system. The vasculature would be based on small arteriole and capillary networks that provide the means to transport nutrients to and waste from the bulk of the tissue it sustains. A microvascular network is a prerequisite to support metabolically demanding tissues that are normally developed and maintained *in vivo* and would have not been successfully developed *de novo* in tissue engineering laboratories. One critical cell type that holds together the microvasculature network is the pericyte, a cell type that is difficult to isolate but may have lineage relationship to hMSCs and provide a potential means for generating pericyte or pericyte-like cells without exhaustive isolation techniques.

Pericytes, also known as mural cells, are a supportive, mesenchymal cell type embedded within the vascular basement membrane of blood microvessels[98, 99]. Pericytes are known to make direct contacts with the endothelium ("peg-socket type") and participate in the development, stabilization, and maturation of vasculature through both physical interactions via mechanical contraction of adherent junctions to control vessel stabilization, and biochemical juxtacrine signaling to control vessel sprouting (Figure 2-4)[98, 100-102]. Pericytes can be identified by a panel of markers, such as positive expression for CD146, platelet-derived growth factor receptor beta (PDGFRβ), neuron-glial antigen 2 (NG2), platelet endothelial cell adhesion molecule 1 (PECAM), alpha-smooth muscle actin (αSMA), and negative expression of vascular endothelial cadherin (VE-cadherin) and Von Willebrand factor (vWF).

As pericytes and endothelial cells are localized closely, pericyte control of endothelial cell phenotype via chemically-mediated signaling cascades that include, but is not limited to, transforming growth factor beta and its receptor (TGF-β/TGFβR), platelet derived growth factor and its receptor (PDGF/PDGFR**)**, and Angiopoietin-1 (Ang1) / Angiopoietin-2 (**Ang2**) / tyrosine kinase with immunoglobulin-like and EGF-like domains 2 (Tie2) (Figure 2-5)[98, 101]. These signaling pathways are crucial for a variety of developmental and regenerative purposes in the body as was previously mentioned. Of the listed pathways, Tie2 becomes activated on endothelial cells upon binding with Ang1 and causes vessel growth and stabilization, and has been confirmed *in vivo* in an ischemia animal model[103, 104]. However, if Ang2 binds to Tie2, the beneficial effects seen in Ang1 are abrogated[98, 105]. Though, it should be mentioned that Ang2 is necessary at certain points in development in regulating postnatal angiogenesis and lymphangiogenesis[106]. Ang2 can be sourced from endothelial cells themselves and likely have autocrine effects in controlling vessel structure[107]. Taken all together, Ang1 serves as the main promoting ligand agent in cell-cell signaling for vessel growth and pericyte stability while Ang2 prevents Tie2 signaling, induces pericyte removal and collapse of vessel growth[98, 108].

In 2008, Crisan *et al.* raised a possibility that hMSCs and pericytes might actually be the same cell type (i.e. high stemness status with pro-angiogenic properties)[109]. Stemness refers to a cell's ability to retain self-renewal capacity and differentiation potential, and is controlled by transcription factors such as OCT4A, Nanog, and SOX2[110]. The isolated pericytes demonstrated multi-lineage differentiation capacity *in vitro* (adipogenic, chondrogenic, osteogenic, myogenic), and exhibited an expression profile of surface proteins similar to that of hMSCs both *in vitro* and *in vivo* (Figure 2-6).

Despite the original findings by Crisan *et al.*, other studies claimed to have identified markers that further delineated the pericyte phenotype from hMSCs, but the findings continue to raise questions of whether pericytes and hMSCs are more closely related than previously thought. For example, CD146 is a marker of both hMSCs and pericytes. However, $CD146^+$ fraction of perivascular cells, but not unfractionated MSCs or $CD146^-$ cells, maintain the undifferentiated state of human hematopoietic stem cells, suggesting a critical role for pericytes in the bone marrow niche[111]. A subpopulation of perivascular cells in the bone marrow corroborated the previous findings having identified the subpopulation of perivascular cells as promoting angiogenesis[112]. Additionally, perivascular cells isolated from multiple human organs exhibited characteristics distinctly similar to those of hMSCs including multi-lineage differentiation capacity *in vitro* and presentation of surface proteins identical to that of hMSCs both when serially-expanded *in vitro*, as well as in the native perivascular niche *in vivo*.[113] Pericytes are also positive for STRO-1[111], which further suggests an *in vivo* relationship between the two cell types that might be lost in culture.

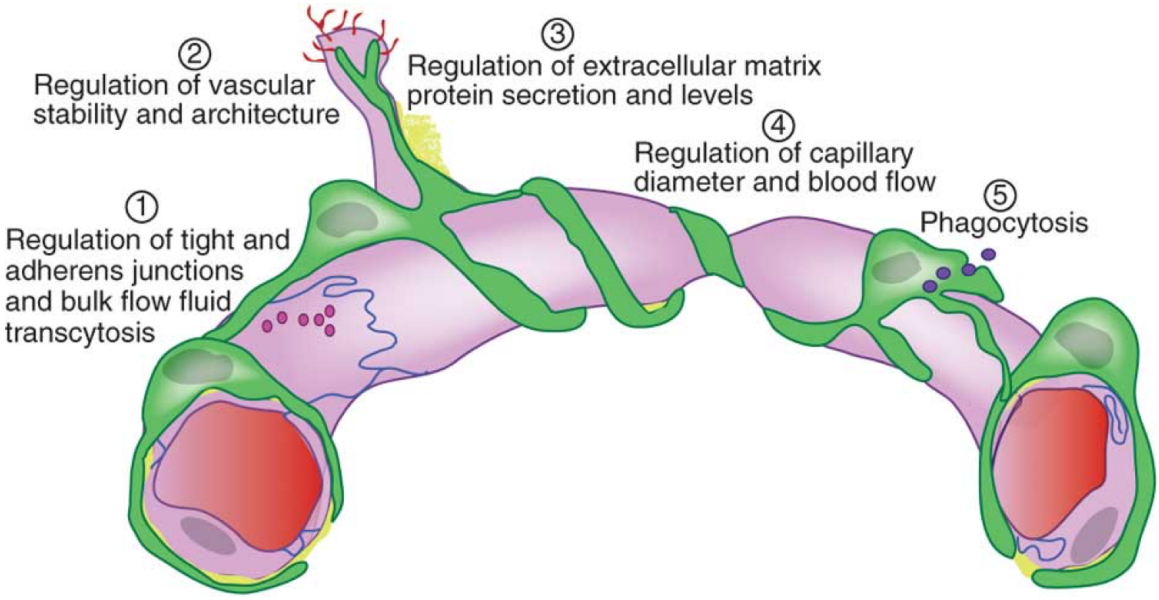

Figure 2-4 Pericyte Localization and Function.
Pericytes localize around endothelial cells that make up capillary networks, and in some cases larger arterioles and venules. They have a variety of functions including: (1) influencing endothelial tight and adherens junction proteins; (2) regulating the stability and architecture of newly formed microvessels; (3) secreting extracellular matrix proteins comprising the basement membrane; (4) regulating capillary diameter and blood flow; and (5) provide clearance and phagocytotic functions depending on surrounding tissue type. Adapted with permission from [114].

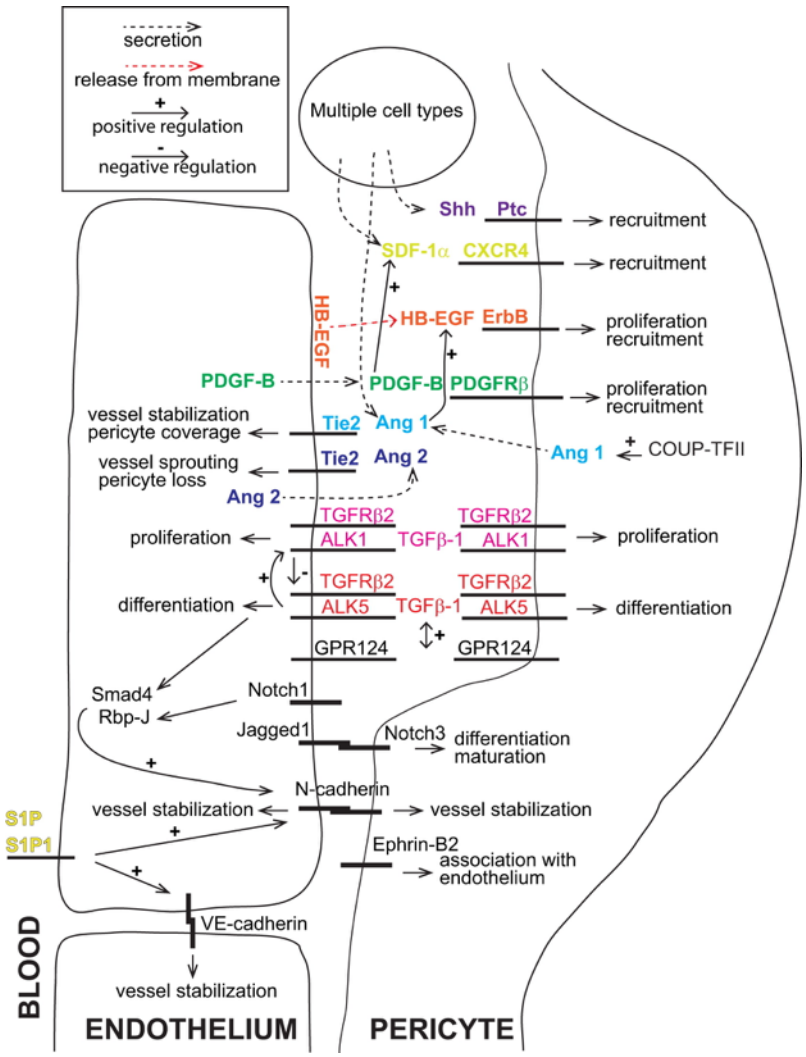

Figure 2-5 Signaling Pathways Mediating Mural Cell Recruitment, Differentiation, and Vascular Stabilization.

Pericyte recruitment to the endothelium is mediated by multiple ligand-receptor complexes. A ligand-receptor pair is indicated by the same color. Adapted with permission from [115].

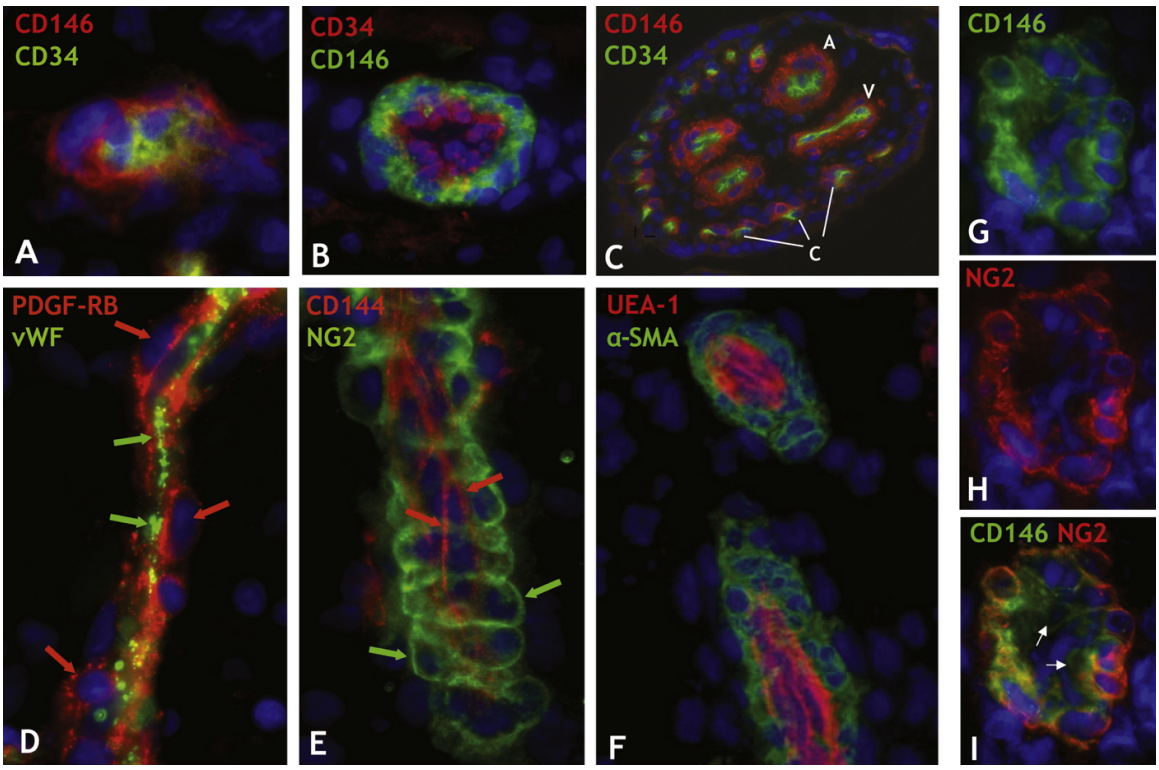

Figure 2-6 Immunodetection of Perivascular Cells in Human Organs.
Sections were indirectly immunostained with antibodies to mural and endothelial cell markers. (A) Myocardium: a capillary endothelial cell in transverse section marked by CD34 expression (green) is closely surrounded by a CD146+ pericyte (red) (×900). (B) Skeletal muscle: small vessel transverse section; CD146+ perivascular cells (green) surround CD34+ endothelial cells (red) (×400). (C) Placental villus: arterioles (A), venules (V), and capillaries (C) are all lined with CD34+ endothelial cells (green) surrounded by CD146+ perivascular cells (×100). (D) Skeletal muscle: small vessel longitudinal section; PDGF-Rβ-positive perivascular cells (red; red arrows) surround vWF+ endothelial cells (green; green arrows) (×400). (E) Fetal pancreas: small vessel longitudinal section; NG2-positive perivascular cells (green; green arrows) surround CD144+ endothelial cells (red; red arrows) (×400). (F) Transverse and longitudinal sections of placental small blood vessels. Endothelial cells marked by the *Ulex europaeus*lectin (red) are surrounded by perivascular cells expressing α-SMA (green) (×400). (G–I) Transverse section of a skeletal muscle blood vessel double stained with antibodies to CD146 (G) and NG2 (H). (G) and (H) have been merged to create (I). Perivascular cells marked by CD146 expression also express NG2. Cells in a more central location express exclusively CD146 (arrows) and likely represent endothelial cells (×300). (A) Fetal myocardium; (B, D, G–I) skeletal muscle; (E) fetal pancreas; (C and F) placenta. Nuclei have been labeled blue with DAPI. Reprinted with permission from [113].

2.2.2 hMSCs and Pericyte Utilization in Tissue Engineering

In light of these multiple findings, some tissue engineers have begun trying to use pericytes in tissue engineering settings as a comparison against hMSCs that have already, and continue to be, exhaustively utilized for vascularization of potential tissue constructs. Many research groups have used hMSCs as a pro-angiogenic supporting cell type for vascular applications[116-121], exploiting their inherent pro-angiogenic properties provided the correct contextual cell culture environment. One group implanted hMSCs with endothelial cells housed within a collagen/fibronectin gel into immunodeficient mice that resulted in stable vasculature formation within the construct for more than 130 days[122]. hMSCs alone could not sustain vasculature *in vivo*, indicating a limitation in their use. To address this shortfall, two papers characterized functional differences between hMSCs and pericytes. The first group developed a micro-patterned system *in vitro* to study the ability of pericytes to stabilize EC tubes without collapsing[123]. The authors showed that pericytes, but not hMSCs, were able to migrate through a mock basement membrane to maintain the integrity of EC tubes, whereas the MSC-supported tubes were collapsed at 16 hours post-incubation. Complimentary to these results, a second research group performed three different co-culture models with human endothelial cells and demonstrated that human placenta-derived pericytes, but not hMSCs or fibroblasts, were able to stabilize EC tubes in 2D Matrigel culture, promote angiogenic sprouts in 3D co-culture, and form interconnected endothelial cell cords[124].

With respect to pericyte-only tissue engineering, one early study utilized human pericytes to pre-seed vascular grafts based from poly(ester-urethane)urea scaffolds in order to repair damaged aortas in rats[125]. 8 weeks after implantation, the pericyte-seeded scaffolds were found to be 100% patent compared to 38% of the scaffold-only controls,

and demonstrated remodeling with ECM deposition, invagination of $aSMA^+$, $calponin^+$ cell layers, and a vWF^+ lumen. However, no hMSC controls were utilized to compare with the existing literature. In a separate study, three-dimensional polyethylene glycol (PEG) hydrogels were formed with muscle tissue pericytes to aid in muscle regeneration[126]. Pericytes obtained from adult boars showed remarkable increase in regeneration capacity in the hydrogel environment to make new muscle tissue reminiscent of young, healthy tissue. In fact, the degree of both vasculogenesis and myogenesis were so improved that no further modification to the PEG hydrogel was needed other than fibrinogen coupling. Finally, with a similar aim in mind, Saik and colleagues created polyethylene glycol gels with immobilized PDGF-BB to stimulate encapsulated pericytes to synthesize native ECM proteins fibronectin, collagen and proteoglycans[127]. The basement membrane formed by the pericytes in this construct for endothelial cells to engraft and undergo angiogenesis in parallel with normal pericyte-endothelial cell chemical signaling exchange.

In conclusion, the pro-angiogenic and anti-inflammatory expression coupled with pronounced stemness factor expression suggests that an hMSC phenotype with high stemness also regulates vascular formation and inflammation, two functions that are incumbent for pericytes[98, 128]. However, no study has successfully identified any marker that uniformly links hMSCs as pericytes, meaning definitive evidence for the theory of pericytes and hMSCs being the same cell type does not exist.

2.3 Biomaterials and Their Use in Modulating Stem Cell Behavior

hMSC behavior can be manipulated by changing the parameters of the extracellular environment to which they are exposed. hMSCs have been shown to

respond to changes in the physicochemical properties of the extracellular matrix (ECM) that result in global alterations to cell phenotype. Indeed, there is a supporting body of literature that explores the competitive influences of substrate properties and how such properties regulate hMSC fate and function[8], but some pieces of the puzzle that explain how hMSCs respond to materials are still missing. These inherent properties in natural ECM are also the same properties that synthetic materials try to recapitulate. However, due to the continued discoveries of how material properties alter specific feedback loops, it makes designing successful materials, natural or synthetic, more difficult. In general, many investigated properties that researchers are transfixed on include, stiffness, nanotopography, cell adhesiveness, molecular flexibility, chemical funcitonality, binding affinity, degradability and degradation products (Figure 2-7)[129]. Three will be discussed due to relevance to this thesis work.

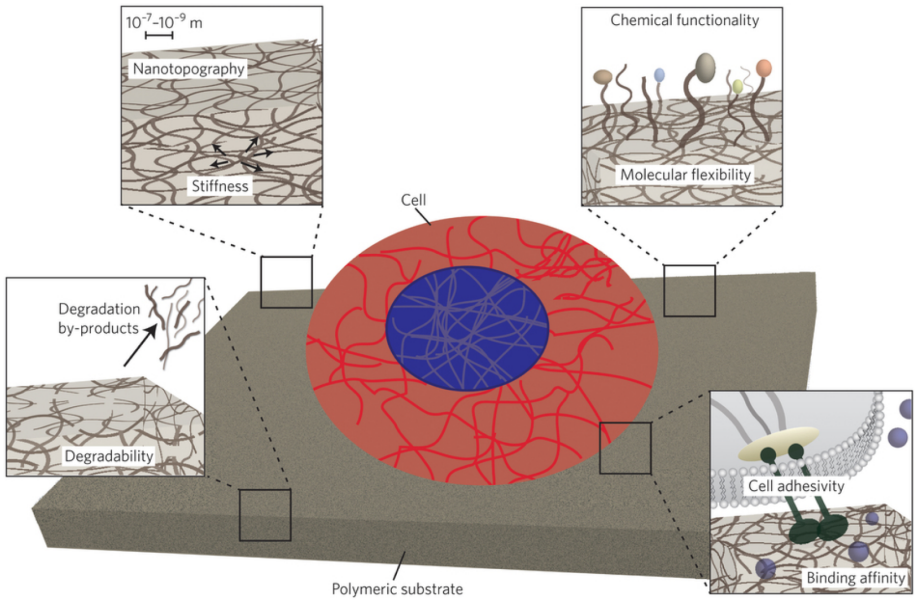

Figure 2-7 Inherent Material Properties.
Stem cell fate decisions can be affected by properties inherent to materials near the cell/material interface, such as nanotopography, stiffness, chemical functionality, molecular flexibility, the adhesivity of cells to the material, its binding affinity for soluble factors, its cell-mediated degradability and its degradation by-products. Reprinted with permission from [129].

2.3.1 Stiffness

Whether using natural or synthetic materials, hydrogels (water-swelling polymer networks of protein or synthetic material) allow for very controlled crosslinking that modulates the gel stiffness. In early investigations of hydrogel stiffness, poly(acrylamide) was the first material of choice given the ease of fabrication and dynamic range of stiffness that could be programmed into the hydrogel[130]. With further chemical modification, natural ECM proteins like collagen I or well-defined peptide sequences could be tethered to the gel to provide binding sits for cells. Shortly after development of the poly(acrylamide) system, more hydrogel platforms came into prominent use like hyaluronic acid and alginate gels, both of which have the same dynamic stiffness range as

poly(acrylamide)[131, 132]. However, no hydrogel system has become more ubiquitous than the poly(ethylene glycol) (PEG) hydrogel system because it can easily be formed for three-dimensional cell culture.

One of the first watershed studies exploring matrix influence on hMSCs discovered that matrix elasticity could govern cell fate[133]. When hMSCs were cultured on matrices that had moduli reflective of a given tissue type, the hMSCs were induced to differentiate into cells that are best suited to the matrix environment (e.g. soft matrix for neuronal tissue promoted neurogenesis and stiff matrix for bone promoted osteogenesis) (Figure 2-8). Recently, there was debate as to whether protein-tethering variation based on substrate pore density was the primary agent responsible for perceived matrix stiffness cues[134], but a 2014 article in Nature Materials[135] rebutted such claims. An *in vivo* study in 2010 had taken mouse muscle stem cells and determined if stem cell self-renewal was also affected by substrate elasticity. Only when the muscle stem cells were cultured on muscle-like substrates (~12 kPa) did the stem cell generate a self-renewing cycle that also generated a fraction of cells that differentiated into fully functional muscles cells and eventually small tissues[136].

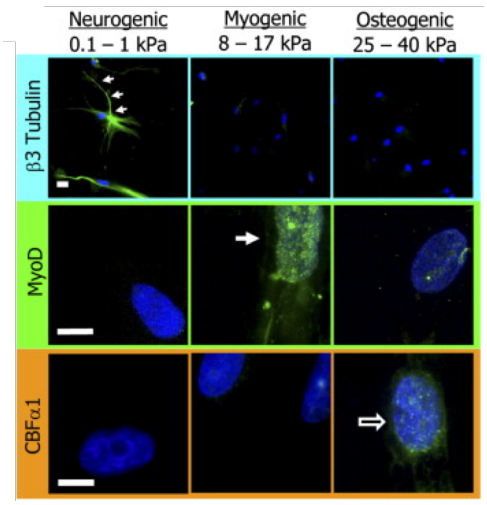

Figure 2-8 Matrix Stiffness Regulates hMSC Differentiation.
hMSCs cultured on polyacrylamide gels of specified elastic moduli induced differentiation into set lineages. Linage evaluation was based on inmmunofluorescent imaging of lineage-associated protein markers. Adapted with permission from [133].

Curiously, some groups have recently demonstrated that downstream regulators of stem cell responses are highly dependent on substrate stiffness. Localization of the yes-associated protein (YAP) and PDZ-binding motif (TAZ) are polarized with respect to compartmentalization (Figure 2-9), as these transcription factors gets shuttled to and from the nucleus with subsequent influence on Rho GTPase activity[137, 138]. Without these factors, differentiation of hMSCs were highly altered or impaired, yielding the conclusion that matrix elasticity remains a central pillar in the stem cell phenotype decision tree. Even more interesting, when hMSCs were cultured on substrates that had tunable stiffness that oscillated between soft and stiff, the cells had an imparted 'memory' of the prior stiffness via these transcription factors and differentiated based on the memory stiffness if induced before the cell had time to recognized the new stiffness of the gel[139].

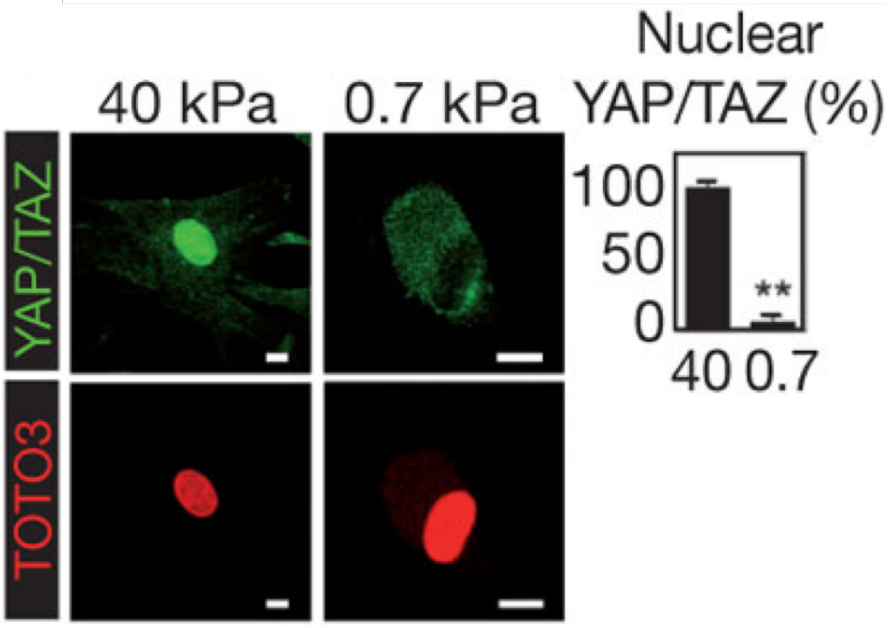

Figure 2-9 YAP/TAZ are Regulated by ECM Stiffness.
Confocal immunofluorescence images of YAP/TAZ and nuclei (TOTO3) in human mesenchymal stem cells (MSC) plated on hydrogels. Scale bars, 15 μm. Graphs indicate the percentage of cells with nuclear YAP/TAZ. (n = 3). Adapted with permission from [138].

2.3.2 Nanotopography

As these discoveries regarding substrate stiffness were being probed, other groups were concurrently exploring the influence of nanotopology and how shaped surfaces could intentionally push cells to adhere in patterns. Nanotopography of substrate surfaces could confine cell interactions with materials or provide prominent z-axis features that recapitulated matrix morphologies found in tissues. Many methods have been developed to alter nanotopography. Nanolithography can alter surfaces to control cell shape, cell size and tissue patterning via generation of pits[5, 140], pillars[141] and channels[142]. Reviewed by DH Kim *et al*, nanolithography methods alter the spatial presentation of adherent areas on a substrate provides the cell with a set of instructions of how to morphologically respond to its environment (Figure 2-10)[143]. For instance, NIH 3T3 cells adopt different

aligned and spread morphologies depending on how the adhesive surface is designed, a response that is readily applicable to hMSCs. In fact, similar patterning can control hMSC orientation under dynamic culture conditions[144]. Depending on the interval distances between adhesive and repellant zones, along with total surface area and curvature of the surfaces, cells will adopt a variety of spread and spindle morphologies that can be used to influence not only stem cell differentiation but also tissue formation similar to native tissue organization observed in histological sections.

Similarly, channels and pillars in varied spatial layouts via nanolithography can promote stem cell renewal or differentiation. It has been demonstrated the human embryonic stem cells maintained a self-renewing population within 30 nm diameter pillars in honeycomb patterning[141] while 120 nm diameter nanopits with 300 nm center-to-center spacing allowed hMSCs to self-renew and asymmetric pit spacing promotes differentiation[5]. Moreover, microgroves of adhesive substrate platforms have influenced epigenetic signaling in induced pluripotent stem cells to maintain their self-renewing population and resist spontaneous differentiation without the need of small-molecule supplements[145].

Nanotopological substrate features can also be generated by electrospinning of natural and synthetic polymers[146]. By adjusting electrospinning variables such as voltage, collection speed, and syringe nozzle, fiber sheets can comprise of homogenous or heterogeneous fiber and pore sizes[147]. Fiber ranges have been tuned as low as tens of nanometers working up to many microns[148].

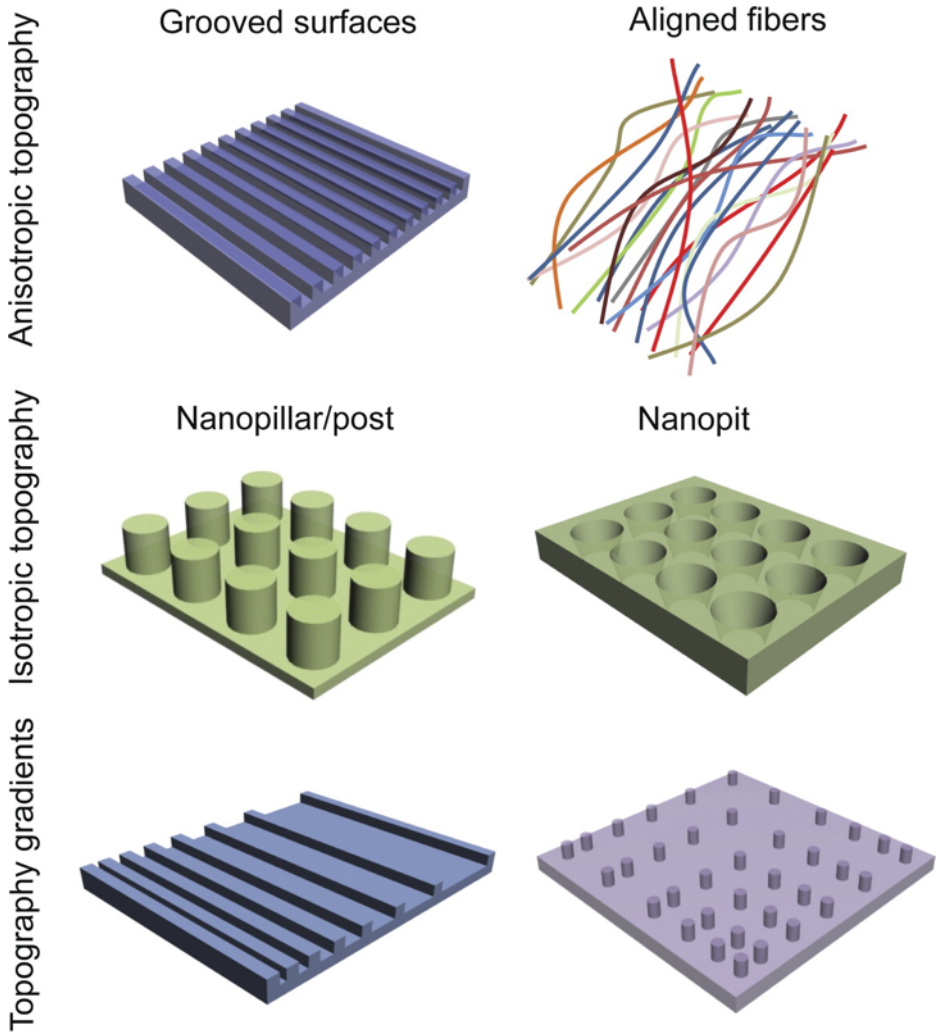

Figure 2-10 *In Vitro* Culture Platforms that Alter Nanotopography.
Schematics of three representative nanotopography geometries commonly used as cell culture substrates, including nanogroove/ridge arrays, nanopost arrays, and nanopit arrays. Anisotropic topographies are directionally dependent, in this case, providing cues along a single axis. Isotropic topographies are uniform in all directions, providing cues along multiple axes. Topography gradients provide cues through gradual changes in physical features (e.g., groove spacing) along a particular direction. Schematics are not drawn to scale. The ranges of relevant feature sizes could vary between 100 nm and 1 μm, depending on the design dimensions of the substrates' nanofeatures. Adapted with permission from [143].

2.3.3 Chemistry

Finally, surface chemistry has also served as a dominant theme in biomaterials design in controlling hMSC phenotype. An early example of this involved functionalizing

glass with different functional end groups (e.g, -CH_3, -NH_2, -SH, -OH, and –COOH) that would alter binding capacity and adsorption properties of serum protein and cells[149]. Cell morphologies were drastically altered when cultured on the different surfaces (Figure 2-11A) and the resulting phenotype commitment of the hMSCs could be seen at the transcriptional level as specific combinations of ECM-related molecules and sensing proteins were more significantly expressed on particular functionalized glass substrates (Figure 2-11B). These results altered the landscape of synthetic materials as culture substrates such that functionalized moieties could recapitulate previous findings for hMSC differentiation into desired tissue types but in larger anatomical dimensions[3]. More specifically, it was the degree of functional moiety incorporation that enhanced the degree of hMSC differentiation, as evaluated by immunofluorescent staining.

ECM-related molecules are not the only substances that can be built into the substrates. Photopolymerization has enabled different synthetic polymer components to be attached to natural and synthetic polymer backbones, and control of this process further allows the user to define where these polymer components are located within or on the substrate (Figure 2-12)[3, 150]. Depending on the chemistry of the added group, different signaling molecules and growth factors are selectively sequestered and provide an additional chemical instruction beyond material cues[151]. Further development of this technology towards high-throughput screening are also being explored as libraries of organic and inorganic materials can aid in decoupling how altered chemistry, topology and stiffness (among other previously listed material characteristics in Section 2.3.1) influence stem cell behavior[152-155].

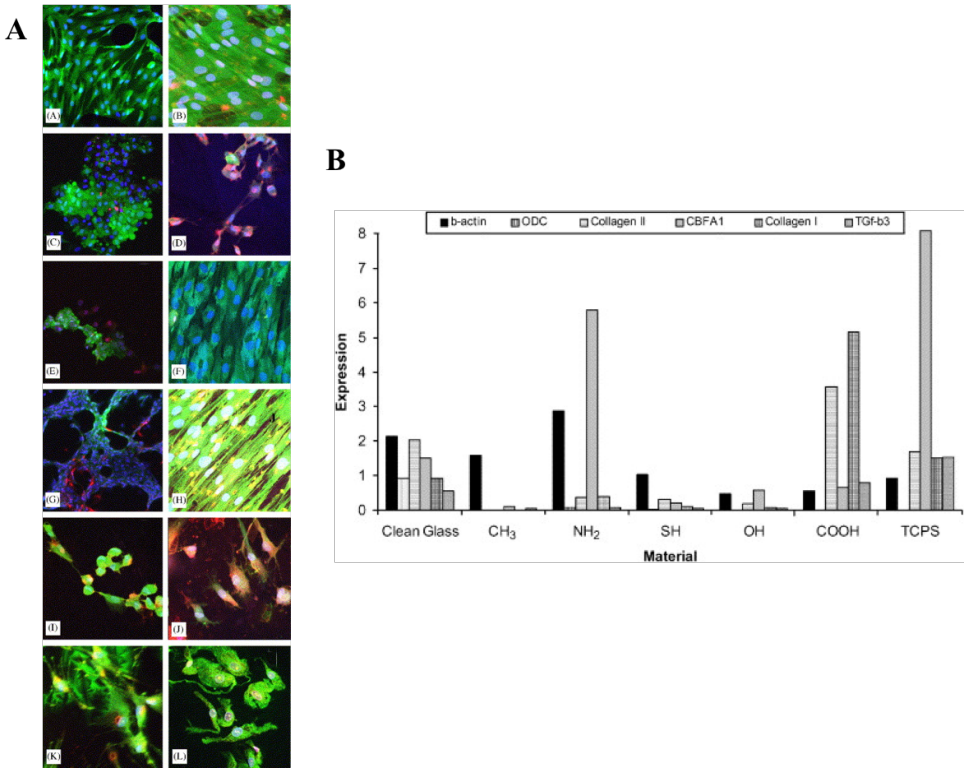

Figure 2-11 Surface Functionalization Alters hMSC Morphology.
(A) Cell viability with Calcein AM (green) and ethidium homodimer (red) was ascertained through immunofluorescent imaging with visible alterations in hMSC morphology depending on surface treatment. (B) qRT-PCR of ECM-related molecules and sensing proteins for each functional group. Adapted with permission from [149].

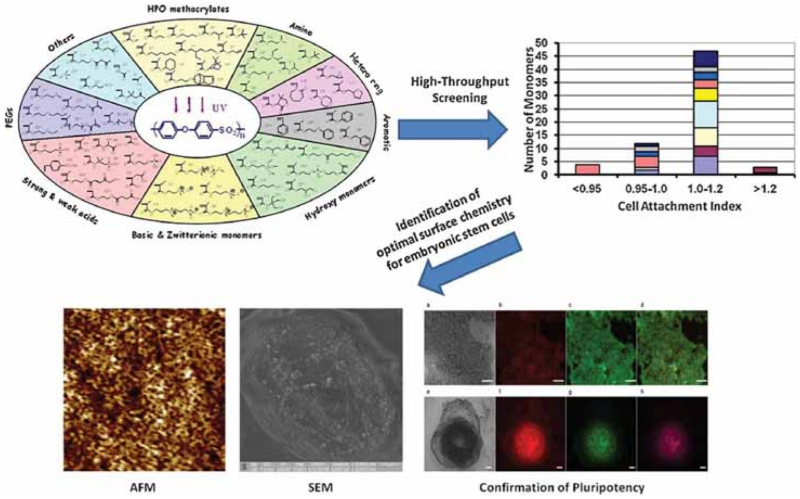

Figure 2-12 High-Throughput Screening of Materials for Stem Cell Culture.
Methodology for high-throughput screening for (embryonic) stem cell culture substrates[150]. Reprinted with permission.

2.3.4 Issues of Material Tunability and Need for More Pro-Stemness Materials

Matrix stiffness, surface chemistry and topology continue to remain as the dominant ECM variables being probed. Yet, there remain issues of platform tunability in order to vary more than one material parameter in a precisely controlled manner. For example, polyacrylamide and poly(dimethyl siloxane) gels have been the tools of choice when studying hMSC responses to the extracellular environment as these mediums allow for tight control over certain material properties[133-135]; however, these platforms offer greater control over stiffness and protein density/crosslinking tunability, leaving properties such as roughness, adhesiveness, and hydrophilicity less easily manipulated when they could, in fact, influence hMSC phenotype. Furthermore, these materials are unable to be fabricated as three-dimensional scaffolds, thereby limiting the implications and scalability of findings.

Because of these substrate limitations, the discourse in the literature over the last 10 years has primarily promoted hMSC mechanosensitivity as a fundamental regulator of lineage specification and has ignored the other end of the spectrum: namely, the material properties that assist hMSCs in resisting differentiation. To date, nearly all studies regarding hMSC interactions with biomaterials have focused upon directed differentiation to specific lineages, aiming to improve their potential for tissue engineering applications[3, 5]. The simplified systems employed in the aforementioned studies have yielded paradigm-shifting insights for outside-in signaling from the microenvironment, but the number of remaining experiments that can yield meaningful results with these systems may be limited. Consensus opinion by leading experts in the field has articulated the need for developing more highly integrated, complex material systems to continue the progression of the field[129].

Biomaterials investigators more recently considered making substrates for long-term maintenance of hMSC stemness. For tissue regeneration in a clinical setting, autologous or allogenic hMSCs would be expanded *ex vivo* to achieve relevant numbers, and then differentiation would be induced over several weeks. Despite the documented loss of stem cell phenotype and potency during this type of long-term culture[43], the underlying requirement for expanding healthy, undifferentiated hMSCs prior to differentiation, or for reinstating the reduced capacity of aging cells, has been significantly overlooked in the literature. To address the unmet need, studies oriented at maintaining expression of hMSC stemness genes in response to changing material and biochemical cues has yielded very few substrates that can maintain an undifferentiated state of hMSCs with high stemness[24, 156-158]. In a seminal paper that evaluated the effects of nanotopography on intracellular function, McMurray *et al* demonstrated that regularly-spaced nanopits in a thin polymer substrate improved the expression of *ALCAM* and *CD63* (markers of undifferentiated hMSCs) while supporting long-term culture of hMSCs and sustaining differentiation capacity[140]. However, the roles of cell-cell/cell-material interactions and coupled material properties that undoubtedly played a role in driving cell behavior were disregarded. Furthermore, only a limited selection of markers was used to classify hMSCs as undifferentiated, and the resulting phenotype of the cells was not explored. Nonetheless, this work represents an important step in the interface of hMSC and biomaterials as it links high-level stem cell biology to controlled alterations at the substrate surface to maintain an undifferentiated status of hMSCs.

Chapter 3: Aim 1- Expanding the Copolymer Library

3.1 Introduction

Two decades of research have demonstrated that cell fate and function can be regulated by the physicochemical properties of biomaterial culture substrates[159]. hMSCs respond to changes in the physicochemical properties of the extracellular matrix (ECM) such as stiffness and nanotopography, revealing an intrinsic sensitivity of cells – particularly hMSCs – to changing material properties[5, 133, 160]. This outside-in signaling has become a dominant theme in the biomaterials community with several groups attempting to elucidate how hMSCs sense their environment and identify how the signal is transduced to elicit functional change in the cell[5, 133-135].

Most studies to-date have focused on material-mediated differentiation of hMSCs toward specific lineages, but one landmark paper demonstrated that topographical cues can modulate hMSC stemness and metabolism[140]. Indeed, development of culture substrates that maintain stemness (that is, the ability of a stem cell to both self-renew and differentiate) is critical for the success of hMSC-based therapies for two reasons. First, exhaustive *ex vivo* expansion of hMSCs is required to generate clinically-relevant cell numbers, but this yields functional abnormalities such as reduced stemness and accumulation of reactive oxygen species (ROS)[43]. Intracellular ROS and the associated redox mechanisms are tightly-controlled in healthy tissues; however, aberrant regulation results in increased ROS levels that oxidize DNA and proteins[161], leading to stem cell aging and quiescence[162]. Second, aging patients (e.g. 65+ years old) who stand to benefit the most from autologous, hMSC-based therapies donate cells that already exhibit reduced stemness and increased ROS, and additional expansion renders their cells therapeutically-limited.[42] Identification of physicochemical material properties that

regulate hMSC health without the need for exogenous biomolecules would overcome these translational barriers. Despite this fact, material systems that simultaneously regulate hMSC stemness and redox capacity remain undeveloped, and systematic evaluations of the physicochemical parameters that affect these pathways have rarely been explored. Therefore, in order to expedite clinical translation, strategies to maintain or reinstate hMSC stemness are needed to address these issues[68].

Cell-matrix and cell-cell interactions instruct stem cell behavior. Within their *in vivo* niche, stem cells are anchored to the extracellular matrix and neighbouring cells, and the competition between these interactions is instrumental for maintaining stemness or inducing differentiation. Most biomaterial systems encourage cell-matrix adhesion, yet biasing the cells in the opposite direction (i.e. toward cell-cell interactions) can be equally beneficial. For example, hMSCs cultured as substrate-free aggregates, or "hanging drops" (HDs), are initially comprised of only cell-cell contacts and have garnered attention due to their anti-inflammatory capabilities[70]. However, HDs pose technical problems for clinical translation, including scalability, handling, and implantation. Material systems such as patterned surfaces[163], pre-fabricated microwells[164], or chitosan-based substrates[75, 165] can be leveraged to promote cell aggregation, but in-depth analysis of the structure-function relationship between the material composition/properties and subsequent cellular response remains undeveloped. To address this issue, synthetic copolymer culture substrates can simultaneously provide physicochemical cues that encourage HD-like cell behaviors, while tuning the material composition/properties for in-depth analysis of material-mediated regulation of the cellular response.

In this aim, we designed copolymers of varying surface repellency that effectively modulate both stemness and redox regulation in hMSCs, and demonstrate that these effects can be finely tuned by altering the polymer composition.

3.2 Methods

3.2.1 Polymer Substrate Preparation

All polymers were synthesized as previously described [166]. Unless otherwise noted, all *in vitro* experiments were performed on spin-coated polymer films that were prepared with a commercial spin-coater (Laurell Technologies, North Wales, PA, USA). 15 mm circular glass cover slips (Fisher Scientific, Waltham, MA, USA) or 10 cm Pyrex Petri dishes (Corning Inc., Corning, NY, USA) were first cleaned with 100% ethanol (Sigma Aldrich, St. Louis, MO, USA), rinsed with dH_2O, and heated to 80°C for ~20 min to dry. A 1% weight/volume (w/v) solution of the specified polymer in tetrahydrofuran (THF, Sigma Aldrich) was spun for either 30 seconds at 3,000 RPM on glass cover slips (50 µl solution/sample) or 2 min at 1,500 RPM on Petri dishes (1 ml solution/sample). All samples were then exposed to constant cold-trap vacuum for ≥ 30 min to remove excess solvent and kept in a desiccator until use. For cell experiments, substrates were UV sterilized for 30-60 min on each side before use; for 15 mm cover glass, samples were placed in a 24-well plate, and secured with an autoclaved silicon O-ring (McMaster Carr, Atlanta, GA, USA).

For protein pre-coating experiments, the desired amount of human fibronectin (Fisher Scientific) was diluted in serum-free αMEM and allowed to adsorb to the material surface for ≥ 30 minutes at 37 ºC. Samples were then rinsed twice with PBS and used for culture experiments.

3.2.2 Physicochemical Characterization of Polymer Library and Surfaces

Surface roughness was measured on dry, spin-coated samples by profilometry (Dektak 150 Surface Profiler, Veeco, Plainview, NY, USA) using a 2 mg force, a 1000 μm scan length over 10 seconds, and a 65.6 μm z-axis scan range. N=10 measurements were made on each of n=3 independent samples and the average deviation from the arithmetic mean (Ra) is reported. Protein adsorption was measured by quartz crystal microbalance with dissipation (QCM-D). Polymer was spin coated onto gold-coated quartz crystal (5 MHz, QSX 301; Q-Sense AB, Goetenberg, Sweden) using a ~50 ml of 10 mg/ml solution at 3,000 RPM for 30 seconds using a spin coater (Headway Research Inc., TX). QCM-D measurements were carried out using a Q-Sense E4 instrument (Q-Sense AB, Goetenberg, Sweden) at 37.5 °C with 10% FBS, according to standard protocols.[167] The data were analyzed using the Voigt model in the Q Tools software supplied by Q-Sense, Inc. Contact angle was performed with a goniometer (Ramé-Hart, Succassunna, NJ, USA) using 10 μl droplets of deionized water. Three measurements were taken on each of three independent samples, and the average advancing contact angle was reported (n = 9).

Surface modulus was measured using a Veeco NanoScope V (Bruker Corporation, Billerica, MA, USA) using a cantilever with a rectangular cross-section (MLCT tip B; Bruker AFM Probes). A glass coverslip was used as a control sample while all spin-coated coverslips were tested using an identical protocol. Samples were first incubated in PBS overnight before testing in air at 37 °C. A topographical scan of a 5 μm x 5 μm area was made in contact mode sampling 512 samples/line for 512 lines with a scanning rate of 30 μm/s. A z-limit of 5 μm was used to prevent tip failure. A force volume scan was then performed to allow for an estimation of the sample's area-averaged

elastic modulus. A 16 x 16 grid spanning the same area as the topographical scan was indented at 1.54 μm/s to a maximum motor movement of 750 nm. Calibration of the deflection-voltage curve *d(V)* of the cantilever beam was estimated using a series of indentations into a glass coverslip by assuming rigidity of the coverslip. This calibration had the form of:

Equation 3-1:

$$d[\text{nm}] = 0.0000113V^2 + 0.00836V - 12.3$$

where *V* has units of volts (n=3; R^2=0.997). The Sader method[168] was used to estimate the cantilever stiffness *k* (approximately 0.02 N/m) such that the force could be estimated as $F = kd$. The indentation depth *u* was computed as:

Equation 3-2:

$$u = (P - P_c) - (d - d_c)$$

where *P* is the absolute position of the stage, P_C is the absolute position at the point of contact between the tip and the sample, and d_C is the deflection of the cantilever at the point of contact. This allowed the generation of a force-displacement *F(u)* diagram for each sample point in the force-volume image. These data were then analyzed using conical indenter theory corrected for the true probe geometry.[169] These results were then used to estimate the elastic modulus *E* in a least-squares sense by treating it as a parameter in a Levenberg-Marquadt fitting algorithm. The expected form of the *F(u)* data was given by:

Equation 3-3:

$$F(u) = \frac{2\beta \tan\alpha}{\pi} \frac{E}{1 - \upsilon^2} u^2$$

where α is the half-angle of the indentation probe (nominal average 71.25°), β=1.023 is the asymmetric correction factor for a probe with square base[169], and assuming incompressibility (i.e. Poisson ratio ν=0.5) and rigidity of the indentation probe. The area-averaged elastic modulus was then found by averaging the modulus determined for each of equally-spaced 256 locations within the 5 μm x 5 μm area characterized during the topographical scan. Analysis was performed using NanoScope Analysis v1.50 (Bruker). Ten randomly-selected locations were analyzed using the indentation analysis tools in this software package. Data from 10-70% of the full force scale were included in the analysis.

^{1}H NMR was conducted on a 400 MHz AV-400 console (Bruker Instruments, Inc) using 1% w/v solutions in $CDCl_3$. Mole percent composition for each copolymer was determined by comparing the integration of CH_2–CH_2 protons of PEG (δ = 3.65 ppm) to that of O–CH_2 protons representing the ε-carbon of the PCL peak at (δ = 4.05 ppm)[170].

Molecular weight was measured by gel permeation chromatography. After dissolving copolymers in THF at 10% w/v, the polymer solutions were injected at 1 mL/min through a Waters chromatography system equipped with a binary HPLC pump, refractive index detector, dual λ absorbance detector, and four 5 mm Waters columns (300 mm x 7.7 mm) connected in series (Waters Corporation, Milford, MA)[171].

3.2.3 Cell Culture

hMSCs were either purchased from Lonza (Walkersville, MD, USA). hMSCs were maintained in complete media (CM) composed of alpha-minimum essential media with nucleosides (αMEM, Life Technologies, Carlsbad, CA, USA) with 16.7% fetal bovine serum (Life Technologies), 1% penicillin/streptomycin (Life Technologies), and 4

μg/ml plasmocin (InvivoGen, San Diego, CA, USA). Cells were kept in a humidified incubator at 37°C and 5% CO_2, and media was replaced twice each week. When ~80% confluent, hMSCs were detached with 0.05% trypsin-EDTA, re-seeded at a density of 100 - 500 cell/cm^2, and cultured for 7-14 days before reaching confluence. For all experiments, hMSCs (page < 6) were seeded at a density of 10,000 viable cells/cm^2, as determined by exclusion of Trypan blue, and cultured for three to four days.

3.2.4 Measuring Levels of Intracellular Reactive Oxygen Species (ROS)

hMSCs were incubated with 10 μM 5-(and-6)-chloromethyl-2',7'-dichlorodihydrofluorescein diacetate acetyl ester (DCFDA) (Life Technologies) in serum-free DMEM for 30 minutes following the manufacturer's instructions. Cells were trypsinized and run on a FACS Calibur flow cytometer (BD Biosciences, Franklin Lakes, NJ, USA) with the appropriate unstained control. N=3 biological replicates were conducted per substrate condition. Data were analyzed by FlowJo software (Tree Star Inc., Ashland, OR).

3.2.5 Measuring Cell Proliferation

hMSCs were incubated with 10 μM 5-ethynyl-2'-deoxyuridine (EDU) (Life Technologies, Carlsbad, CA, USA) in serum-free media for 12 hours before the completion of the 96-hour culture period. Cells were fixed in 4% paraformaldehyde (PFA, Sigma Aldrich, St. Louis, MO) and processed per the manufacturer's instructions. Images were taken with a Zeiss LSM 710 microscope (Carl Zeiss, Oberkochen, Germany), and the images were processed with Zeiss Zen software and ImageJ (National Institutes of Health, Bethesda, MD). N=6 biological replicates were used per substrate condition.

3.2.6 Immunocytochemistry and Immunophenotyping by Flow Cytometry

hMSCs were fixed with 4% paraformaldehyde (PFA, Sigma Aldrich) for 15 min, permeabilized with 0.3% Triton-X (Sigma Aldrich) for 15 min when probing intracellular targets, and blocked with 10% goat serum (Sigma Aldrich) for >2 hours, all at room temperature. hMSCs were then incubated with primary antibody in 1% bovine serum albumin (Table A-1) overnight at 4°C, followed by incubation with the appropriate secondary antibody at 1:500 in 5% goat serum for 2 hours at room temperature, and counterstained with Hoechst (Sigma Aldrich, 2μg/ml). For staining the actin cytoskeleton, cells were incubated with Alexa488-phallodin (1:40 v/v in PBS, Life Technologies) for 10 minutes followed by counterstaining with Hoechst (Sigma Aldrich, 2 μg/ml) for 20 minutes at room temperature. Imaging was performed with either a Nikon Ti inverted microscope (Nikon Instruments Inc., Melville, NY, USA) or a Zeiss LSM 710 confocal microscope (Carl Zeiss, Oberkochen, Germany), and images were processed with ImageJ (National Institutes of Health, Bethesda, MD, USA).

For flow cytometry, unstained hMSCs were used to set voltages for the fluorescence and scatter channels. Single-stained hMSCs were used to determine compensation values so that fluorescence signal within one channel was definitively from a positively-stained cell. Cells were then run on a FACS Calibur flow cytometer (BD Biosciences). Each experiment represents 10,000 gated cells, and data were analyzed by FlowJo software (Tree Star Inc., Ashland, OR, USA).

3.2.7 Quantitative Real-Time Polymerase Chain Reaction

hMSCs on spin-coated substrates were homogenized with the Trizol reagent (Life Technologies), mixed with chloroform (1:5 Trizol:chloroform), and separated by centrifugation (12,000x g, 15 min, 4°C). The RNA contained within the aqueous phase was then isolated with RNeasy columns (Bio-Rad, Hercules, CA, USA), according to the manufacturer's instructions. cDNA was synthesized using a kit (Applied Biosystems, Life Technologies), and qRT-PCR was performed with a SYBR Green master mix (Bio-Rad) with 15 – 20 ng cDNA and 500 nM each of forward and reverse primers, using a CFX Real-Time PCR System (Bio-Rad). The qRT-PCR protocol included: 95°C for 3 min, followed by 40 cycles of denaturation at 95°C for 30 seconds, annealing at 58°C 30 sec, and extension at 72°C for 30 seconds. The expression of each gene of interest was normalized to expression of glyceraldehyde 3-phosphate dehydrogenase (GAPDH) as a housekeeping gene, generating the $\Delta C(t)$ value, and expression of $2^{-\Delta\Delta C(t)}$ relative to the TCPS control with $n \geq 3$ biological replicates for each experiment was reported. Primer sequences are listed in Table A-2 and only those that showed single, specific amplicons were used for qRT-PCR experiments.

3.2.8 Statistical Analysis

Comparisons between two groups were performed with a Student's unpaired t-test. Comparisons between multiple groups were performed with a one- or two-way analysis of variance (ANOVA) with a Tukey *post hoc* test to adjust p-values for multiple comparisons. In all cases, $p < 0.05$ is considered statistically significant. Mean ± standard deviation is reported, unless otherwise noted.

For multivariate analysis, all computation work and graphical outputs were performed in R statistical software. Specific tests and analyses conducted are described in the results section.

3.3 Results

3.3.1 Physicochemical Substrate Properties on the PEG-PCL-cPCL Library

We first employed 2D copolymer substrates consisting of three subunits (Figure 3-1A): PCL, which is hydrophobic and protein adsorptive; PEG (2kDa chain length), which is hydrophilic and cell-repellant; and carboxylated-PCL (cPCL) which is hydrophilic but interacts favorably with proteins. We included cPCL as a material "rescue" against the repellant effect of PEG; comparing two materials with the same PEG mol%, but with and without cPCL, allows us to better understand how PEG repellency modulates stem cell behavior. Protein adsorption (Figure 3-1B) and contact angle (Figure 3-1C) were controlled by altering the mol% PEG, with increasing PEG content resulting in more hydrophilic, protein-repellant surfaces; this effect was counteracted upon inclusion of cPCL. Surface moduli were constrained between 2 and 18 kPa to mitigate stiffness influences on cell behavior (Figure 3-1D). Surface roughness increased when either PCL or cPCL content was added to PEG, thereby confirming the hydrophobic surfaces were entropically ruffled due to semi-crystalline formations (Figure 3-1E). However, it should be noted that when more PEG was added, the surface roughness increased likely due to competitive packing between PEG and PCL/cPCL subunits.

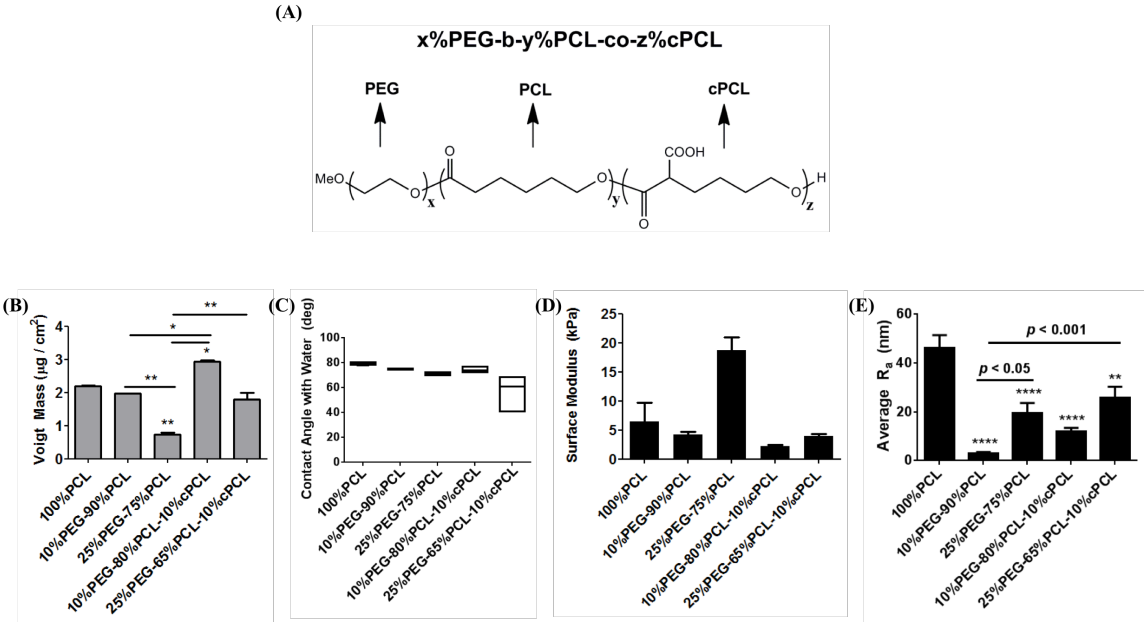

Figure 3-1 Chemical Structure and Material Properties of the Ter-Polymer Library. **(A)** Schematic representation of the copolymer structure, including hydrophobic and cell-adhesive PCL, hydrophilic and cell-repellent PEG, and hydrophilic and cell-adhesive cPCL. **(B)** By varying the molar percentage of each subunit, the protein adsorption on spin-coated surfaces was controlled. Increasing PEG content resulted in a more repellent surface, but inclusion of the cPCL component increased protein binding. **(C)** Contact angle measured by goniometry demonstrates that increasing PEG and cPCL content in the copolymer backbone results in a more hydrophilic surface. **(D)** Surface modulus measured by atomic force microscopy confirms that copolymers exhibit values that fall within a range not expected to heavily influence cell behavior. **(E)** Surface roughness measured by a one-dimensional profilometer demonstrates that PEG incorporation increased surface roughness, with supplemental increase with cPCL. All bars are mean ± S.D. *$p < 0.05$, **$p < 0.01$, ***$p<0.001$, ****$p<0.001$ relative to 100%PCL or as indicated between the lines.

3.3.2 hMSCs Phenotypic Response to the PEG-PCL-cPCL Library

hMSCs formed aggregates on PEG-PCL copolymers but spread on 100%PCL and cPCL-containing materials (Figure 3-2A), verifying the functional repellency of PEG and adhesiveness of PCL and cPCL. Increasing the mol% PEG further to 25%PEG-75%PCL resulted in large regions devoid of cell attachment after seeding, indicating this as the upper limit of cell repellency for further experiments. As was previously described, hMSC spheroids are representative of embryonic-like niches, which should have reduced ROS loads. ROS was subsequently measured in order to investigate if the morphological findings indicated any deeper biological changes occurring. Intracellular ROS (Figure 3-2B) decreased for hMSCs cultured on 100%PCL and decreased further on PEG-PCL, but returned to TCPS-equivalent levels on cPCL copolymers.

We next evaluated copolymer-mediated modulation of *NANOG* and *SOX2,* two fundamental stemness genes that maintain self-renewal and differentiation capacity.[172, 173] Confirming our hypothesis that repellency would modulate stemness, one copolymer - 10%PEG-90%PCL – induced a significant increase in expression of *NANOG* and *SOX2* relative to TCPS control (Figure 3-2C,D). Because 10%PEG-90%PCL had the greatest significant increase in pluripotency gene expression, we reconfirmed that ROS was also reduced as was demonstrated in a separate experiment (Figure 3-2B). Furthermore, expression of STRO-1, the most commonly used *in vivo* marker of undifferentiated hMSCs, is gradually lost during *in vitro* culture on TCPS[23], but was reinstated on 10%PEG-90%PCL (Figure 3-2F).

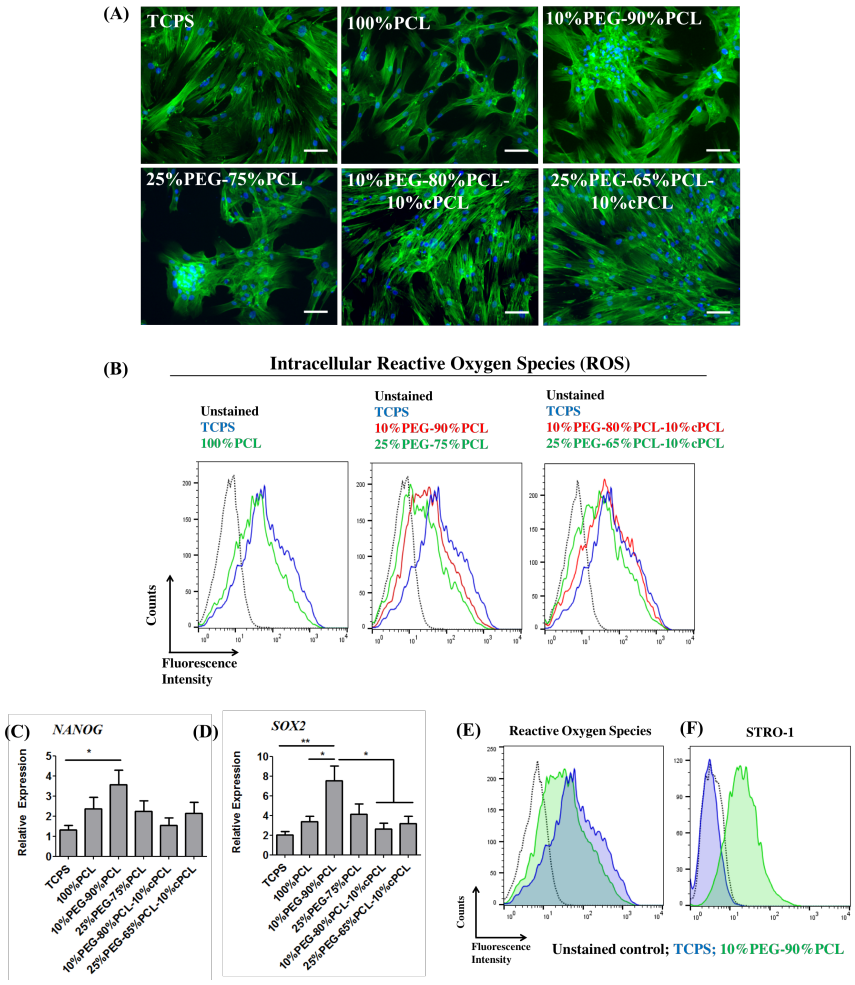

Figure 3-2 Pro-stemness and Low Redox Phenotype is Enhanced on 10%PEG-90%PCL.

(A) Cell attachment and spreading were heavily influenced by the substrate upon which they were grown. hMSCs on TCPS or 100%PCL attached and spread normally, but copolymers of PEG-PCL forced cells to aggregate, discouraging cell-matrix interactions; in contrast, hMSCs cultured on the PEG-PCL-cPCL copolymers appeared similar to those on TCPS and 100%PCL, demonstrating that the cell-repellent PEG subunit has a functional effect on cell behavior (green – phalloidin, blue – Hoechst; scale bars = 100 μm). **(B)** Intracellular reactive oxygen species (ROS) quantification by flow cytometry shows that hMSCs cultured on TCPS or 100%PCL carry similar ROS loads; in contrast, PEG-PCL materials stimulate a reduction in ROS levels, but cells cultured on cPCL-containing polymers exhibit an ROS profile similar to that of TCPS. The gene expression of the core stemness genes **(C)** *NANOG* and **(D)** *SOX2* was modulated by culture on the test substrates (n = 5). Furthermore, the accumulation of intracellular ROS **(E)** was decreased on 10%PEG-90%PCL, relative to TCPS, as indicated by the fluorescence of the ROS-sensitive DCFDA dye. **(F)** The expression of STRO-1, an *in vivo* marker of undifferentiated hMSCs in the bone marrow, was lost during culture on TCPS but was reinstated following three-day culture on 10%PEG-90%PCL. All bars are mean ± S.D. $*p < 0.05$, $**p < 0.01$ relative to TCPS or as indicated between the lines.

3.3.3 Validating Surface Chemistry as the Primary Driver for hMSC Response

Previous studies have implicated specific material properties in regulating hMSC behavior[133-135] and we analyzed how stemness gene expression was influenced by physicochemical parameters. Figure 3-3A presents the correlation matrix that shows the bivariate linear association between shear modulus, elastic modulus, contact angle, Voigt mass, *NANOG* and *SOX2*. The results indicate that contact angle and roughness produces relatively largest effects for *NANOG* and *SOX2*. In particular, contact angle had a consistent positive impact on *NANOG* and *SOX2*, whereas roughness' effect for them remained negative. On the other hand, voight mass, shear modulus, and elastic modulus affected the outcomes (i.e., *NANOG* and *SOX2*) in inverse fashion in smaller magnitudes. Results from significance testing were deemed uninformative and not reported here as the test involved a small sample size ($N = 15$).

Exploratory factor analysis (EFA) continued to explore for a parsimonious model by collapsing potentially redundant predictors. Examination of the correlation matrix suggested eliminating shear modulus and elastic modulus from the model considering the relatively small impact for the outcomes and their strong association with Voight mass. Accordingly, the remaining variables including contact angle, surface roughness, *NANOG*, and *SOX2* entered the model. These factors were further extracted using principal component analysis (PCA) as shown in Figure 3-3B. The strongest correlation was between the material contact angle and hMSC expression of *NANOG* and *SOX2*; relatively weaker correlations with roughness and Voigt mass were also observed.

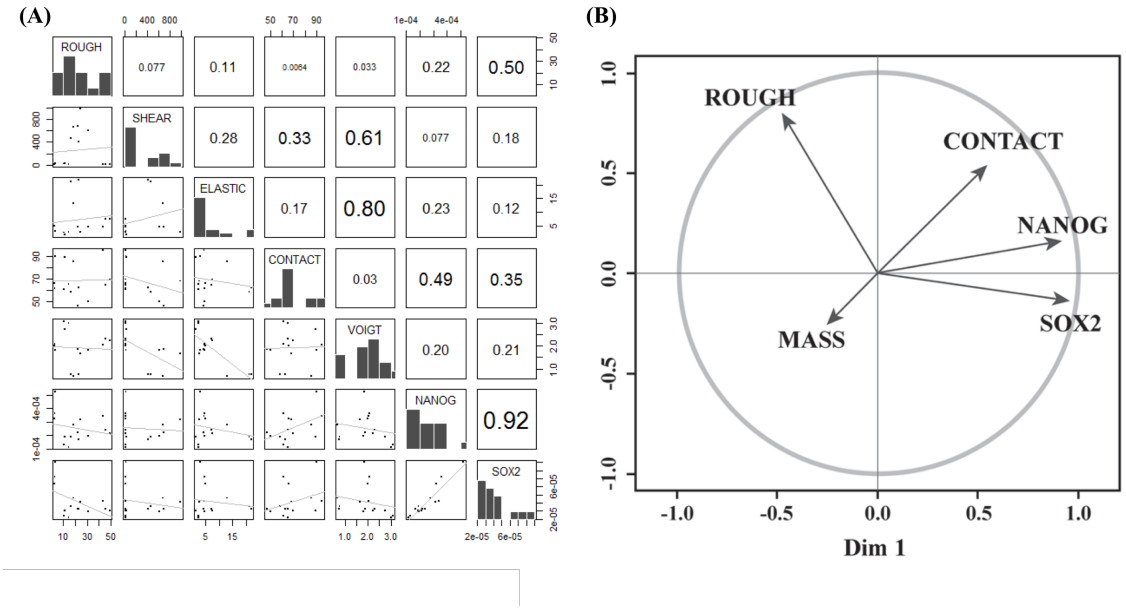

Figure 3-3 Stemness Gene Expression Has Specific Correlations with Material Properties.
(A) A PCA matrix across all measured material properties and stemness gene expression was compiled for Pearson correlation values. **(B)** Three material variables (roughness, contact angle and Voigt mass) were plotted on the first two principal components along with *NANOG* and *SOX2*. Contact angle was correlated with stemness gene expression while roughness and Voigt mass were anticorrelated, and these findings align with the functional properties of PEG when mol% is increased.

To confirm that the chemical elements of the copolymers were driving the hMSC phenotype change, copolymer surfaces were then pre-coated with adhesive collagen I, laminin or fibronectin (**FN**) at varying concentrations to mask the repellent domains without changing copolymer composition. Only the lowest concentration of FN tested (0.05 μg/cm^2) retained the material-induced increase in *NANOG* and *SOX2*, but this effect was lost as FN content increased (Figure 3-4). All concentrations of collagen I or laminin resulted in a complete attenuation of stemness expression.

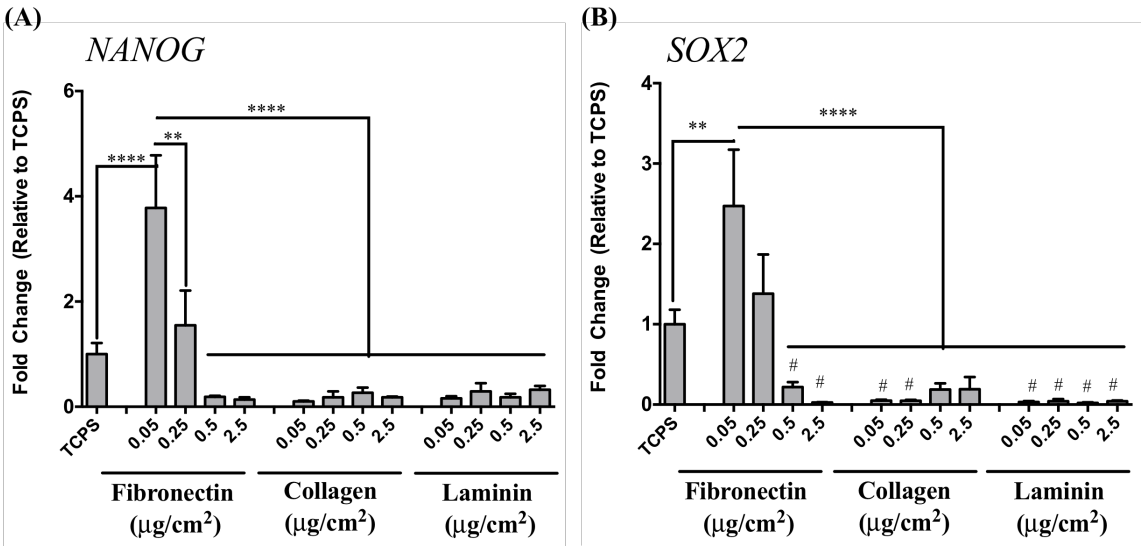

Figure 3-4 Covering the Copolymer Surface with ECM Protein Abrogates Increased Stemness Gene Expression.
To prove that surface repellency is required to modulate stemness, 10%PEG-90%PCL was pre-coated with fibronectin (FN), collagen I and laminin at various concentrations before culture. The expression of **(A)** *NANOG* and **(B)** *SOX2* was regulated by the surface repellency (n = 4). At the lowest FN concentration, 10%PEG-90%PCL copolymers promoted expression of stemness genes that was similar to that of substrate-free hanging drop (HD) cultures (data not shown); however, as FN concentration increased, cell attachment and spreading increased, and the increased stemness effect was lost. The same effect was seen for all concentrations of collagen I and laminin. All bars are mean ± S.D. $^{**}p < 0.01$,$^{****}p<0.0001$. $\#p<0.05$ compared to TCPS.

Since PEG as the repellent copolymer subunit would restrict cell attachment, we hypothesized that abrogated effects of pre-coated PEG-PCL were due, at least in part, to a shifting bias toward cell-matrix interactions through enhanced accessibility to adhesive ligands. Because FN was the only ECM molecule that maintained increased pluripotency gene expression with low surface coating mass, we imaged the cell spreading progression at 8 and 72 hours post-seeding. As seen in Figure 3-5A, the concentration of FN at the PEG-PCL surface played a critical role in changing hMSC behavior. Cell aggregates formed on uncoated and 0.05 μg/cm^2 FN PEG-PCL after 8 hours (red arrows), but cells spread more readily on higher FN concentrations. After 72 hours, a similar effect was

observed with limited cell spreading on uncoated and 0.05 μg/cm^2 FN PEG-PCL but confluent cultures for higher concentrations (Figure 3-5B). These results verify that pre-coating the surface with ECM proteins promotes cell attachment and spreading, increasing cell-matrix interactions and diminishing the influence of the cell-repellant PEG-PCL material.

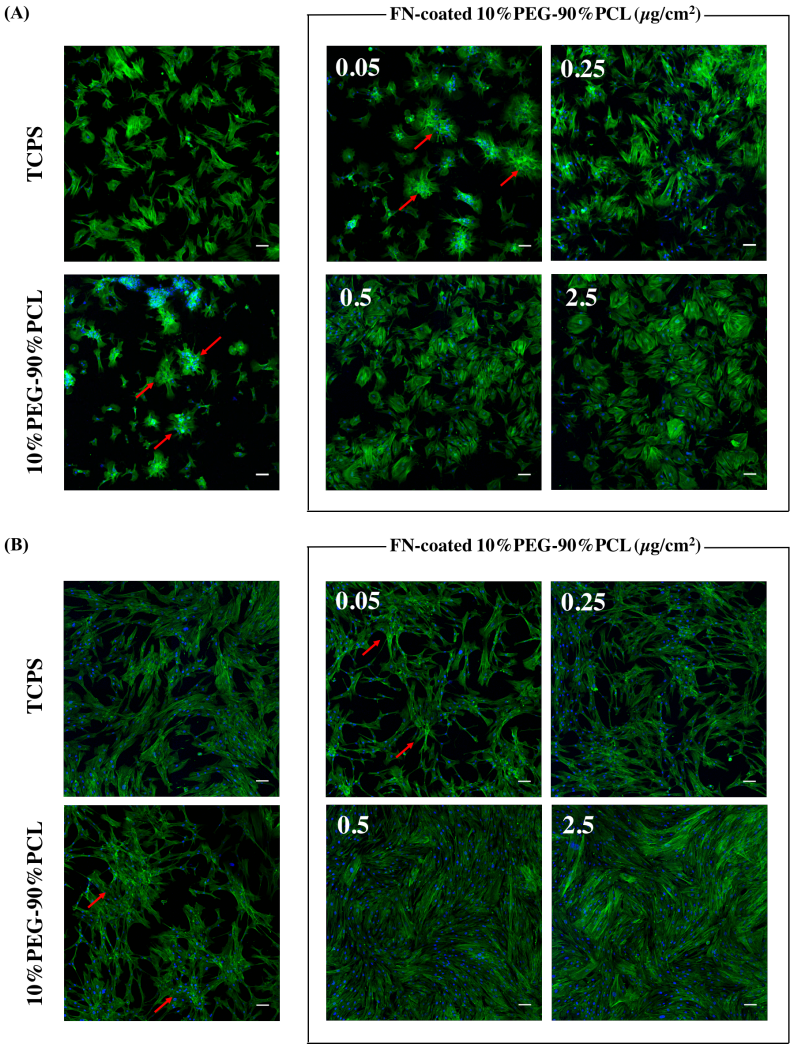

Figure 3-5 Increased Fibronectin Coating Induces Cell Spreading.
To prove that surface repellency is required to modulate stemness, 10%PEG-90%PCL was pre-coated with fibronectin (FN) at various concentrations before culture (green – phalloidin, blue – Hoechst; scale bars = 100 μm). On uncoated and 0.05 μg / cm^2 FN 10%PEG-90%PCL, hMSCs formed aggregates (red arrows) at **(A)** 8 hours and **(B)** 24 hours post-seeding. Increasing FN concentration enhanced cell attachment and spreading beyond what was observed on TCPS control.

3.3.4 Expanding the PEG-PCL Copolymer Library

A library of PEG-PCL was created given that cPCL compositions tested in the original copolymer library did not yield statistically significant increases in pluripotency genes nor performed well in terms of decreased ROS load. In the new copolymer library, the length and/or mol% of the PEG subunit within the copolymer backbone was tuned to further regulate the cellular response. Copolymers containing (i) 5 – 20 mol% PEG and (ii) block lengths of 750Da, 2kDa, or 5kDa were synthesized and characterized (Figure 3-6). hMSCs were cultured on these copolymers to determine the degree of repellency that the surfaces imparted on the cells with the aforemented altered PEG subunit variables. After four days in culture, PEG_{750} materials allowed attachment, although to a decreasing degree as PEG mol% increased (Figure 3-7A). This trend was more apparent on PEG_{2k} copolymers as > 10 mol% PEG inhibited attachment, and virtually no attachment was observed on PEG_{5k} copolymers. Four materials ($5\%PEG_{750}$, $20\%PEG_{750}$, $5\%PEG_{2k}$, and $10\%PEG_{2k}$) were chosen for remaining studies to represent two decoupled variables: (1) increased PEG chain size at a constant mol%, and (2) increased mol% with constant PEG chain size (Figure 3-7A-B, indicated by red letters).

hMSCs on PEG_{750} copolymers interacted with the surface and elongated, but cells on PEG_{2k} copolymers generated more isolated aggregates **(**Figure 3-7B). With respect to stemness genes, the expression of *NANOG* (Figure 3-7C) and *SOX2* (Figure 3-7D) were heavily influenced by both the PEG chain length and the mol%. *NANOG* expression was increased significantly on all copolymers, relative to TCPS control, with a subsequent increase on $10\%PEG_{2k}$. Interestingly, *SOX2* displayed a 'step-like' pattern. Copolymers comprised of longer PEG chains (2kDa versus 750Da) stimulated greater expression of *SOX2* genes, and the increased mol% of PEG within each group (10/20% versus 5%)

further enhanced this effect. On all copolymers, the expression of key antioxidative mediators, including sestrin 1 (*SESN1*), superoxide dismutase 2 (*SOD2*), thioredoxin (*TRX*), and apurinic endonuclease/redox-factor 1 (*APE/Ref-1*), was increased (Figure 3-8A-D), and both intracellular ROS load (Figure 3-8E) and cell proliferation (Figure 3-9) were significantly reduced, relative to TCPS.

PEG Mw (Da)	PEG mol%	PCL mol%	Mn (kDa)	Mw (kDa)	PDI
750	5.6	94.4	40.89	69.32	1.70
	7.3	92.7	35.17	56.77	1.61
	9.9	90.1	31.97	53.18	1.66
	12.9	87.1	24.11	40.47	1.68
	16.8	83.2	17.70	25.27	1.43
	20.6	79.4	17.33	28.34	1.64
2000	5.5	94.5	110.31	179.77	1.63
	7.1	92.9	90.65	153.27	1.69
	9.3	90.7	80.64	130.44	1.62
	12.5	87.5	62.59	102.67	1.64
	18.2	81.8	41.63	71.50	1.72
	21.5	78.5	36.04	59.80	1.66
5000	5.5	94.5	119.12	196.80	1.65
	7.8	92.2	92.70	157.36	1.70
	9.2	90.8	110.36	179.76	1.63
	13.5	86.5	93.79	128.73	1.37
	17.5	82.5	56.69	94.78	1.67
	21.5	78.5	72.90	122.34	1.68

Figure 3-6 Characterization of New PEG-PCL Copolymer Library.
Highlighted in yellow are the copolymers chosen for biological experiments. The PEG mol% is rounded to the closest 5% in the main text and all figures for simplicity (such as, 5%PEG_{750}, 20%PEG_{750}, 5%PEG_{2k}, and 10%PEG_{2k}).

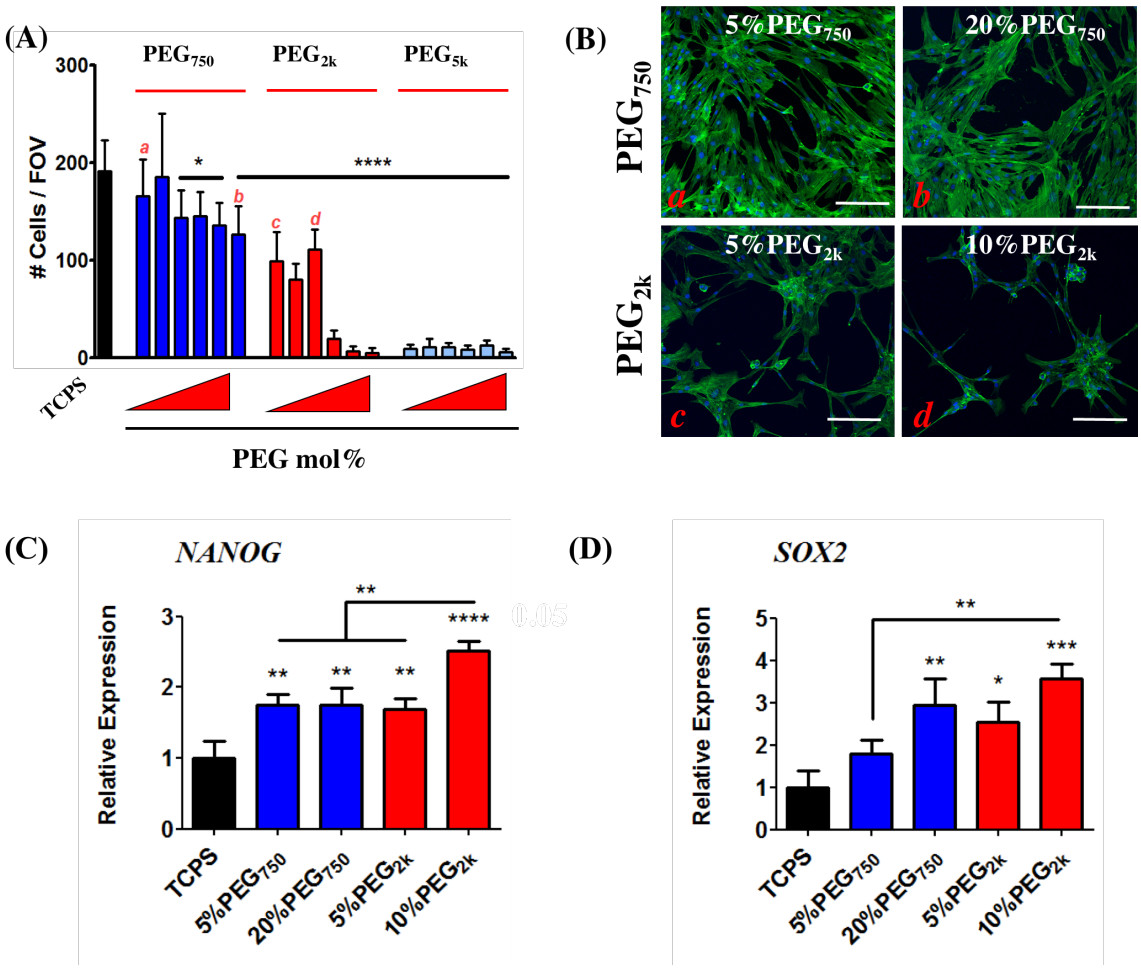

Figure 3-7 Tuning PEG Chain Length and Mol% Regulates Cell Attachment and Stemness Gene Expression.

(A) Cell attachment could be tuned by varying the PEG mol% and/or chain length within the copolymer. All 750Da PEG copolymers (PEG_{750}) and 2kDa PEG (PEG_{2k}) ≤ 10 mol% maintained hMSC attachment whereas PEG_{2k} copolymers > 10 mol% and the entire 5kDa PEG (PEG_{5k}) library prevented cell attachment. Therefore, four materials (indicated by the red letters) were chosen as they offered the greatest range of PEG mol% and/or PEG chain length without completely preventing cell attachment. **(B)** hMSCs cultured on PEG_{750} copolymers attached and elongated, but still formed aggregates (*a*: 5%PEG_{750} and *b*: 20%PEG_{750}). In contrast, at the same PEG mol% or less, PEG_{2k} copolymers discouraged cell attachment and promoted cell aggregation at the material surface (*c:* 5%PEG_{2k} and *d:* 10%PEG_{2k}). **(C-D)** PEG mol% percentage and chain length both affected the gene expression of stemness markers significantly. The expression of *NANOG* was enhanced on all copolymers relative to TCPS, with greatest expression on 10%PEG_{2k}. *SOX2* was higher on 20%PEG_{750} versus 5%PEG_{750}, and the increase in PEG chain length enhanced this effect further, with 5%PEG_{2k} expression higher than 5%PEG_{750}, and 10%PEG_{2k} higher than 20%PEG_{750} (n = 3). All bars are mean ± S.D. *p < 0.05, **p < 0.01, ***p < 0.001, ****p < 0.0001 relative to TCPS or as indicated between the lines.

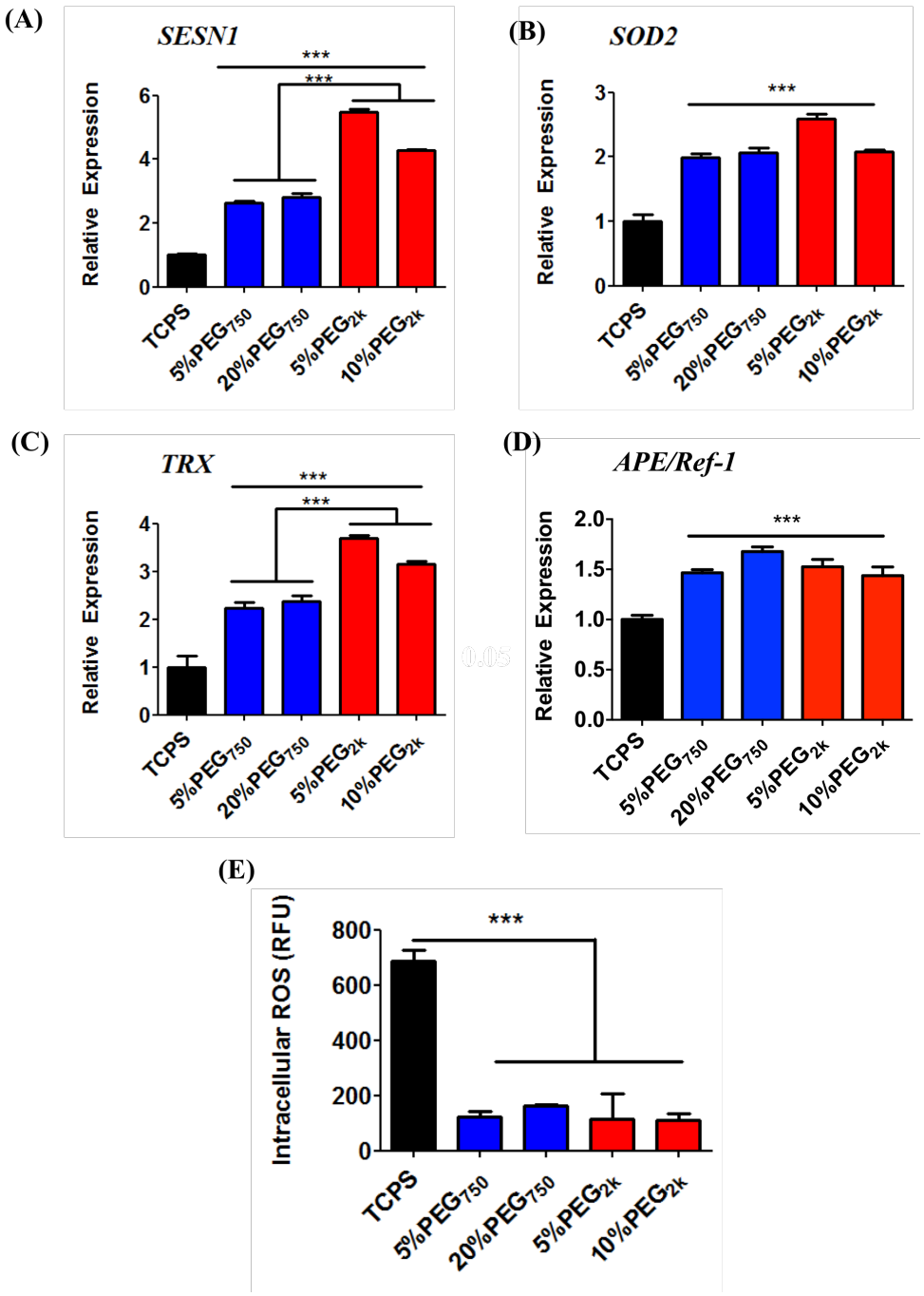

Figure 3-8 Tuning PEG Chain Length and Mol% Regulates Redox Potential.
The expression of anti-oxidative genes was enhanced significantly in hMSCs cultured on all test polymers, compared to TCPS control **(A-D)**. The expression of **(A)** *SESN1* and **(C)** *TRX* was further increased on PEG_{2k} copolymers (n = 3). **(E)** Enhanced redox gene expression was functionally-relevant as hMSCs from all copolymers exhibited significantly reduced intracellular ROS. All bars are mean ± S.D. ***$p < 0.001$ relative to TCPS or as indicated between the lines.

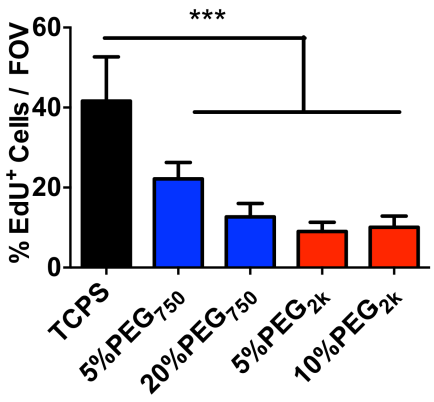

Figure 3-9 hMSC Proliferation Decreases on Select Copolymers.
The degree of cell proliferation was significantly decreased on all select copolymers, an expected association with pro-stemness environments. All bars are mean ± S.D. ***$p <$ 0.001 relative to TCPS.

3.4 Conclusions

In this Aim, copolymer comprising of subunits that modulate surface repellency were synthesized and fabricated into thin films for hMSC cell culture. As evidenced in the physical characterization data, adjusting molar ratios of PEG and cPCL in the copolymer backbone resulted in changed surface repellency (increase and decrease, respectively). An upper threshold of 25%PEG was determined as the ceiling molar ratio before surface repellency could not be overcome by the hMSCs. Surprisingly, when hMSCs were cultured on an optimal PEG-PCL surface (10%PEG-90%PCL), a known *in vivo* surface antigen only expressed by hMSCs present in the bone marrow was reactivated. Concurrently, gene expression of both *NANOG* and *SOX2* were upregulated and ROS load was decreased. Pre-coating the polymer surface with ECM proteins were found to abrogate the new hMSC phenotype and statistical analysis demonstrated contact angle being most correlated and adsorbed protein mass plus roughness being least correlated with stemness gene expression.

Further tuning of the PEG-PCL library through alteration of PEG molecular weight and PEG/PCL mol% uncovered hMSC sensitivity to copolymer composition beyond the original library first used in cell studies. Higher PEG content by either PEG block size and/or mol% resulted in more dramatic decrease in ROS loads and increased stemness gene expression. Moreover, cell proliferation decreased on the copolymers, thereby marking hMSCs adopting more 'stem cell-like' phenotype where cell division is typically decreased in stem cell reservoirs.

Chapter 4: Aim 2

4.1 Introduction

We next sought to determine the nanoscale structure-function relationship that drives these changes. In a previous study, PEG chains copolymerized with hydrophobic repeating units (e.g. tyrosine-derived polymers) segregated into nanoscale phase domains, thereby creating unique spatial patterns of PEG-mediated repellent surface that modulates adhesion of proteins and cells[174]. This event was previously investigated using small-angle neutron and x-ray scattering techniques where the spectra allowed for quantified nanoscale distribution of the hydrophobic and hydrophilic domains on such[174, 175]. Moreover, the surface roughness observed in atomic force microscopy measurements was thought to be the result of minor phase separation and/or hydration and swelling. These resulting surface clusters were thus speculated to determine protein adsorption and subsequent cell attachment. Unfortunately, the nanoscale phase behavior effect on intracellular behavior and functional activities were not evaluated.

Nanoscale analysis to explain the phase behavior of copolymer composition and its effect on cellular interaction is lacking in the field likely due to technical limitations to observe nanoscale changes in polymer phase behavior and subsequent changes in molecular presentation of cells in contact with the polymer substrates. Therefore, we utilized small-, medium-, and wide-angle x-ray scattering (SAXS, MAXS, WAXS**)** to study phase behavior of the copolymers, and how this might explain the observed hMSC response[176, 177]. We also employed super resolution imaging to confirm cell adhesion machinery was organizing in patterns that would indicate cell recognition of the phase behavior described by x-ray scattering.

In order to provide better context of these techniques, brief backgrounds are provided below.

4.1.1 Brief Background on X-Ray Scattering

X-rays are a form of electromagnetic radiation that comprises part of the electromagnetic spectrum (Figure 4-1). Originally discovered in 1895 by Wilhelm Röntgen, for which he was awarded the Nobel Prize in physics, x-rays were found to be critical in both basic science (e.g. astronomy) and real-world applications (e.g. medical imaging). X-rays are formed by shooting of electrons at a metal anode under high voltage, knocking out a lower orbital electron, and the higher energy orbital electrons release quantized energy as an x-ray when the the lower orbital vacancy is filled (Figure 4-2A). X-rays can also be formed by the sudden change in electron acceleration around a charged nucleus called Bremsstrahlung (Figure 4-2B). However, the phenomenon that is taken advantage of for the purpose of this thesis is x-ray scattering, and not the generation of x-rays themselves.

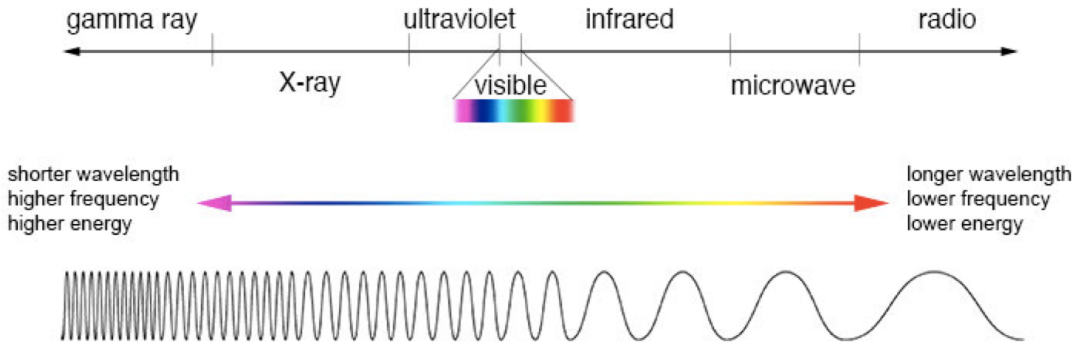

Figure 4-1 The Electromagnetic Spectrum.
Different types of electromagnetic radiation are illustrated in the figure. Wave of low energy (e.g. radio waves) have larger wavelengths and lower frequencies while the inverse is found in high energy waves (e.g. gamma rays). Adapted from [178].

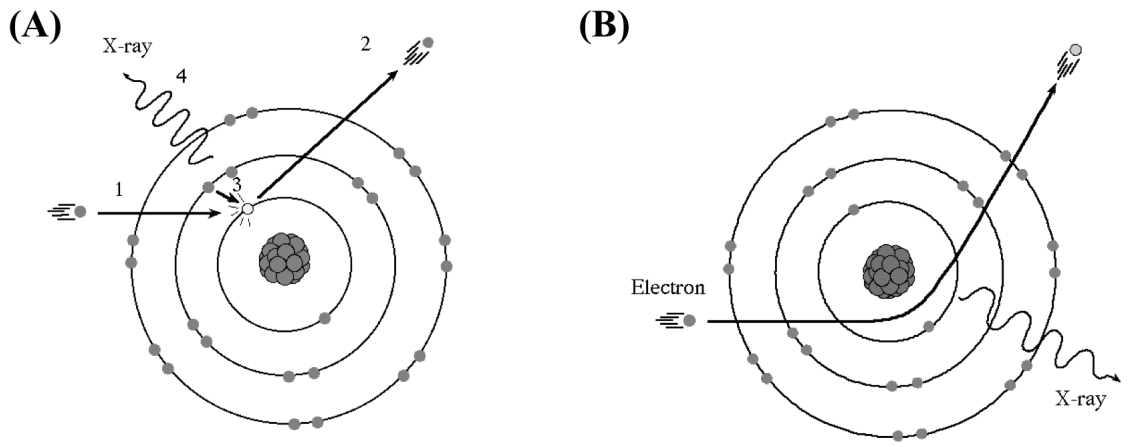

Figure 4-2 Two Common Mechanisms for Generating X-Rays.
(A) An incident electron (1) aimed at an electron in a lower shell displaces the low energy electron (2). The higher shell electron fills the valence by dropping down to the lower shell (3) and releases excess energy as an x-ray. **(B)** Bremsstrahlung is an event where an incident electron undergoes rapid deceleration change within a target atom and the excess energy is released as an x-ray. Adapted from [179].

Similar to the generation of x-rays, x-ray scattering can occur in two formats: elastic and inelastic scattering. In elastic scattering, an incident x-ray strikes an electron on a target atom and then is scattered as a spherical wave from the electron (Figure 4-3). In inelastic scattering, some of the energy is kept by the electron, and thus changes the phase of the scattered emanated x-ray. The most useful information from x-ray scattering typically comes from the elastic scattering category, and features of the substances subjected to incident x-rays are classified based on the scattering angle. Four divisions of scattering angles are ultrasmall angle x-ray scattering (USAXS), small angle x-ray scattering (SAXS), medium angle x-ray scattering (MAXS), and wide angle x-ray scattering (WAXS). Scattering angles beyond those covered by WAXS are collected by x-ray diffraction and other associated techniques.

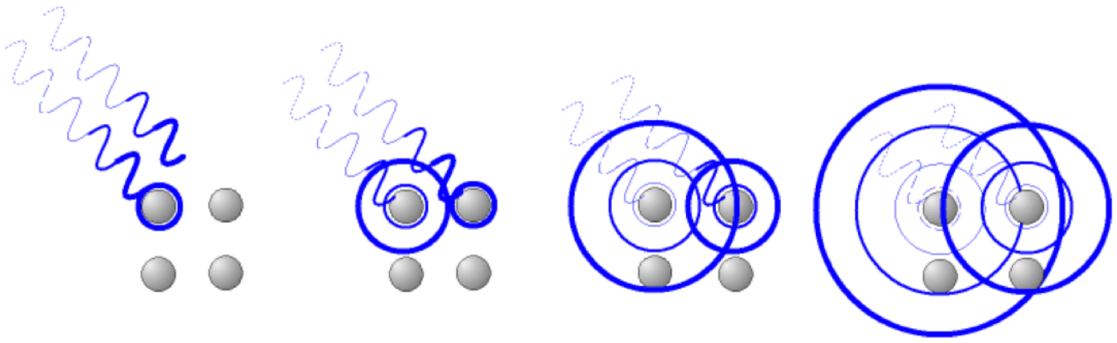

Figure 4-3 Wave Patterning of Scattered X-Rays.
X-rays that are focused on a specified target will encounter electrons and nuclei that scatter the waves. Upon hitting one of the aforementioned atomic constituents, the x-ray is converted from a one-dimensional wave to a spherical wave, which is detected by sensitive instruments in experimental setups. Adapted from [180].

SAXS has become one of the premier methodologies to elucidate very small features of materials as well as computationally developing three-dimensional maps of macromolecules (in solution) without the need for x-ray crystallography[181]. The general SAXS experiment is outlined in Figure 4-4. First, x-rays generated by a synchrotron source (e.g. device that accelerates electrons) are passed through one of the following: a bending magnet, undulator, or wiggler. Any of these devices create a dipole moment that makes the electrons oscillate and lose energy in the form of x-rays at very tuned wavelengths. These x-rays move through a beam line where it is defined, cleaned and collimated to the sample cell. When the x-rays strike the sample in the sample cell, the scattering x-rays hit a detector device, typically a CCD or imaging plate that has a beam stop to exclude non-scattered x-rays. In a typical experiment, an empty sample cell and sample cell with solvent are collected as background and control measurements, respectively, before collecting scattering data from actual solutions. Of note, only one-dimensional data is collected for SAXS on biological samples. MAXS data can be

collected from SAXS experimental runs, but other instruments are usually required for WAXS experiments.

When the scattering data is fully processed, different parts of the intensity curve can described features of the target sample. Several classifications are illustrated in Figure 4-5[182].

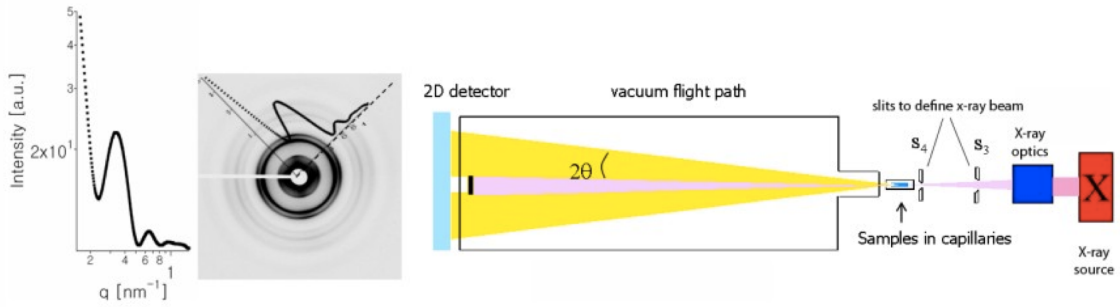

Figure 4-4 Schematic of X-Ray Scattering Experiment.
Moving from right to left, an x-ray source and collimated onto a sample target. Scattered x-rays strike the detector with the exception of the beam stop (pink shade), which prevents detection of unscattered x-rays. Examples on the left illustrate how raw data is converted into intensity plots for analysis. Adapted from [183].

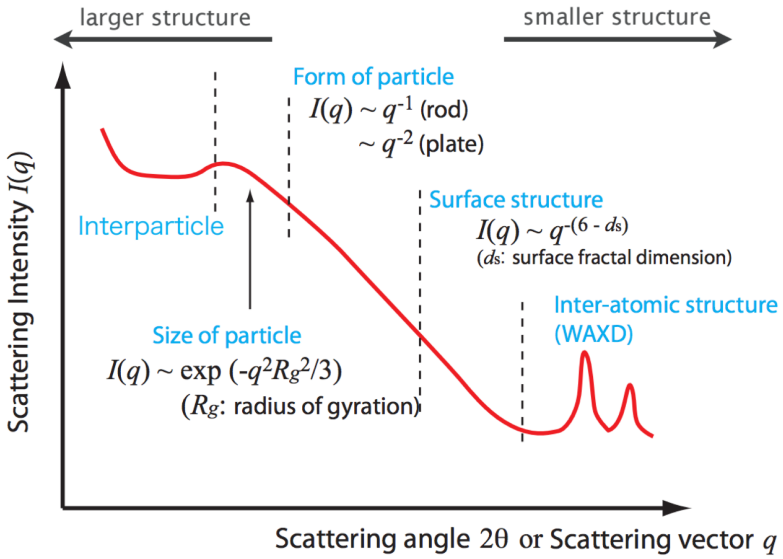

Figure 4-5 Structural Features of an X-Ray Scattering Plot.
A list of features and example curve-fitting equations are provided to illustrate the dynamic range of analysis that can be extracted from raw x-ray scattering data. Adapted from [182].

4.1.2 Brief Background on Structured Illumination Microscopy

Several different super resolution microscopy techniques have come to the forefront of biological research over the past several decades. Several modes used include structured illumination microscopy (SIM), saturated structured illumination microscopy (SSIM), stimulated emission depletion microscopy (STED), photoactivated localization microscopy (PALM) and stochastic optical reconstruction microscopy (STORM). The advent of these tools recently garnered recognition with the Nobel Prize in chemistry in 2014. This thesis work used SIM and the brief overview of SIM concepts are reviewed below.

SIM works by shining light onto a sample through different patterned gradients that can rotate about an axis[184]. When light passes through the gradients, the interference pattern is measured, otherwise known as a moiré patter (Figure 4-6). In order to amplify the resolution, non-structured illumination was introduced and more features could be spatially resolved as the saturated point for different pixels varied over time[185]. For all the fringe patterns obtained, computational algorithms stitch together a final image via Fourier analysis (frequency space to spatial space) (Figure 4-7)[186]. Additionally, no modified fluorophores or special reagents are necessary to obtain images with this mode of microscopy other than the initial capital investment in the microscope itself. Many labeled components of cells can also be imaged in three-dimensional space, thereby exceeding the previous z-stack standards in confocal microscopy[187-190].

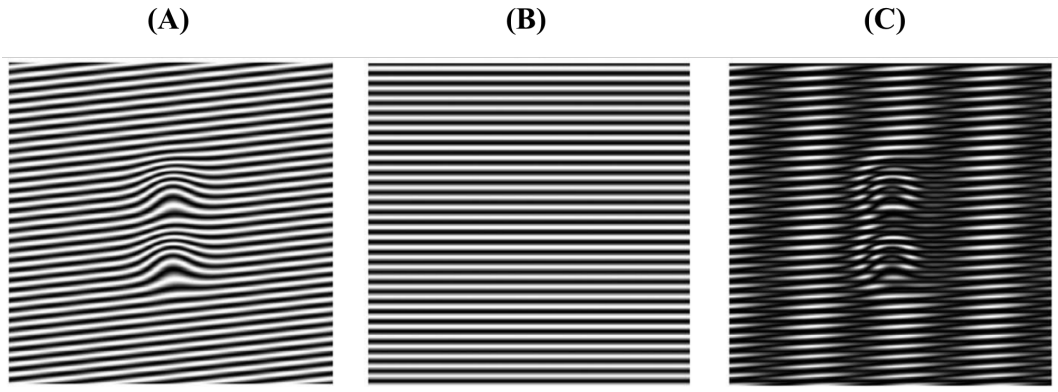

Figure 4-6 Moiré Patterning.
(A) A sample containing unknown structures. **(B)** A known structured patterned. **(C)** The moiré´ pattern generated by overlaying **(A)** and **(B)** Adapted with permission from [184].

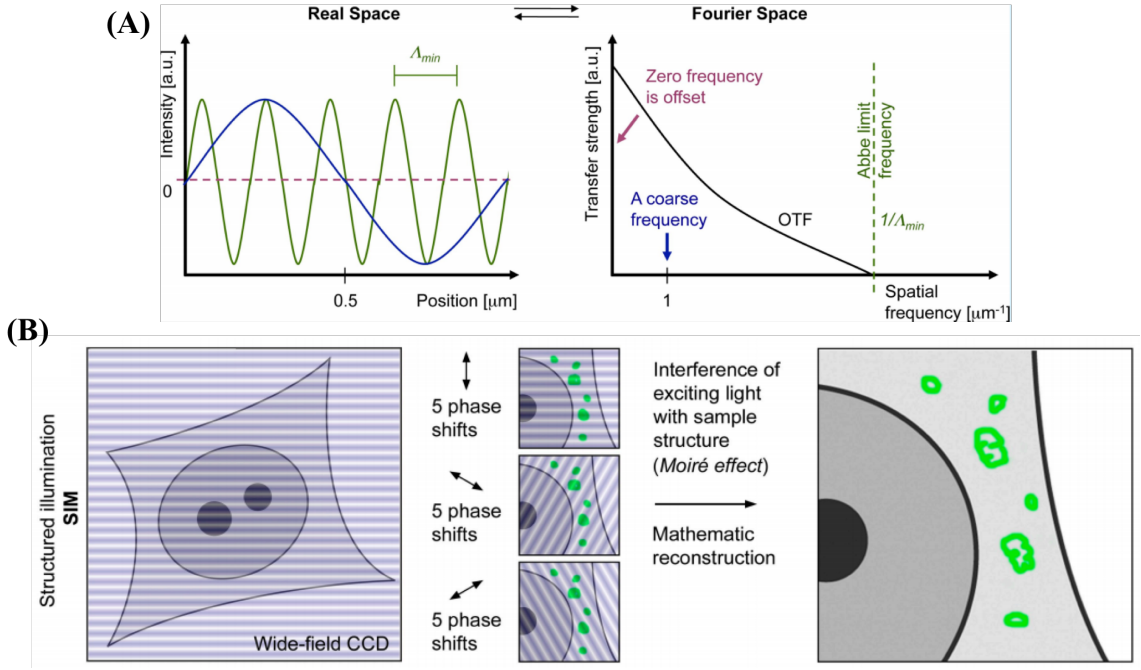

Figure 4-7 Illustration of Super Resolution Imaging Concepts.
(A) The ability to increase resolution in super resolution microscopes is based on convoluting real space data into Fourier space for each point. The graphs illustrate how the data are interchanged. **(B)** In SIM, the sample plane is excited by a non-uniform wide-field illumination. Laser light passes through an optical grating, which generates a strip-shaped sinusoidal interference pattern. This combines with the sample information originating from structures below the diffraction limit to genera moiré fringes. The image detected by the CCD camera thus contains high spatial frequency samples information shifted to a lower spatial frequency band that is transmitted through the objective. A mathematical reconstruction allows, from a series of 15 raw images per slice, to reconstruct a high-resolution image with a doubled resolution in x-y compared with wide-field resolution. Adapted with permission from [186].

4.2 Methods

4.2.1 Calculations for PEG Volume Fraction

PEG volume percent was calculated using three equations. First, PCL molecular weight for each copolymer was calculated using:

Equation 4-1:

$$\text{PCL } M_W = \text{Copolymer } M_W - \frac{\text{PEG mol\%} * \text{PEG } M_W}{100}$$

PEG molecular weight was taken from the manufacturer's data sheet and copolymer molecular weight reported by gel permeation chromatography. Weight percent of PEG or PCL in each copolymer was then calculated using:

Equation 4-2:

$$\text{PEG Wt\%} = \frac{100 * (\text{PEG mol\%} * \text{PEG } M_W)}{(\text{PEG mol\%} * \text{PEG } M_W + \text{PCL mol\%} * \text{PCL } M_W)}$$

Finally, PEG volume percent of each copolymer was calculated using:

Equation 4-3:

$$\text{PEG vol\%} = \frac{100 * \left(\frac{\text{PEG wt\%}}{1.234}\right)}{\left(\frac{\text{PEG wt\%}}{1.234} + \frac{\text{PCL wt\%}}{1.146}\right)}$$

where 1.234 and 1.146 are the densities (g/cm^3) of PEG and PCL, respectively.

4.2.2 Polymer Substrate Preparation

All polymers were synthesized as previously described [166]. Unless otherwise noted, all *in vitro* experiments were performed on spin-coated polymer films that were prepared with a commercial spin-coater (Laurell Technologies, North Wales, PA, USA).

15 mm circular glass cover slips (Fisher Scientific, Waltham, MA, USA) or 10 cm Pyrex Petri dishes (Corning Inc., Corning, NY, USA) were first cleaned with 100% ethanol (Sigma Aldrich, St. Louis, MO, USA), rinsed with dH_2O, and heated to 80°C for ~20 min to dry. A 1% weight/volume (w/v) solution of the specified polymer in tetrahydrofuran (THF, Sigma Aldrich) was spun for either 30 seconds at 3,000 RPM on glass cover slips (50 µl solution/sample) or 2 min at 1,500 RPM on Petri dishes (1 ml solution/sample). All samples were then exposed to constant cold-trap vacuum for ≥ 30 min to remove excess solvent and kept in a desiccator until use. For cell experiments, substrates were UV sterilized for 30-60 min on each side before use; for 15 mm cover glass, samples were placed in a 24-well plate, and secured with an autoclaved silicon O-ring (McMaster Carr, Atlanta, GA, USA).

4.2.3 X-Ray Scattering Experimental Protocol and Analysis

For x-ray scattering experiments, Pyrex petri dishes were spin-coated with 40% w/v copolymer solutions in THF. Each petri dish was spun twice to generate a film that could be peeled off the dish surface by hand and easily handled for transportation and cut to size for insertion into 2 mm quartz capillary tubes. X-ray scattering was performed before (dry condition) and after wetting by exposing polymers to phosphate buffered saline (PBS) for at least 6 hours. Small- and medium-angle x-ray scattering was performed at the Cornell High Energy Synchrotron Source (CHESS) facility in Ithaca, NY. The wavelength was 1.055 Å, and sample-to-detector distances were 1479 and 416 mm for small- and medium-angle scattering, respectively. Radiation damage was monitored by collecting 10 exposures, each of 4 second duration, and no radiation damage was observed. Small- and medium-angle x-ray scattering data were analyzed

using BioXTAS RAW 0.99.14b software (open-source on sourceforge.net). Wide-angle x-ray scattering data were collected on a Bruker area detector using Cu Kα radiation from a rotating anode and a sample-to-detector distance of 88 mm. These data were analyzed using JADE software (Materials Data Inc., Livermore, CA).

4.2.4 Cell Culture

hMSCs were either purchased from Lonza (Walkersville, MD, USA). hMSCs were maintained in complete media (CM) composed of alpha-minimum essential media with nucleosides (αMEM, Life Technologies, Carlsbad, CA, USA) with 16.7% fetal bovine serum (Life Technologies), 1% penicillin/streptomycin (Life Technologies), and 4 μg/ml plasmocin (InvivoGen, San Diego, CA, USA). Cells were kept in a humidified incubator at 37°C and 5% CO_2, and media was replaced twice each week. When ~80% confluent, hMSCs were detached with 0.05% trypsin-EDTA, re-seeded at a density of 100 - 500 cell/cm^2, and cultured for 7-14 days before reaching confluence. For all experiments, hMSCs (page < 6) were seeded at a density of 10,000 viable cells/cm^2, as determined by exclusion of Trypan blue, and cultured for three to four days.

4.2.5 Super Resolution Imaging

hMSCs were fixed with 4% paraformaldehyde (PFA, Sigma Aldrich) for 15 min at room temperature, washed three times with 1X PBS, and then permeabilized with 0.3% Triton X-100 (Sigma Aldrich,) for 5 min at room temperature. Primary anti-paxillin (Cat. #610051, BD Transduction Laboratories, Franklin Lakes, NJ, USA) and secondary AlexaFluor 568 goat anti-mouse (Cat. A11004, Life Technologies) antibodies were diluted in 10% bovine serum albumin (Sigma Aldrich) at 1:200 and 1:100, respectively, and centrifuged at 13000 RPM for 10 min before use. Samples were blocked in 10%

bovine serum albumin for 20 min at room temperature, and primary antibody incubation occurred at room temperature for 1 hour and 45 minutes, washed three times with 1X PBS, and then secondary antibody incubation for 1 hour at room temperature followed by three washes with 1X PBS. Cells were mounted in Vectashield (H-1000, Vector Laboratories, Inc. Burlingame, CA, USA) mounting medium. SIM imaging was performed on a GE Healthcare DeltaVision OMX equipped with a 60x 1.42 NA Oil objective and sCMOS camera. Images were collected from N=3 biological replicates with n≥3 images per replicate. SIM images with a maximum projection (in Z) of 3D acquisitions were analyzed using ImageJ (National Institutes of Health, Bethesda, MD, USA). Focal adhesion width was calculated using the ImageJ 1D line tool (width = 10) by drawing a line across the leading edge of the cell. A 1D plot of pixel intensity was generated live as the line was drawn to identify the focal adhesion regions within the plot. Full width at half maximum (FWHM) was used as the width measurement for each focal adhesion. The average from at least 40 cells from three images was reported for each group.

4.2.6 Statistical Analysis

Comparisons between two groups were performed with a Student's unpaired t-test. Comparisons between multiple groups were performed with a one- or two-way analysis of variance (ANOVA) with a Tukey *post hoc* test to adjust p-values for multiple comparisons. In all cases, $p < 0.05$ is considered statistically significant. Mean ± standard deviation is reported, unless otherwise noted.

4.3 Results and Discussion

4.3.1 X-Ray Scattering Elucidates PEG and PCL Domain Structure

X-ray scattering was performed on the entire copolymer library with the respective graphs show examples raw data curves obtained from the synchrotron (Figure 4-8). Peaks seen in the SAXS plot (Figure 4-8A) indicate that PCL exists as lamellae in the films, and that these crystalline lamellae are farther apart in the PEG_{2k} and PEG_{5k} copolymers than in the PEG_{750} copolymer (150 vs. 130 Å, Figure 4-8E); this was true at all mole% PEG used in this study. The MAXS curves (Figure 4-8B) show a PCL peak at $q=0.9$ $Å^{-1}$ along with its 002 reflection that has not been reported in the literature[191]. These two peaks were sharp in the PEG_{750} when dry but broad when wet, indicating that PCL chains are ordered when dry but disordered when wet. In contrast, this peak remains sharp in PEG_{2k} and PEG_{5k} copolymers when both dry and wet (Figure 4-8B), as PCL crystalline order remains unchanged upon hydration. The WAXS curves (Figure 4-8C) show the expected crystalline peaks indicated by their Miller indices overlaid on the amorphous scattering of the copolymer and water. Results of detailed profile analysis (Figure 4-8D) showed that the PCL crystallinity increases by ~20% upon hydration in the PCL, PEG_{2k} and PEG_{5k} samples, but not in the PEG_{750} samples. These results suggest that PEG_{750} is dispersed differently in the PCL matrix than the PEG_{2k} and PEG_{5k}, and may explain some of the differences observed in cellular responses between PEG chain sizes for these groups.

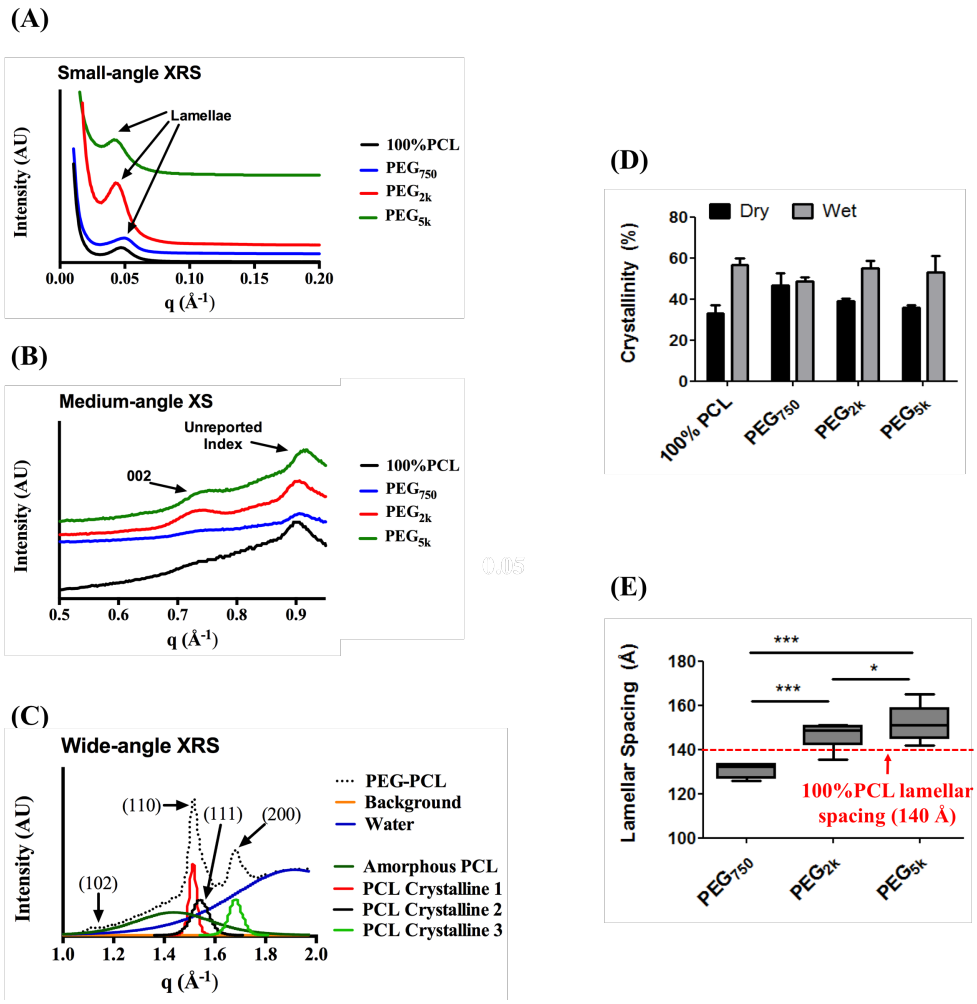

Figure 4-8 X-Ray Scattering (XRS) Reveals PEG Chain Length-dependent Nanoscale Characteristics at the Material Surface.
(A) Small-angle, **(B)** Medium-angle, and **(C)** wide-angle XRS confirmed the presence of PCL lamellae and crystalline structures, respectively, in all test copolymers (sample curves shown). Small-angle XRS data indicate that PEG chain length does not interfere lamellar formation. Medium-angle XS plot (wet) shows the broadening of the PCL peak upon hydration in the PEG_{750} copolymer sample, but this does not happen for 100%PCL, PEG_{2k}, or PEG_{5k}. This indicates that PEG_{750} copolymers are less ordered upon hydration, whereas the other three polymer samples become more ordered. Miller indices are shown by black arrows. Wide-angle XRS data demonstrate that the example curve of measured PEG-PCL spectra is the summation of signals from amorphous PCL, three peaks of crystalline PCL, and water. **(D)** PEG_{750}, but not PEG_{2k} or PEG_{5k}, prevented PCL crystallization under wet conditions, suggesting that PEG_{750} chains interdigitate within PCL domains whereas the longer PEG chains remain excluded, but mushroom out at the polymer-air/water interface. **(E)** Indeed, lamellar spacing data further support this claim. PEG_{2k} and PEG_{5k} chains swelled upon hydration, physically distancing the adjacent crystalline domains of PCL. All bars are mean ± S.D. $*p < 0.05$, and $*** p < 0.001$ between groups indicated by the lines.

Since PEG and PCL regions influence cell adhesion differently depending upon their locations in crystalline versus amorphous areas[192], it was crucial to find whether PEG domains were formed in PCL crystalline or amorphous areas. The presence of a SAXS lamellar peak confirmed that PEG does not interfere with this process in this copolymer format since the crystalline peaks associated with PCL remain unchanged at all PEG molecular weights. This result indicates that the PEG segments likely form phase-separated domains in the amorphous PCL area. The signature of these domains was not expected with PEG_{750} because PEG_{750} domains do not crystallize. Surprisingly, although PEG_{2k} and PEG_{5k} blocks are known to crystallize in copolymers, there was no evidence of PEG crystallinity even in the dry samples. Therefore, PEG_{2k} and PEG_{5k} chains are either interdigitated with the PCL chains in the amorphous space or they mushroom out at the polymer-air/water interface. Interdigitation, if present, is expected to disrupt the crystallization of PCL. We observed the opposite: the crystallinity of these samples is about the same as in PCL and increases to ~60% upon hydration. In contrast, the crystallinity increased with PEG_{750} when dry (47%) and did not change upon hydration (49%) (Figure 4-8D). MAXS peaks also show that PEG_{2k} and PEG_{5k} samples are more ordered. Thus, we conclude that PEG_{2k} and PEG_{5k} that are excluded from the crystalline PCL lamellae form a mushroom-like structure at the copolymer-water interface.[193, 194] This can also account for the increase in the lamellar spacing in these two copolymers upon hydration (150-155 vs. 140 Å); no such increase was observed with PEG_{750} (132 Å) (Figure 4-8E).

4.3.2 Consistent Volume Fraction of PEG Aids in Decoupling Molar Percent Ratio and Molecular Weight of PEG

To investigate how mole% PEG, instead of PEG chain size, influenced the film surface, the percent volume fraction of PEG was calculated for each copolymer in the library using the GPC data (Figure 4-9). The plot shows that the percent volume fraction of PEG was about the same for PEG_{750} and PEG_{2k} at each of the PEG concentrations. PEG_{5k}, likely due to the effect of chain size on copolymer synthesis, had markedly elevated percent volume fractions of PEG for all compositions. Because the films are approximately 100 nm thick, the volume fraction derived from bulk copolymer samples can be taken to represent the surface area fraction. Thus, the plot shows that the surface area of PEG coverage is the same for the three PEG sizes at the same molar ratio of PEG to PCL. This enables us to separate the effect of the PEG size from that of the PEG concentration on the observed cellular responses. As the PEG_{750} did not display large changes in the lamellar spacing or crystallinity (Figure 4-8D,E), and displayed disorder in the MAXS data shown (Figure 4-8B), it can be concluded that PEG_{750} stays embedded within the amorphous PCL. Yet, the volume fraction is too small ($x<0.5\%$) to completely cover the amorphous space between the crystalline PCL lamellae. Thus, with shorter PEG chains, PEG segments remain embedded in the amorphous PCL matrix, and the exposed amorphous PCL regions facilitate cell attachment. In contrast, based on the x-ray scattering data discussed earlier, we conclude that longer PEG chains form a local hydrated mushroom structure out of the non-crystalline regions of PCL.

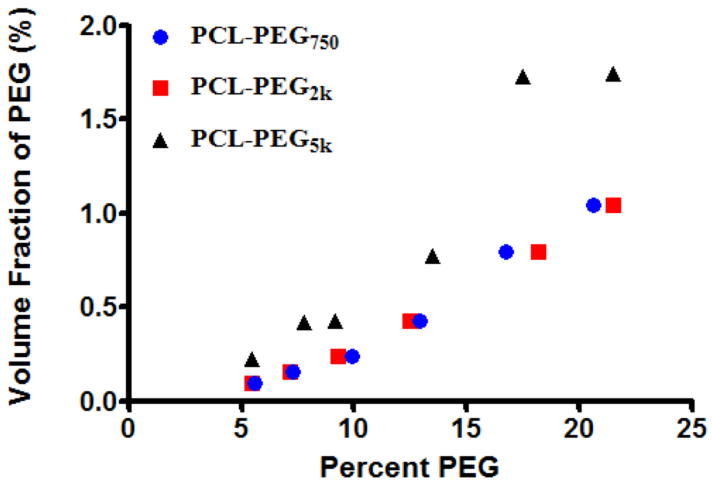

Figure 4-9 Volume Fraction of PEG in PEG-PCL Library.
Volume fraction of PEG, computed from gel permeation chromatography (GPC) data, for all copolymers synthesized in Figure 3-6. For copolymers with < 15 mol%, PEG_{750} and PEG_{2k} demonstrate similar vol% values, confirming that direct comparison between the materials is not skewed by the volume occupied by the PEG fraction.

4.3.3 Synthesis of X-Ray Scattering Data Justifying Degree of Cellular Attachment

The influence of nanoscale structural changes at the copolymer surface gleaned from the above data on the hMSCs is schematically illustrated in Figure 4-10. It has been previously shown that cells do not adhere to crystalline PCL areas, which make 60% of surface area on the films. Therefore, the hMSCs interact only with the amorphous PCL-PEG phase.[192] When the PEG size is increased, the amount of exposed amorphous phase PCL is relatively decreased while at the same time the size of the hydrated PEG domain is increased. Together, the larger PEG domains, especially PEG_{5k}, mask large areas of amorphous PCL from cell-matrix binding machinery. Hence, cell aggregation is induced in order for the cells to survive on the copolymer substrate. When the PEG chain is small (e.g., 750 Da), the numerous PEG domains are not large enough to block cell attachment.

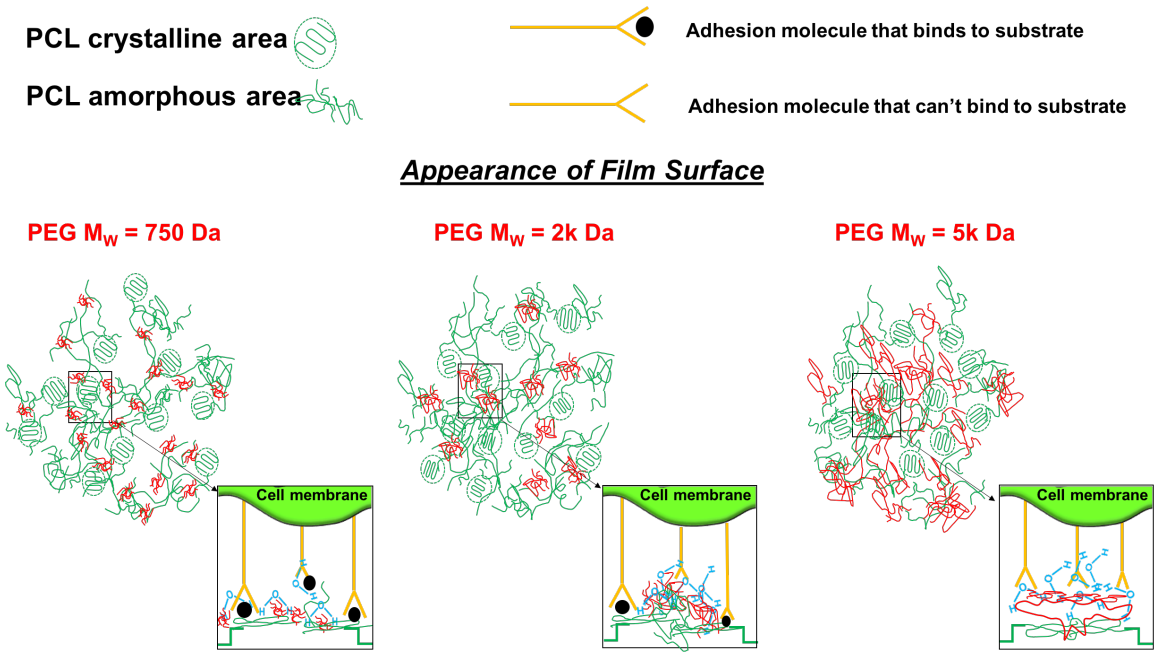

Figure 4-10 Schematic Synthesis of XRS Data and Cell-Material Interface.
In PEG_{750} samples, PEG chains remain interdigitated in the amorphous PCL matrix and cannot mobilize to the material surface upon wetting. This does not prevent cell attachment to the amorphous PCL. In contrast, larger PEG chains (PEG_{2k}, PEG_{5k}) are completely excluded from the PCL region, forming a loop that hydrates and swells, effectively mushrooming out and masking the adhesive PCL domains that cell attachment machinery cannot overcome.

4.3.4 Verification of Phase Separation by Super Resolution Microscopy of Focal Adhesions

In order to causatively link how changes in copolymer domain spacing influences cell attachment, we sought to visualize focal adhesion formation at the cell-material interface using Structured Illumination Microscopy (SIM)[185]. We used SIM to verify that hMSC attachment was influenced by exposure to limited amorphous PCL, and that this cell-biomaterial phenomenon was responsible for changing the subsequent hMSC behavior. Integrins are the main proteins involved in matrix adhesion, but there transient binding nature for stromal cell types such as hMSCs necessitates visualization of a more permanent and definitive marker. The mature focal adhesion marker protein, paxillin, was chosen for these purposes. Representative images found in Figure 4-11A confirm that the

PEG chains covering the amorphous PCL copolymer surface are causative for changes in focal adhesion formation in hMSCs as their structural morphologies are different. Quantification of the focal adhesion widths are reported in Figure 4-11B. Glass and 100%PCL control substrates had large focal adhesion sites resulting from the interaction between the hMSC and the culture substrate. Both 5%PEG_{750} and 20%PEG_{750} have a similar number of focal adhesions that also displayed the same morphology, thereby confirming that the steric hindrance of the PEG chain in these copolymers is unable to block amorphous PCL areas from formation of necessary integrin-matrix complexes. In contrast, both 5%PEG_{2k} and 10%PEG_{2k} show drastically different focal adhesion quantity and morphology. Focal adhesion morphologies portraying decreasing width and extending long axes has been documented to have more cell-induced force associated with them as a result of weak cell binding to the matrix[195-199]. Because the PEG domain sizes are increased, the reduction in amorphous PCL binding area is reflected with the thinner focal adhesion morphology with a compensated increased major axis length. Additionally, the striated pattern of the focal adhesions could be indicative of the spatial distribution of PEG in the amorphous PCL matrix.

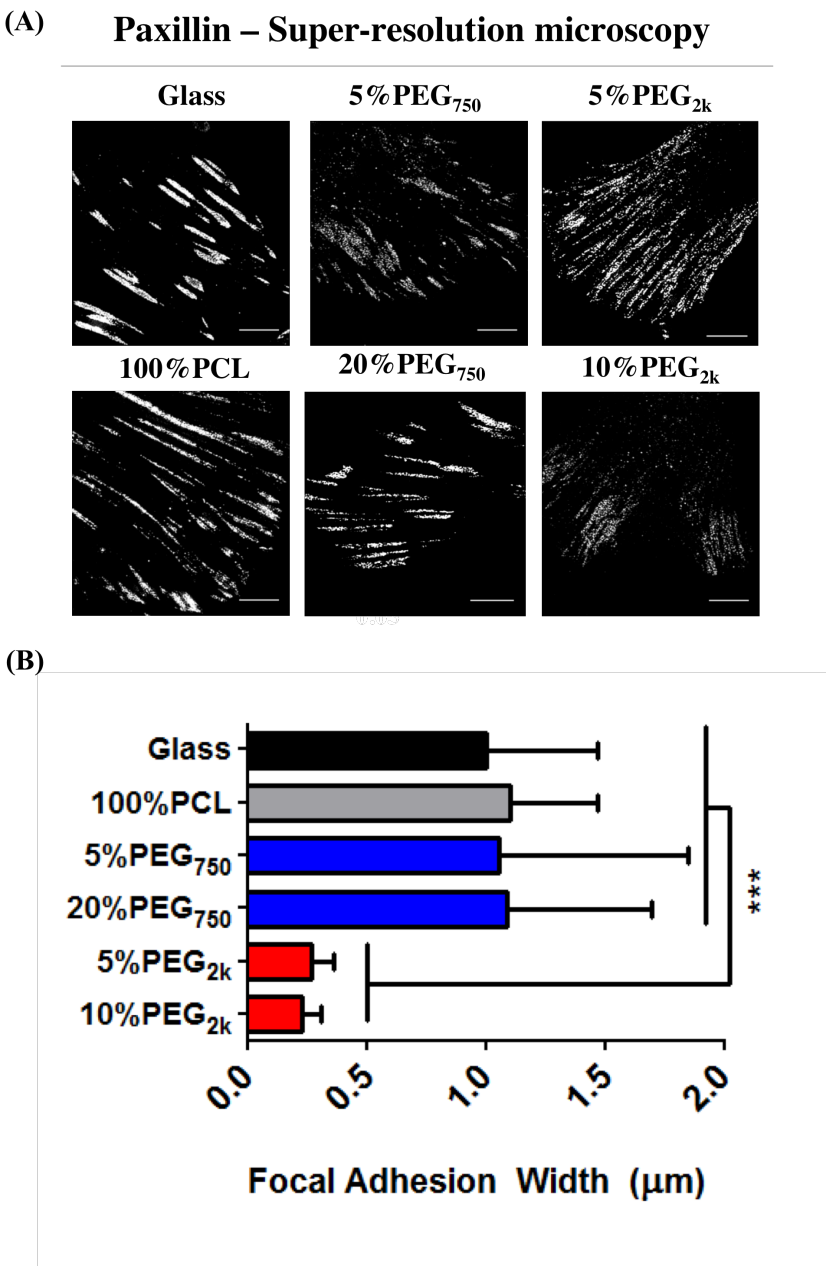

Figure 4-11 Focal Adhesion Morphologies are Compromised on Select Copolymers. **(A)** To interrogate how cells perceive the nanoscale surface, super resolution, structured illumination microscopy (SIM) was performed for the mature focal adhesion (FA) protein, paxillin. On glass and 100%PCL surfaces (i.e. fully adhesive, non-repellent), hMSCs formed thick, dense FAs. Similarly, on PEG_{750} copolymers, FA morphology and width remained similar to the adhesive controls; however, on PEG_{2k} samples, FAs were sparse with a compromised, thin morphology, suggesting weak cell-matrix interactions and supporting the presentation of PEG_{2k} chains at polymer-air/material interface (scale bars = 5 µm). **(B)** Quantification of FA width confirms similarity between glass, 100%PCL, and PEG_{750} samples versus PEG_{2k}. All bars are mean ± S.D. *** $p < 0.001$ between groups indicated by the lines.

4.4 Conclusions

In this Aim, we employed two high-resolution experiments to elucidate the cell-material interface. X-ray scattering from a synchrotron source demonstrated that the copolymers displayed phase separation between the PEG and PCL subunits. SAXS curves contained peaks that indicated PCL lamellae in the copolymer films for all the compositions. Specifically, this meant that all the sizes of PEG used in the copolymer library has phase separation with PCL domains. MAXS curves also showed peaks that indicated phase separation between PEG and PCL. Surprisingly, an unreported Miller index was discovered in the raw data curves that had not been in any previous literature available. WAXS curves had predicted Miller indices for PEG and PCL components. When these raw data curves were subjected to computational analysis, it was found that PEG_{750} copolymers has PEG components that interdigitated with the amorphous PCL while both PEG_{2k} and PEG_{5k} copolymers formed distinct PEG domains that masked the limited amorphous PCL on the film surface.

Validation of the x-ray scattering data with biological relevance was conducted using SIM. Immunostaining for the mature focal adhesion protein, paxillin, demonstrated that cell attachment machinery morphology was indeed altered on the different copolymer surface. These morphological changes were aligned with the x-ray scattering findings where larger PEG molecular weight components stressed the cell's ability to adhere to the amorphous PCL, as the focal adhesion widths were significantly thinner and more numerous.

Chapter 5: Aim 3

5.1 Introduction

Our next avenue of investigation was two-fold: (1) determine if the effect of the PEG-PCL substrate was universal across a larger body of hMSC donors, and (2) determine what protein or proteins at the cell-material interface are critical for the maintenance of hMSC stemness. The variability between donors for any cells or tissues exists for a variety of reasons. Some of the principle factors arise from the fact that all human beings have unique genomes, are exposed to different environmental conditions, and can develop a dynamic medical history. Commercial sources, like Lonza Walkersville, Inc, have strict criteria for donor cells. For example, hMSCs come from individuals between the age of 18 and 45, are of the male gender or non-pregnant females; have acceptable hematological vital signs; have general good health with no past history of chronic illness (e.g. heart disease, kidney disease, liver disease, cancer, epilepsy, and blood/bleeding disorders); and are negative for HIV, hepatitis B and hepatitis C[200]. As was alluded to in Chapter 2 and the introduction of Chapter 3, most patients who need regenerative therapies are of a more advanced age, which could generally be considered with a lower cut off of 65 years of age. These hMSCs are likely to have unique phenotypes compared to the donors between 18 and 45 years old. Even more, donors over 65 have likely started developing chronic illnesses. Hence, the efficacy of the PEG-PCL substrate should be tested on a population that not only is broader than those that commercial sources use but also select donors who would likely benefit most from regenerative medicine therapies requiring expansion of their bone marrow hMSCs.

With respect to the second part of this Aim's investigation, we desired to uncover what cell-cell and cell-matrix adhesion proteins may be modulated by the copolymer, and

if they were inhibited would the improved stemness phenotype be lost. Integrins play key roles in both cell signaling as well as cell adhesion to the ECM. Several types of integrins exist and dimerize to form functional macromolecular structures that can link with cytoskeletal machinery within the cell or set off a signaling cascade[201]. Similarly, a host proteins form adherens junctions between cells, such as cadherins, that serve to provide structural integrity between cells in a tissue as well as a conduit for signaling molecules to travel between cells[202-204]. Given the plethora of literature and biotechnology companies that seek to find chemical inhibitors of both integrins and cell-cell junction proteins, we subjected hMSCs to peptide and chemical inhibitors to find the causative protein(s) that initiate the phenotype change.

5.2 Methods

5.2.1 Polymer Substrate Preparation

All polymers were synthesized as previously described [166]. Unless otherwise noted, all *in vitro* experiments were performed on spin-coated polymer films that were prepared with a commercial spin-coater (Laurell Technologies, North Wales, PA, USA). 15 mm circular glass cover slips (Fisher Scientific, Waltham, MA, USA) or 10 cm Pyrex Petri dishes (Corning Inc., Corning, NY, USA) were first cleaned with 100% ethanol (Sigma Aldrich, St. Louis, MO, USA), rinsed with dH_2O, and heated to 80°C for ~20 min to dry. A 1% weight/volume (w/v) solution of the specified polymer in tetrahydrofuran (THF, Sigma Aldrich) was spun for either 30 seconds at 3,000 RPM on glass cover slips (50 µl solution/sample) or 2 min at 1,500 RPM on Petri dishes (1 ml solution/sample). All samples were then exposed to constant cold-trap vacuum for ≥ 30 min to remove excess solvent and kept in a desiccator until use. For cell experiments, substrates were

UV sterilized for 30-60 min on each side before use; for 15 mm cover glass, samples were placed in a 24-well plate, and secured with an autoclaved silicon O-ring (McMaster Carr, Atlanta, GA, USA).

5.2.2 Cell Culture

hMSCs were either purchased from Lonza (Walkersville, MD, USA) or acquired from patients at Vanderbilt University Medical Center in cooperation with Dr. Pampee P. Young, according to previously published methods.[205] hMSCs were maintained in complete media (CM) composed of alpha-minimum essential media with nucleosides (αMEM, Life Technologies, Carlsbad, CA, USA) with 16.7% fetal bovine serum (Life Technologies), 1% penicillin/streptomycin (Life Technologies), and 4 μg/ml plasmocin (InvivoGen, San Diego, CA, USA). Cells were kept in a humidified incubator at 37°C and 5% CO_2, and media was replaced twice each week. When ~80% confluent, hMSCs were detached with 0.05% trypsin-EDTA, re-seeded at a density of 100 - 500 cell/cm^2, and cultured for 7-14 days before reaching confluence. For all experiments, hMSCs (page < 6) were seeded at a density of 10,000 viable cells/cm^2, as determined by exclusion of Trypan blue, and cultured for three to four days.

5.2.3 Quantitative Real-Time Polymerase Chain Reaction

hMSCs on spin-coated substrates were homogenized with the Trizol reagent (Life Technologies), mixed with chloroform (1:5 Trizol:chloroform), and separated by centrifugation (12,000x g, 15 min, 4°C). The RNA contained within the aqueous phase was then isolated with RNeasy columns (Bio-Rad, Hercules, CA, USA), according to the manufacturer's instructions. cDNA was synthesized using a kit (Applied Biosystems, Life Technologies), and qRT-PCR was performed with a SYBR Green master mix (Bio-

Rad) with 15 – 20 ng cDNA and 500 nM each of forward and reverse primers, using a CFX Real-Time PCR System (Bio-Rad). The qRT-PCR protocol included: 95°C for 3 min, followed by 40 cycles of denaturation at 95°C for 30 seconds, annealing at 58°C 30 sec, and extension at 72°C for 30 seconds. The expression of each gene of interest was normalized to expression of glyceraldehyde 3-phosphate dehydrogenase (GAPDH) as a housekeeping gene, generating the $\Delta C(t)$ value, and expression of $2^{-\Delta\Delta C(t)}$ relative to the TCPS control with $n \geq 3$ biological replicates for each experiment was reported. Primer sequences are listed in Table A-2 and only those that showed single, specific amplicons were used for qRT-PCR experiments.

5.2.4 Inhibitor Study

hMSCs were exposed to various inhibitor concentrations for 48 hours to determine optimal concentrations. The following inhibitors and concentrations were used: 30 μM BTT 3033 (Integrin $\alpha_2\beta_1$ inhibitor, Tocris, Avonmouth, Bristol, United Kingdom), 30 μM P11 (Integrin $\alpha_v\beta_3/\alpha_v\beta_5$ inhibitor, Tocris) and 1 mg/mL GAP26 (Connexin-43 peptide-based inhibitor). GAP26 (Val-Cys-Tyr-Asp-Lys-Ser-Phe-Pro-Ile-Ser-His-Val-Arg) peptide was synthesized by standard solid-phase fluorenylmethyloxycarbonyl chloride chemistry on a Rink amide-MBHA resin using PS3 synthesizer (Protein Technologies, Tucson, AZ, USA). These peptides were cleaved and deprotected in trifluoroacetic acid/thioanisole/ethanedithiol/anisole (90/5/3/2). The formation of peptide was characterized by liquid chromatography-mass spectrometry (LC-MS) (Figure B-1).

For the inhibition experiment, the indicated concentrations of inhibitors were added to hMSC suspensions before seeding the cells onto the substrates. Cells were cultured for 4 days before harvesting RNA for gene expression analysis.

5.2.5 Measuring Levels of Intracellular Reactive Oxygen Species (ROS)

hMSCs were incubated with 10 μM 5-(and-6)-chloromethyl-2',7'-dichlorodihydrofluorescein diacetate acetyl ester (DCFDA) (Life Technologies) in serum-free DMEM for 30 minutes following the manufacturer's instructions. Cells were trypsinized and run on a FACS Calibur flow cytometer (BD Biosciences, Franklin Lakes, NJ, USA) with the appropriate unstained control. N=3 biological replicates were conducted per substrate condition. Data were analyzed by FlowJo software (Tree Star Inc., Ashland, OR).

5.2.6 Western Blot

Western blot analysis was done according to standard protocols[206]. Primary antibodies used in this study include: Integrin-α2 (1:200, sc-6586r, Santa Cruz Biotechnology, Dallas, TX, USA), Integrin-β3 (1:200, D7X3P, Cell Signaling Technologies, Danvers, MA, USA), Integrin-β5 (1:200, D24A5, Cell Signaling Technologies), Connexin-43 (1:200, #3512, Cell Signaling Technologies), and GAPDH (1:5000, 14C10, Cell Signaling Technologies) (Table A-1). Appropriate secondary antibodies from Li-COR (Lincoln, Nebraska, USA) were used to image the blots on the Odyssey imaging system according to the manufacturer's protocol.

5.2.7 Statistical Analysis

Comparisons between two groups were performed with a Student's unpaired t-test. Comparisons between multiple groups were performed with a one- or two-way

analysis of variance (ANOVA) with a Tukey *post hoc* test to adjust p-values for multiple comparisons. In all cases, $p < 0.05$ is considered statistically significant. Mean ± standard deviation is reported, unless otherwise noted.

5.3 Results and Discussion

5.3.1 Generating and Validating the Donor hMSCs

Donor hMSCs were obtained from patients at Vanderbilt University Medical Center in order to investigate if the effect of the copolymer has the same phenotype outcome from non-commercial cell sources. The cells purchased from Lonza have strict screening criteria as the commercial cell sources have to guarantee performance to anyone that purchases the cells for research purposes. However, because this screening criteria is so discriminatory, the ability to confidently state that the copolymer's usefulness in potential patient application is severely limited because Lonza hMSCs are not a randomly selected portion of the donor population. Hence, when screening to obtain donor hMSCs from Vanderbilt University Medical Center, very limited criteria was used. First, all donors were limited to being over 65 years of age. As most patients that would benefit from future tissue engineering therapies are of advanced age, proof of principle testing should utilize donors that are reflective of that population. Second, only male donors were selected. Because it is well known that steroid hormones cause significant physiological changes in hMSCs, their presence is hard to decouple if the donors were of both male and female genders. Moreover, related to the first screening criterion, the hormone levels are significantly altered for young and old donors[207]. Third, none of the male donors over 65 years of age could have known genetic blood disorders or known cancer diagnosis at the time of bone marrow harvest.

Confirming that the hMSCs obtained from the donor bone marrow were a pure population was paramount before conducting *in vitro* studies. Flow cytometry staining for three positive markers (CD74, CD90, and CD105) and four negative markers (CD14, CD20, CD34, and CD45) in a phenotyping kit was performed. As evidenced in Figure 5-1, all three donors exhibited the staining patterns predicted for both positive and negative stains. Hence, the hMSC isolation was deemed successful.

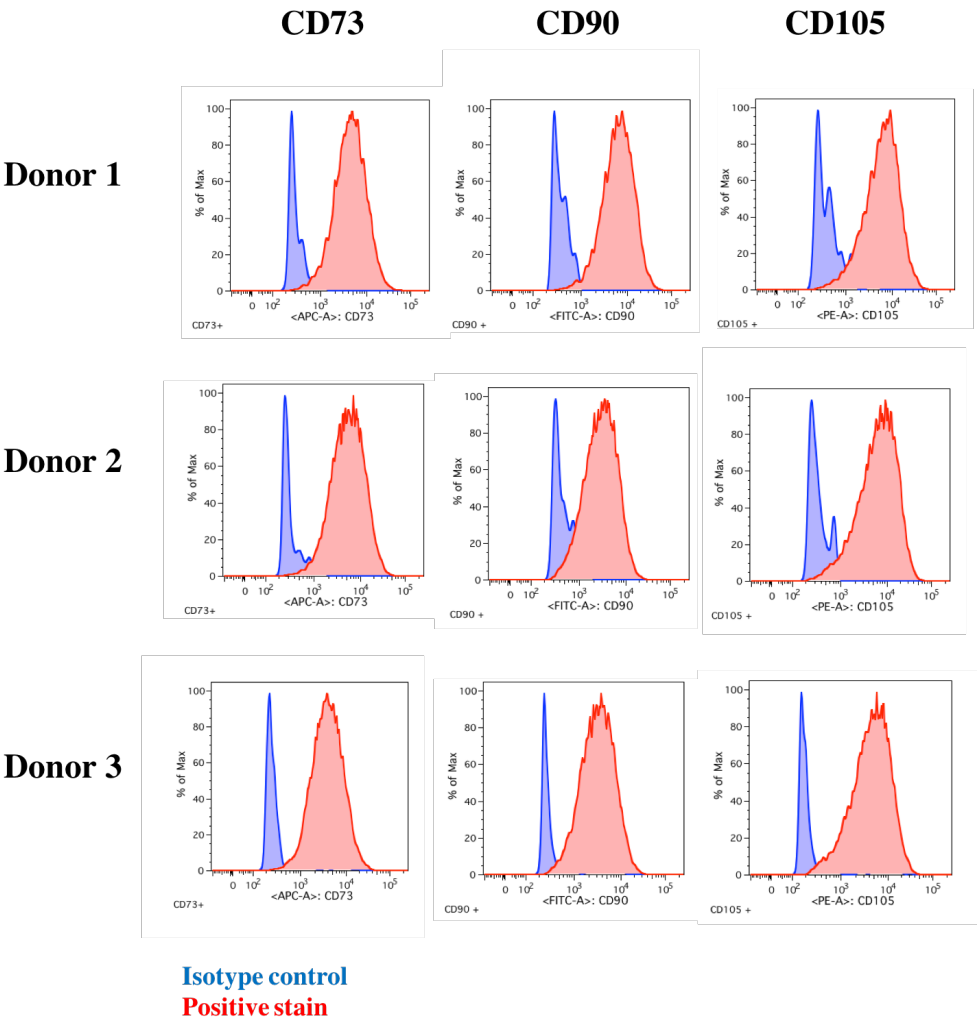

Figure 5-1 Flow Cytometry Verification of Isolated Donor hMSCs.
Flow cytometry analysis of marker expression of three patient-derived MSCs confirms the expected immunophenotype: $CD73^{+}CD90^{+}CD105^{+}$ > 95% for all tested samples.

5.3.2 Donor hMSCs Elicit Same Phenotype Response to PEG-PCL as Commercial hMSCs

To demonstrate that the effect of the material was not donor-dependent, hMSCs from the three patient sources were tested on the 5%PEG_{2k} copolymer since a strong cellular response was consistently observed on this substrate. For all donors, compared to TCPS, the expression of *NANOG* and *SOX2* was significantly increased on 5%PEG_{2k} (Figure 5-2A-C), and the expression of antioxidative genes was enhanced in virtually all cases (Figure 5-2D-F). Intracellular ROS levels decreased for all patient cells cultured on the copolymer, compared to TCPS control (Figure 5-2G).

5.3.3 Screening Cell-Cell and Cell-Matrix Proteins for Causative Agent

Since cell aggregation can be promoted by increased cell-cell interaction with altered cell-matrix interaction, it was imperative to screen major cell-cell/cell-matrix binding proteins thus far reported in order to glean what cell adhesion molecules might be altered in response to changing material parameters (Figure 5-3). Thus, cell-cell adhesion molecules were first investigated because of the aggregated status of hMSCs on 2 kDa PEG. Platelet endothelial cell adhesion molecule 1 (PECAM-1), connexin-43 (CX43), and intercellular adhesion molecule (ICAM) were significantly upregulated on all select copolymers relative to TCPS. However, expression of neural cadherin did not change. Five integrins had striking upregulation profiles that highlighted the effects of altered chemistry in the copolymers. Integrins alpha 1, 2 and 6 (ITGA1/ITGA2/ITGA6) had dramatically higher mRNA levels than TCPS. Interestingly, integrins beta 3 and 5 (ITGB3/ITGB5) had significant fold change.

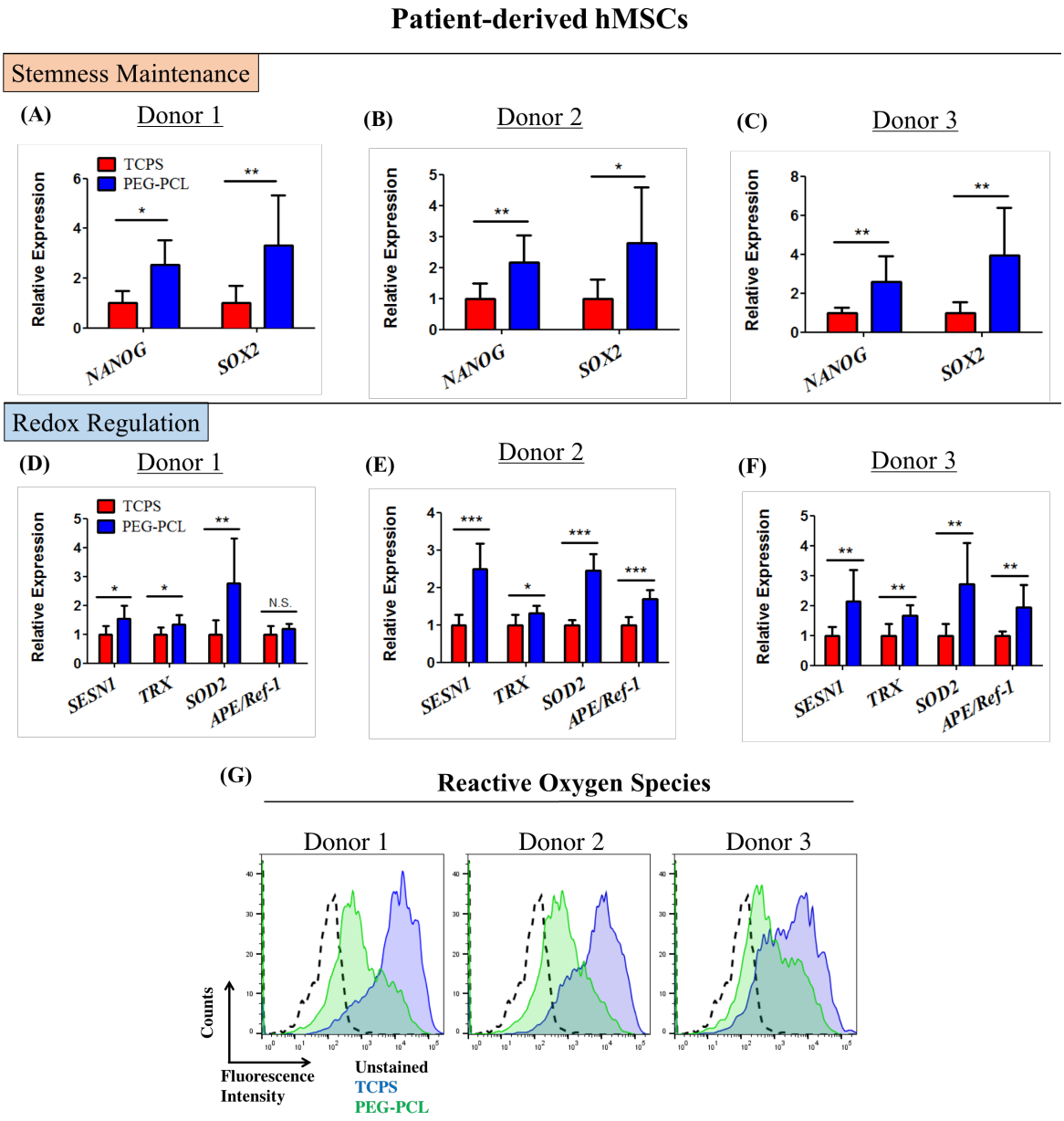

Figure 5-2 Patient-derived hMSCs Demonstrate that Material-mediated Modulation of Stemness and Redox is Not Donor-specific.
(A-C) hMSCs isolated from three different donors demonstrated significant increases in the expression of *NANOG* and *SOX2* when cultured on 5%PEG$_{2k}$, relative to TCPS control (n = 4). **(D-F)** Similarly, the expression of the anti-oxidative genes *SESN1, TRX, SOD2,* and *APE/Ref-1* was downregulated in virtually all cases (n ≥ 5). **(G)** Intracellular ROS load was also reduced for hMSCs isolated from all three donors when cultured on 5%PEG$_{2k}$, relative to the TCPS counterpart. All bars are mean ± S.D. *$p < 0.05$, **$p < 0.01$, ***$p < 0.001$ relative to TCPS or as indicated between the lines.

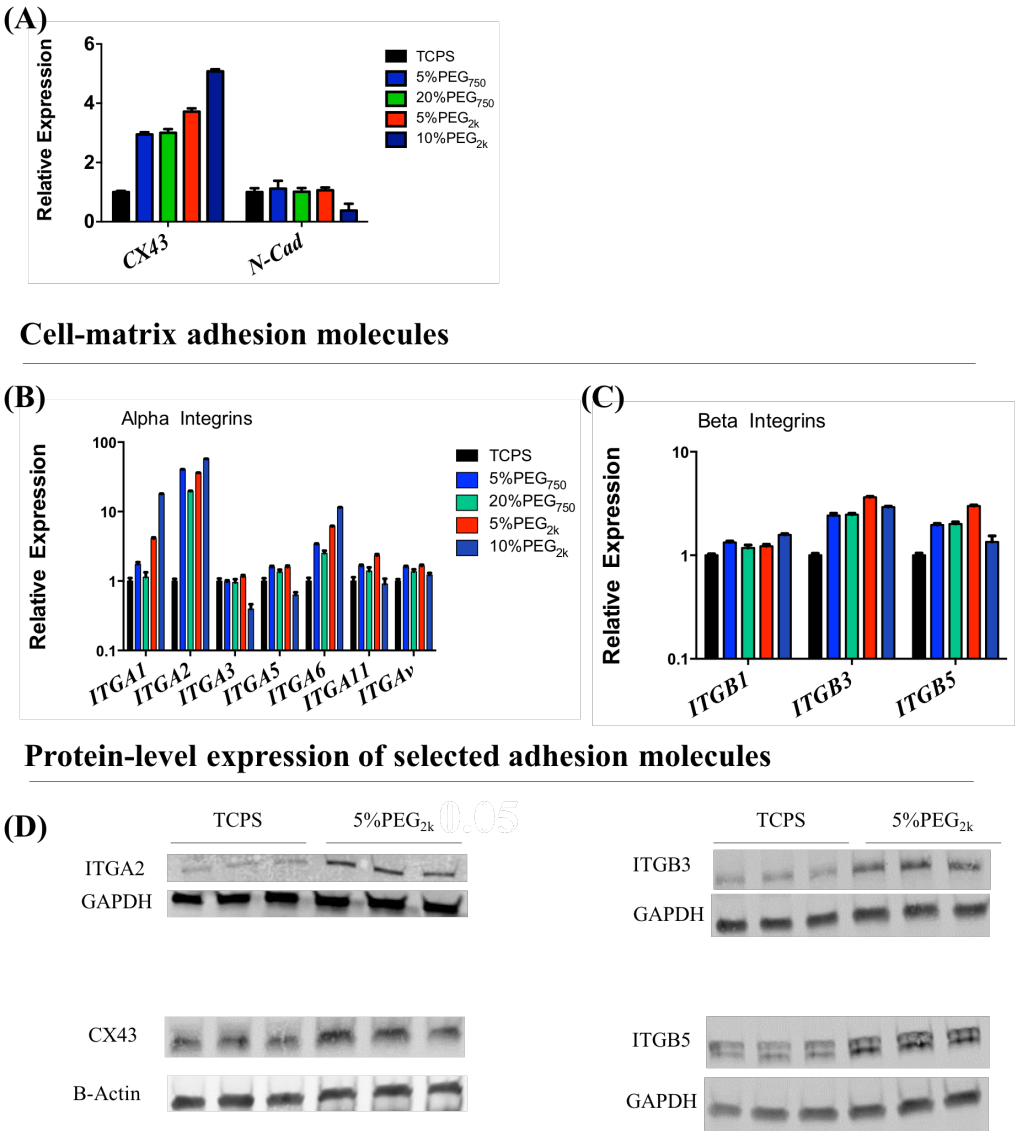

Figure 5-3 Gene- and Protein-level Screening of Cell Adhesion Molecules on Select Copolymers.

(A) Cell-cell adhesion molecule screen shows that Connexin-43 (CX43) is modulated by copolymer composition but N-cadherin (N-Cad) is not. **(B-C)** Screening of cell-matrix adhesion molecules (i.e. integrin: ITG) reveals a potential role for ITGA1, ITGA2, ITGA6, ITGB3, and ITGB5. We chose to inhibit ITGA2 and ITGB3/B5 as representative subunits of the heterodimeric integrin complex. **(D)** Protein-level analysis by Western blot confirms the upregulation of the molecules-of-interest (CX43, ITGA2, ITGB3, ITGB5) on 5%PEG$_{2k}$ copolymer, relative to TCPS (n = 3 independent replicates).

Principal component analysis (**PCA**) was performed to find correlations between hMSC responses and polymer properties (Figure 5-4). Expression of both stemness genes

was positively correlated with PEG molecular weight and mol% PEG. Several cell adhesion markers clustered in particular arrangements, as indicated by the dot and text color. The clear divergence among these clusters supports the hypothesis that polymer chemistry is a major factor that changes hMSC behavior. Moreover, the scale of screening such genes across a highly controlled set of copolymer surfaces allows for unprecedented insight into chemistry influences on particular cell adhesion molecules. Further inhibition experiments are required to verify mechanistic roles of the clustered cell-cell and cell-matrix markers on the functional and phenotypical changes of hMSCs.

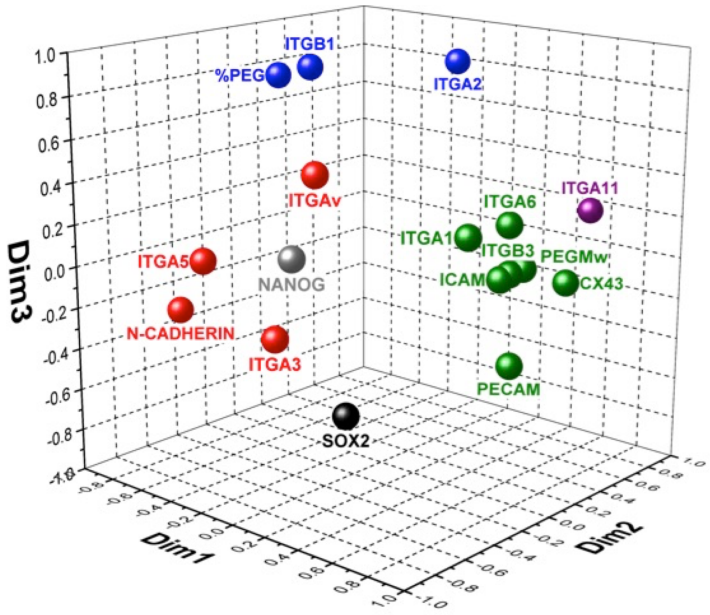

Figure 5-4 PCA for Stemness and Cell Adhesion Molecule Gene Expression Compared to PEG Chain Length and Mol%.
PCA illustrations color-coded correlations among different genes and altered chemical properties of the copolymers. PEG chain length (PEGMw here) was found to positively correlate with ITGA1/6, ITGB3, ICAM, PECAM and CX43. Mol% (%PEG here) positively correlated with ITGB1 and ITGA2.

5.3.4 Inhibition of Key Proteins to Elucidate Molecular Mechanism

Since the balance of cell-cell and cell-matrix adhesions is hypothesized to drive this effect, we measured the expression of multiple cell adhesion molecules and integrin

subtypes (Figure 5-3), and identified CX43, integrin α2 (ITGA2), and integrins β3/β5 (ITGB3/B5) as candidate regulators of the material-derived effect. Upon inhibition, we found that interruption of CX43 most potently attenuated the expression of stemness (Figure 5-5A) and anti-oxidative genes (Figure 5-5B). CX43 has recently been shown to maintain skin-derived stem cells[208], and is also required for resistance to oxidative stress in the bone marrow[209]; this finding indicates a functional role of CX43 in mediating material-derived signals in hMSCs.

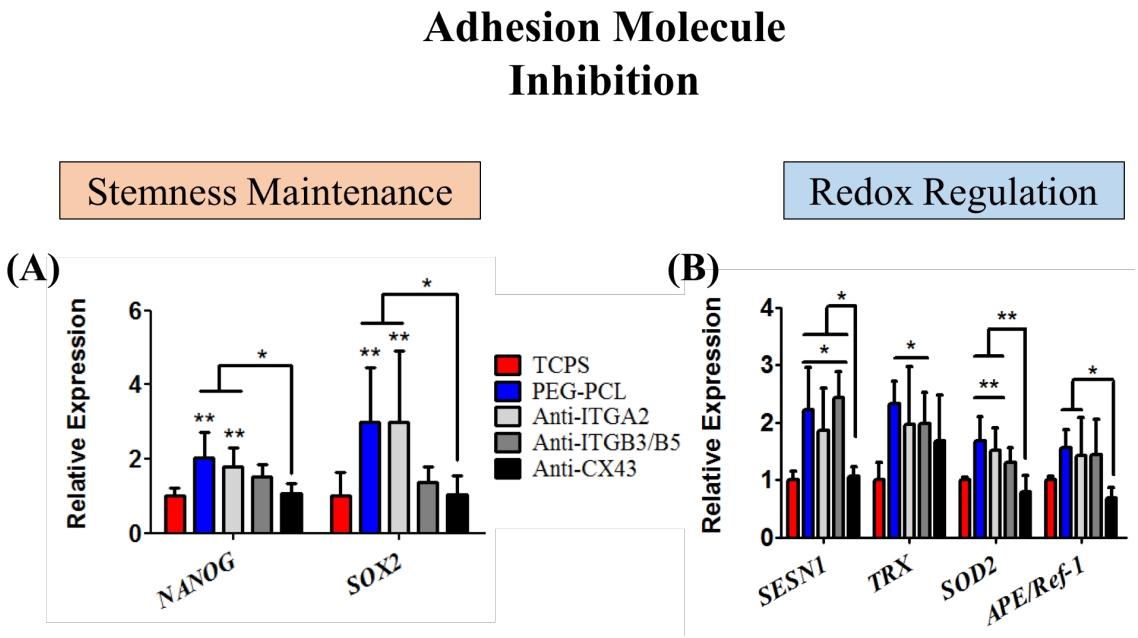

Figure 5-5 Functional Inhibition of Adhesion Molecules Suggests a Role for Connexin-43 in Regulating Outside-in Signaling.
(A) The gene expression of stemness markers significantly decreased when treated with anti-CX43 inhibitor, relative to untreated cells on 5%PEG_{2k}. **(B)** Similarly, the polymer-mediated increase in expression of *SESN1, SOD2*, and *APE/Ref-1* antioxidative genes was lost under treatment with anti-CX43 inhibitor ($n \geq 5$). All bars are mean ± S.D. *$p < 0.05$, **$p < 0.01$ relative to TCPS or as indicated between the lines.

5.4 Conclusions

In this Aim, donor hMSCs from a larger population were successfully harvested and screened to confirm a uniform population not contaminated by bone marrow fibroblasts or other native bone marrow cell types. Donor were selected with minimal screening criteria in order to maintain a more representative donor population that could potential use this copolymer platform for hMSC culture as well as determine if the effect of the copolymer effect on hMSC phenotype was universal beyond commercial hMSC cells sources. Upon culturing all three donors on a select copolymer ($5\%PEG_{2k}$), gene expression for both *NANOG* and *SOX2* were significantly increased to expression levels seen in the Lonza hMSCs. Moreover, the redox related genes were significantly upregulated with the concomitant decrease in ROS load.

Extensive PCR screening was conducted to determine what cell-cell and/or cell-matrix proteins could be positioned at the cell-material interface to initiate the drive for hMSC phenotype change. Several candidate genes were reported and upon western blot analysis, only ITGA2, ITGB3, ITGB5, and CX43 had increased translation. Chemical inhibition was employed as opposed to genetic modification or RNA interference given that hMSCs generally do not respond well to genetic-level manipulation and RNA interference would not only be transient but also risk upregulation of genes not present in non-treated cells. As such, CX43 inhibition was found to most ameliorate the phenotype change at the RNA level, thereby indicating that the forced aggregation affect driven by the PEG content is the likely dominant signaling factor for the increase in stemness in the hMSCs.

Chapter 6: Aim 4

6.1 Introduction

Human mesenchymal stem cells (hMSCs) offer a potential stem cell source for the translation of tissue engineering strategies to repair or replace damaged tissues. In fact, several proof-of-principle studies of direct stem cell injections into injury sites have resulted in improved function, such as in bone[210], cartilage[211], heart[212] and large blood vessels[213]. However, to effectively translate these studies to human clinical trials, sufficient stem cells need to be grown such that enough hMSCs are present at the injury/disease site to engraft and adopt the cell phenotype of the host tissue. Since hundreds of millions of hMSCs are required to generate meaningful regeneration of bone in large animals[67] for tissue generation, the few hundred thousand hMSCs that can be isolated from the bone marrow of any typical human donor requires expansion and breaks the Hayflick limit in the process. This could become an obstacle in front of translating hMSCs for therapeutic applications[42, 43, 68], as phenotype-level changes occur when hMSCs are serially passaged on tissue culture polystyrene (TCPS). In order to expedite clinical translation, new cheap, easily scalable strategies to maintain or reinstate hMSC fitness following expansion must be developed to counteract this inherent decline in cell health[68].

Spheroid aggregates of hMSCs produce the most effective stem cells in terms of stem cell potency and avoidance of senescence[78, 79]. Generating large quantities of aggregates have employed bioreactors and cell substrates with varying degrees of success. Maintaining bioreactor systems, due to their inherent design, can be financially prohibitive, and the complexity of interconnected bioreactor components and unique contamination risks (e.g. chemical or biological) complicates scaling up this process[214].

With respect to culture substrates, many groups have employed inverted hanging drop wells that have cell-repellant surfaces[79-82]. While the cell aggregates recapitulated the expected pro-stemness phenotype, controlling the size of the hMSC aggregates can be challenging and risk developing of necrotic cores that could result in negative consequences for the recipient tissues receiving the cells[74, 83, 84]. Moreover, the ability to handle and break down these aggregates into single cell suspensions for injection is difficult.

Approaches other than aggregates have also been developed for extensive culture of hMSCs. In one study by Ng *et al*, adipose MSCs were expanded *in vitro* by culturing on extracellular matrix (ECM) protein produced by fetal MSCs[215]. Although the adipose MSCs demonstrated increased functional capacity over several passages, concerns regarding immunogenicity arise when using ECM from another human donor that could stimulate a negative immune response by the stem cell recipient. Also, the financial burden of continually generating uniform fetal ECM and harvesting fetal MSCs to generate the ECM could become exponential. Alternatively, other groups like Duffy *et al* have developed synthetic polymer culture substrates that reduce harsh passaging techniques to grow hMSCs over many passages[216]. While their enzyme-free substrate did demonstrate marginal improvement in adipose MSC differentiation, the surface marker profiles were not maintained thereby challenging the efficacy of the system beyond simple differentiation assays and the monolayer appearance of the cells.

Using these studies as inspiration, we set out to demonstrate a cheap, easily-reproducible and effective culture platform that could maintain stem cell homeostasis and functional capacity over serial passaging. Based on previous work using a poly(ethylene

glycol) (PEG) and poly(ε-caprolactone) (PCL) copolymer film, we discovered that human bone marrow-derived MSCs maintained high stemness and low reactive oxygen species load compared to conventional TCPS plates (in review). Using the optimal copolymer composition from this study, we serially passaged patient donor hMSCs from aged donors (age > 65 years old) to demonstrate feasibility of maintaining a pro-stemness state of the cells as they multiplied by performing a series of functional assays including flow cytometry detection of reactive oxygen species (ROS), adipogenic and osteogenic differentiation and Raman spectroscopy for metabolite changes.

6.2 Methods

6.2.1 Polymer Substrate Preparation

5%PEG (Mw = 2000 Da) - 95%PCL (PEG-PCL) was synthesized using methods previously described[166]. Spin-coated polymer films were prepared with a commercial spin-coater (Laurell Technologies, North Wales, PA, USA). 15mm circular glass cover slips (Fisher Scientific) or CaF_2 discs (Crystran Ltd, Dorset, United Kingdom) were first cleaned with 100% ethanol (Sigma Aldrich), rinsed with dH_2O, and heated to 80°C for ~20 min to dry. A 1% weight/volume (w/v) solution of the copolymer in tetrahydrofuran (THF, Sigma Aldrich, St. Louis, MO, USA) was spun for 30 seconds at 3,000 RPM atop the clean glass cover slip (50 µl copolymer solution per sample). For preparation of "large-scale" Petri dish polymer films, Pyrex Petri dishes (Corning Inc., Corning, NY, USA) were cleaned as described above, and 1 mL of a 1% w/v solution of polymer in THF was spun for 2 min at 1,500 RPM to coat the surface. All samples were then exposed to constant vacuum for ≥30 min to remove excess solvent and kept in a

desiccator until use. Coverslips and dishes were UV sterilized for 60 min before use for cell culture.

6.2.2 Cell Culture

hMSCs were acquired from three patients at Vanderbilt University Medical Center in cooperation with Dr. Pampee P. Young, according to previously published methods[205]. All patients were male and over the age of 65 with no known blood disorders or cancer diagnosis at the time of bone marrow harvest. hMSCs were maintained in complete media (CM) composed of alpha-minimum essential media with nucleosides (αMEM, Life Technologies, Carlsbad, CA, USA) with 16.7% fetal bovine serum (Life Technologies), 1% penicillin/streptomycin (Life Technologies), and 4 μg/ml plasmocin (InvivoGen, San Diego, CA, USA). Cells were kept in a humidified incubator at 37°C and 5% CO_2, and media was replaced twice each week. For all experiments, hMSCs were seeded at a density of 10,000 viable cells/cm^2, as determined by exclusion of Trypan blue, and cultured for four days before passaging.

6.2.3 Immunocytochemistry

hMSCs were fixed with 4% paraformaldehyde (PFA, Sigma Aldrich) for 15 min, permeabilized with 0.3% Triton-X (Sigma Aldrich) for 15 min when probing intracellular targets, and blocked with 10% goat serum (Sigma Aldrich) for >2 hours, all at room temperature. Cells were incubated with Alexa488-phallodin (1:40 v/v in PBS, Life Technologies) for 10 minutes followed by counterstaining with Hoechst (Sigma Aldrich, 2 μg/ml) for 20 minutes at room temperature. Imaging was performed with a Zeiss LSM 710 confocal microscope (Carl Zeiss, Oberkochen, Germany), and images were processed with ImageJ (National Institutes of Health, Bethesda, MD, USA).

6.2.4 Measuring Levels of Intracellular Reactive Oxygen Species (ROS)

hMSCs were incubated with 10 μM 5-(and-6)-chloromethyl-2',7'-dichlorodihydrofluorescein diacetate acetyl ester (DCFDA) (Life Technologies) in serum-free DMEM for 30 minutes following the manufacturer's instructions. Cells were trypsinized and run on a BD LSR Fortessa (BD Biosciences, Franklin Lakes, NJ, USA) with the appropriate unstained control. N=3 biological replicates were conducted per substrate condition. Data were analyzed by FlowJo software (Tree Star Inc., Ashland, OR).

6.2.5 Differentiation Assays

hMSCs were grown on TCPS or PEG-PCL at their indicated passage for 4 days before being trypsinized and moved to 24-well TCPS plates. Differentiation assays were performed based on pre-established protocols[217, 218]. Adipogenic media using AMEM contained 16.7% FBS, 1% P/S, 4 μg/ml plasmocin, 0.1 μM dexamethasone, 0.45 mM 3-isobutyl-1-methylxantine, 0.2 mM indomethacin 1 μg/mL insulin and 1 μM rosiglitazone. Osteogenic media using AMEM contained 16.7% FBS, 1% P/S, 4 μg/ml plasmocin, 10nM dexamethasone, 5mM β-glycerophosphate and 50 μg/mL ascorbate-2-phosphate. All specialized differentiation media reagents were purchased from Sigma-Aldrich. Cells were cultured under induction media for one month and then fixed with 4% PFA. Cells were stained with Oil Red O (ORO) and Alizarin Red S (ARS) for adipogenic and osteogenic staining, respectively. Images were taken with a Nikon Ti inverted microscope (Nikon Instruments Inc., Melville, NY, USA) and processed with ImageJ. Stain quantification was performed on N = 3 independent experimental replicates. Images were first converted to RGB stack followed by setting a threshold range in the green

channel to account for variation in background light from brightfield imaging. The images were inverted resulting in a new grayscale image and mean intensity was measured.

6.2.6 Raman Instrumentation and Image Acquisition

Raman spectra of $N \geq 3$ cells per substrate condition (uncoated or PEG-PCL spin-coated CaF_2 discs at both passage 3 and passage 6) were recorded with an InVia confocal Raman microscope (Renishaw, Hoffman Estates, Illinois) using a diode laser at 532nm as excitation wavelength. The laser light was focused on the sample with a 100X/0.85 NA objective (Leica N Plan, Wetzlar, Germany) to deliver ~ 15 mW. Spectra were obtained with 10 second accumulations in mapping mode using a motorized xy-sample stage with 2 μm step-size through the same objective with a 180 degree backscatter collection geometry. Cosmic ray removal and noise smoothing based on a 4^{th} order Savitky-Golay filter were implemented in Matlab, along with background subtraction based on a modified polynomial fitting algorithm[219].

6.2.7 Statistical Analysis for ROS and Differentiation Assays

Comparisons between substrates for differentiation assays were performed with a Student's unpaired t-test. In all cases, $p < 0.05$ is considered statistically significant. Mean ± standard deviation is reported, unless otherwise noted.

6.2.8 Statistical Analysis for Raman Spectra

The intensity of the 1003 cm-1 peak (phenylalanine) was used to identify pixels within the Raman maps that correspond to hMSCs and generate an image mask. Spectra from identified pixels were included in analysis. Spectral regions that correspond to substrate-specific features were excluded from analysis of the dataset after masks were

generated for each cell area. Principal component analysis (PCA) was performed on full range Raman spectra following mean centering. Separate rank sum tests were applied to PCA scores to identify principal components that significantly differ between hMSC preparations (temporal passages or substrates). To identify biomolecules that correspond with individual PCs, wavenumbers associated with each biomolecule target were compiled into a library from prior literature with a focus on energy metabolism (refer to Tables 1 and S1). Raman shifts identified in the library that intersected with the substrate specific features were omitted from further analysis. Each remaining library Raman shift was compared to a threshold value defined as one standard deviation below the maximum intensity of the absolute value for each PC loading and the percent overlap for the library biomolecules and the PCs were determined. PCs that had significant overlap (>50%) with biomolecules and explained at least 0.5% of the total variance were compiled for further comparison.

6.3 Results

6.3.1 Experimental Design

The synthesis of the PEG-PCL polymer was based on ring opening polymerization of ε-caprolactone onto methoxy-PEG (Figure 6-1A). X and Y refer to the mole percent fraction of PEG and PCL, respectively. Based on prior work in our group, we utilized a 5%PEG-95%PCL copolymer where the PEG block was 2000 Da in size. Substrates were generated using a spin coater in order to create easily reproducible and high throughput films that cells could grow on (Figure 6-1B). As illustrated, a Pyrex© Petri dish (or coverslip) was placed in the spin coater with a small amount of copolymer

solution added in the center. The rotation of the block spread the solution evenly across the surface of the dish yielding the copolymer film in a culture-ready vessel.

For the longitudinal study, patient hMSCs were isolated from donors, expanded two passages on TCPS, and then subsequently cultured to passage 6 on either TCPS or PEG-PCL substrates (Figure 6-1C). Upon initial collection of bone marrow aspirate, the bone marrow was passed through a 70 μm filter, cultured on Histoplaque, and the monocytes were collected to be plated on TCPS. The hMSCs were the only cells to adhere to TCPS dishes at passage 0 and grown to confluence before being evaluated for appropriate positive and negative MSC markers at passage 1 (refer to Section 5.3.1). Cells were grown out to passage 2 and frozen down before beginning the serial passage phase of the experiment. As indicated in the Figure 6-1C, cells were passaged every 4 days, the time needed for hMSCs from all three donors to become confluent on TCPS. At day 4, cells from TCPS or PEG-PCL were re-plated onto new TCPS or PEG-PCL substrates. At passages 3 and 6, hMSCs were evaluated for functional capacity by looking at their morphology on their respective substrates, ROS load, osteogenic and adipogenic differentiation capacity, and metabolic profile visualized by confocal Raman spectroscopy.

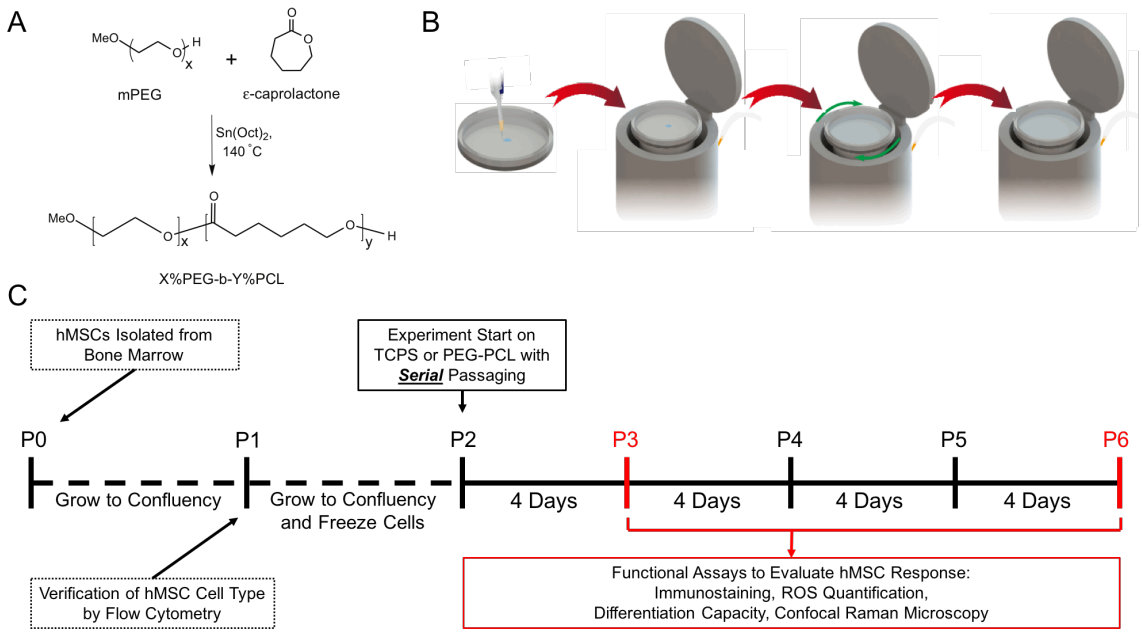

Figure 6-1 Experimental Flow Overview
(A) The PEG-PCL copolymer was synthesized using methoxy-PEG and ring-opening polymerization of ε–caprolactone. **(B)** Polymer films were generated by spin-coating copolymer solution onto coverslips or into Pyrex© petri dishes as shown in the illustration. First, a set volume of 1% w/v PEG-PCL solution is dropped onto coverglass or Pyrex© petri dishes. The coverglass or dishes are placed into the spin coater and an spin program (green arrows) is applied to the substrates. The PEG-PCL solution is evenly spread out on the surface with the solvent evaporating in the process. **(C)** The timeline of experiments with respect to passage number of the donor hMSCs. Red indicates that passage numbers where imaging or functional tests were performed.

6.3.2 Morphological Change of hMSCs on TCPS and PEG-PCL Over Passages

hMSCs from all donors showed markedly altered cellular morphology when passaged on TCPS or PEG-PCL (Figure 6-2). At passage 3, hMSCs grown on TCPS had a flattened, spread cell shape typical of this cell type. However, when cultured on PEG-PCL, distinct cell clusters, reminiscent of hanging drop aggregates, formed over the entire surface area of the coverslips. Cells within the aggregates were round in morphology with some cells exhibiting spindle-like extensions. At passage 6, TCPS hMSCs were highly aligned with strong spindle morphology, forming a cell sheet. PEG-PCL hMSCs yielded aggregates with increased size and number of constituent cells. The

diversity in spheroid morphology can be seen among the donors, where donor 2 maintained a tight, enlarged spheroid of cells, donor 1 had more cellular spindle projections anchoring to the copolymer surface, and donor 3 contained a spheroid with a broad based of spindle-shaped hMSCs along the copolymer surface like a cell-feeder layer. Of note, passage 6 was not exceeded in this study due to the spheroids becoming so large that they no longer adhered to the surface of the PEG-PCL.

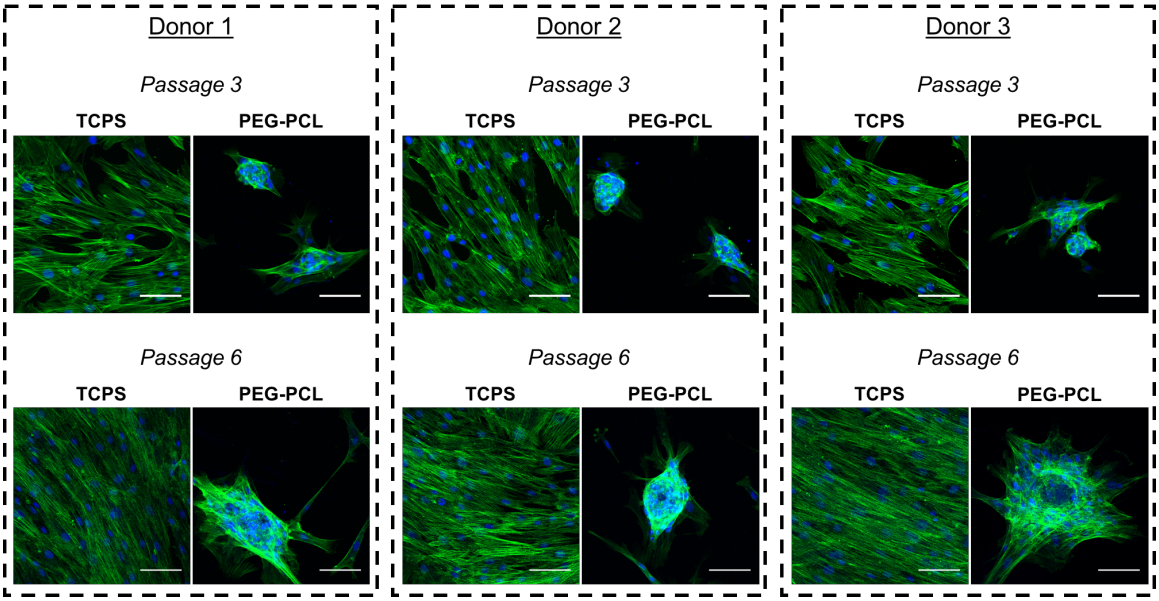

Figure 6-2 Morphological Changes Occur Over Serially Passaging hMSCs on Their Respective Substrates.
Cells were stained with AlexaFluor-488-conjugated phalloidin (green) and Hoechst nuclear counterstain (blue). Scale bar = 100μm.

6.3.3 ROS Load

All donors displayed decrease levels of detected intracellular ROS when grown on the PEG-PCL compared to TCPS (Figure 6-3). Passage 3 fluorescent signal was decreased by ~1 order of magnitude, and this effect was maintained at passage 6. TCPS curves (blue) had a homogenous population while PEG-PCL (green) was more heterogenous as seen by the increased peak width. This could be due to the cells closer to

the material interface containing more ROS compared to the cells within in the cell aggregate.

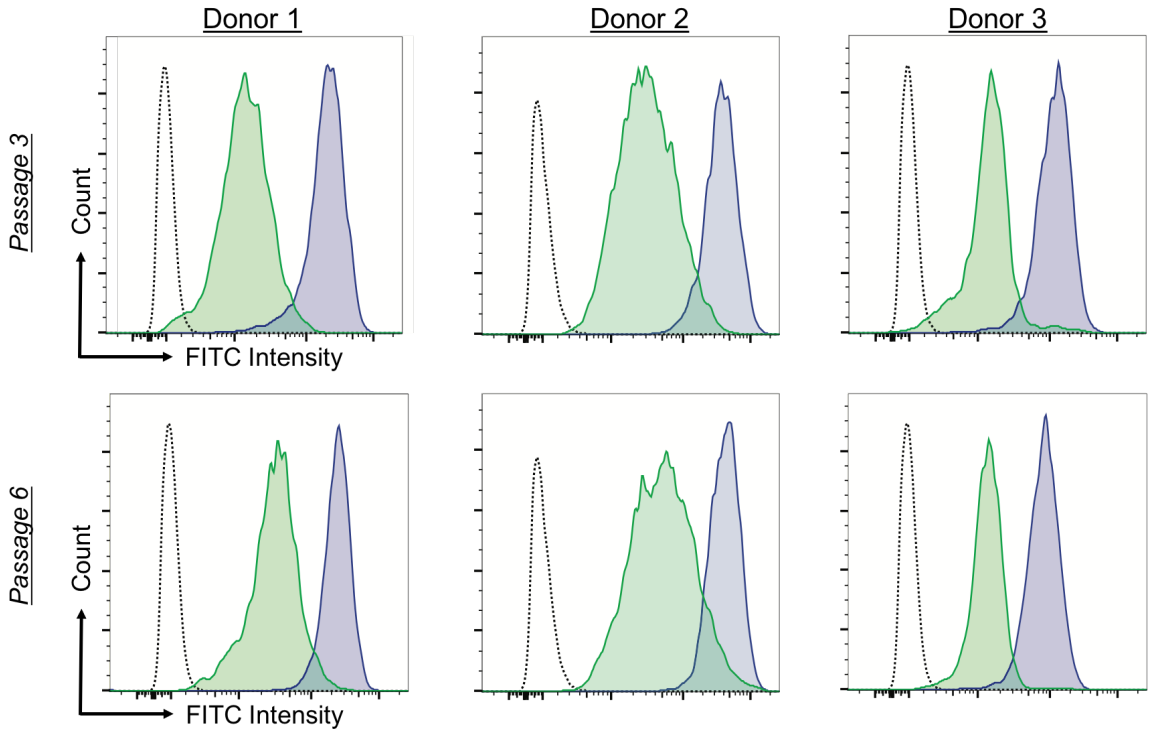

Figure 6-3 PEG-PCL Copolymers Reduce Intracellular ROS Load for Donor Cells at Both Passages.
hMSCs were incubated with DCFDA and FITC intensity correlated with active ROS species. The graphs shown are representative results from N = 3 independent experimental replicates.

6.3.4 Differentiation Capacity

The degree of osteogenic differentiation, as evaluated by image-based quantification of ARS, was maintained when hMSCs were serially passaged on PEG-PCL (Figure 6-4). Different staining patterns were observed across all donors at passage 3, with enhanced mineralization for donor 2. However, at passage 6, staining intensity was markedly decreased on TCPS, with minimal staining for donor 2. Adipogenic differentiation had mixed results across all donors (Figure 6-5). Staining patterns for TCPS and PEG-PCL did not show unique patterning or oil droplet shape nor where there

statistically significant differences in staining intensity between the substrates at either passage.

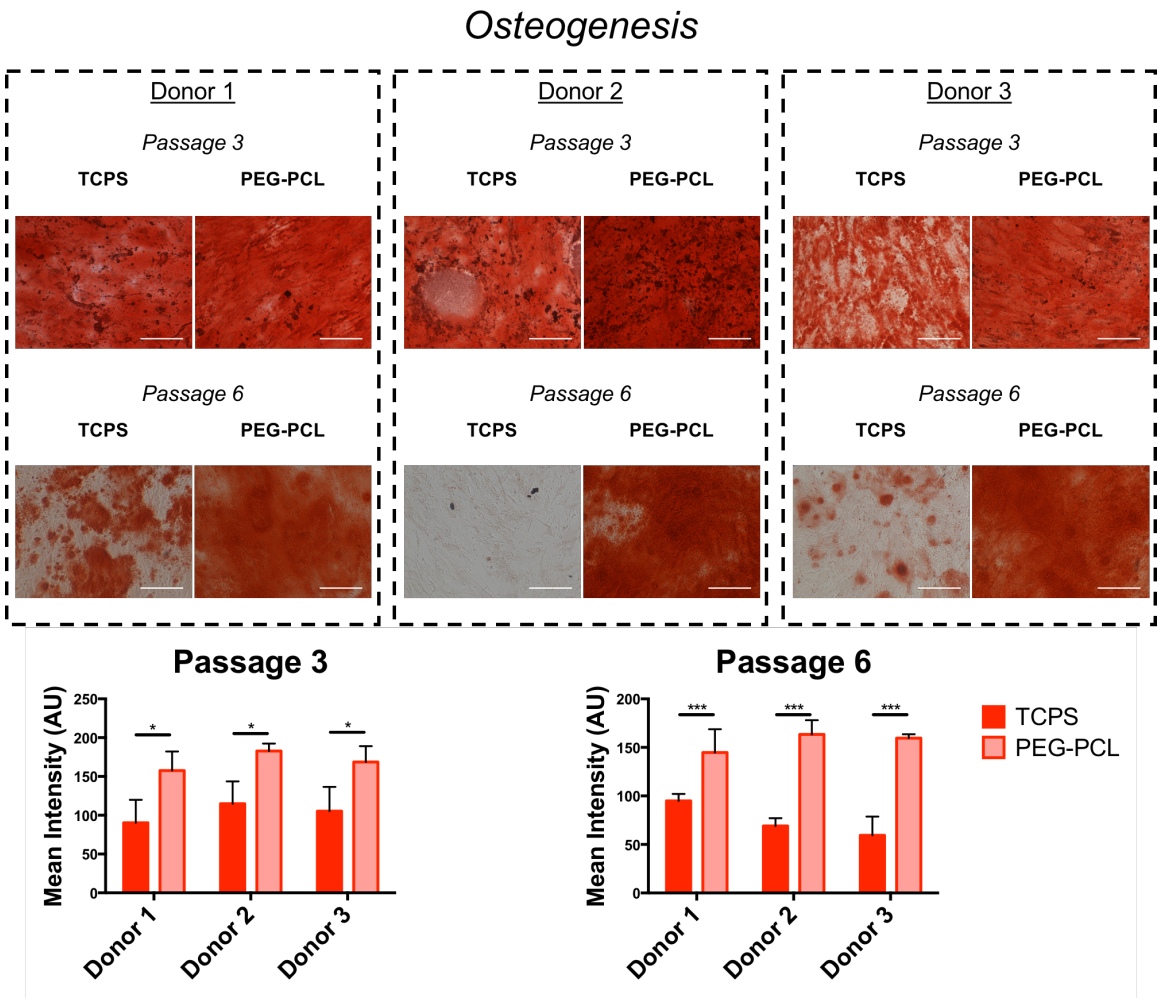

Figure 6-4 Osteogenic Differentiation of hMSCs.
hMSCs were stained with Alizarin Red after one month of osteogenic differentiation. Mean ± S.D. of stain intensity is plotted for all donors for each substrate with N = 3 independent experimental replicates. * $p < 0.05$, *** $p < 0.001$.

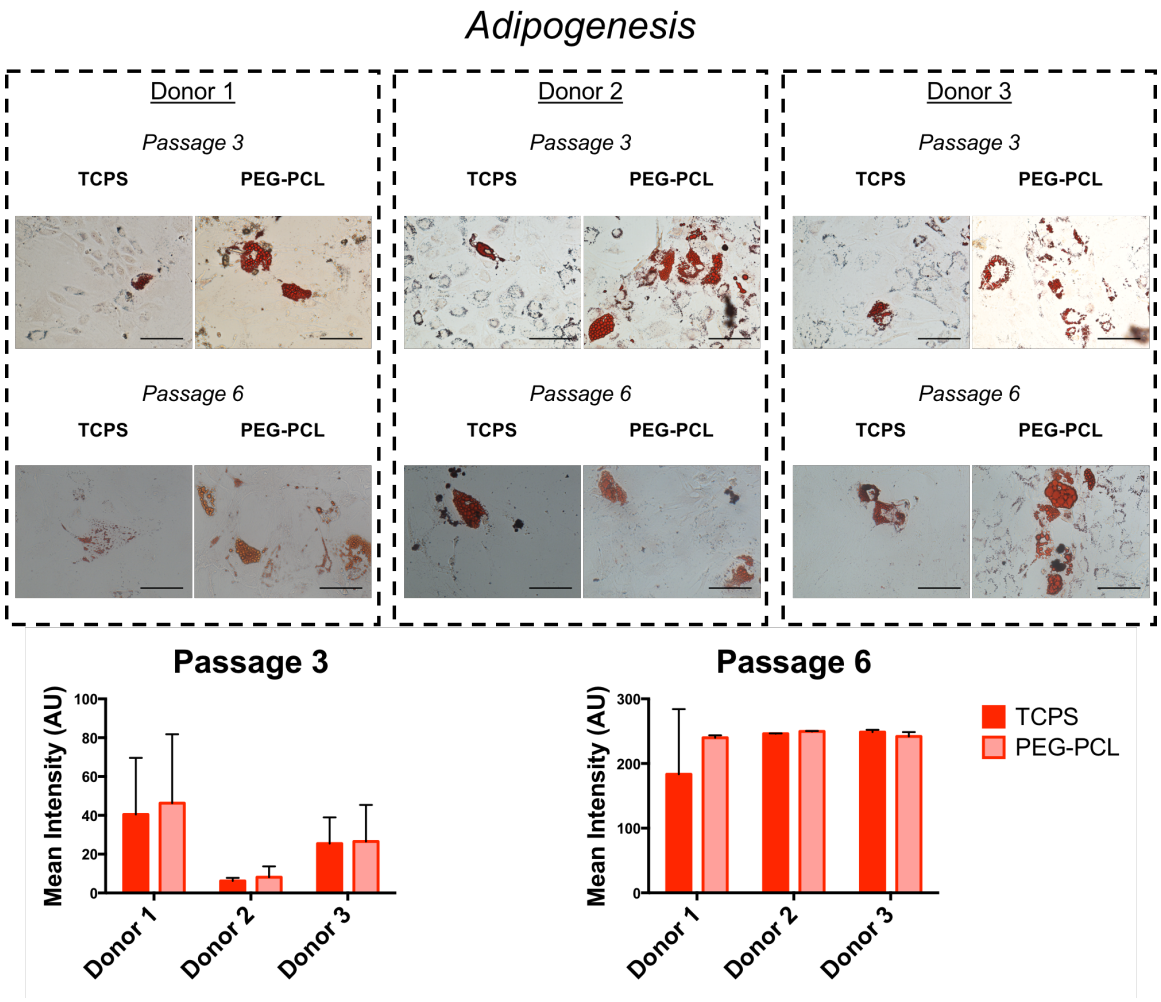

Figure 6-5 Adipogenic Differentiation of hMSCs.
hMSCs were stained with Oil Red O after one month of adipogenic differentiation. Mean ± S.D. of stain intensity is plotted for all donors for each substrate with N = 3 independent experimental replicates.

6.3.5 Raman Analysis

hMSCs grown on TCPS and PEG-PCL were imaged with confocal Raman microscopy in a 2 micron grid. Mask generation to isolate the cell area and not background-only area used the intensity of the 1003cm^{-1} peak as the delineating feature, as a strong cellular signal of this peak did not occur in the background specific spectra of either TCPS or PEG-PCL substrates (Figure 6-6). Furthermore, masking of acquired maps was necessary to remove signals specific to the substrates themselves within the cell area spectra.

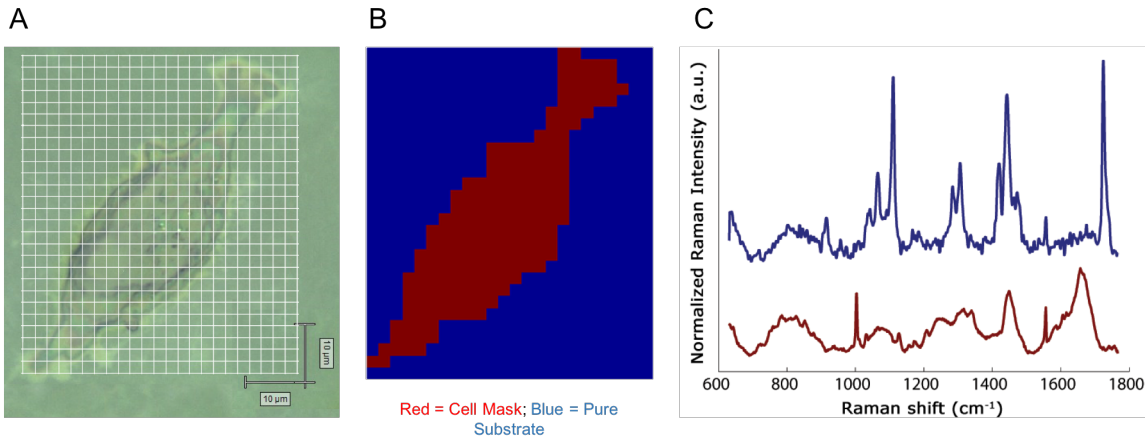

Figure 6-6 Raman Analysis Overview.
(A) Brightfield images of the cells were overlaid with a grid indicating the step pattern taken for each of the images taken by the confocal Raman microscope. **(B)** Using the cell-less background substrate as a control signal, all pixels within the grid that did not contain cell signal was thresholded to generate a cell mask for spectral analysis. **(C)** An example graph illustrating the cell-less background signal (blue) and the cell-containing spectra (red). Cell-containing spectra were used for subsequent metabolite analysis.

Two types of analysis were conducted on the collected Raman spectra. The first test investigated if the composite signal from the whole cell differed with respect to passage change with substrate control (referred to as 'temporal') or signals from the whole cell differed with respect to substrate at the same passage number (referred to as 'substrate') (Figure 6-7). Based on non-parametric tests, significant differences were

found between both temporal passage and substrate for several principal components of the aggregate signal.

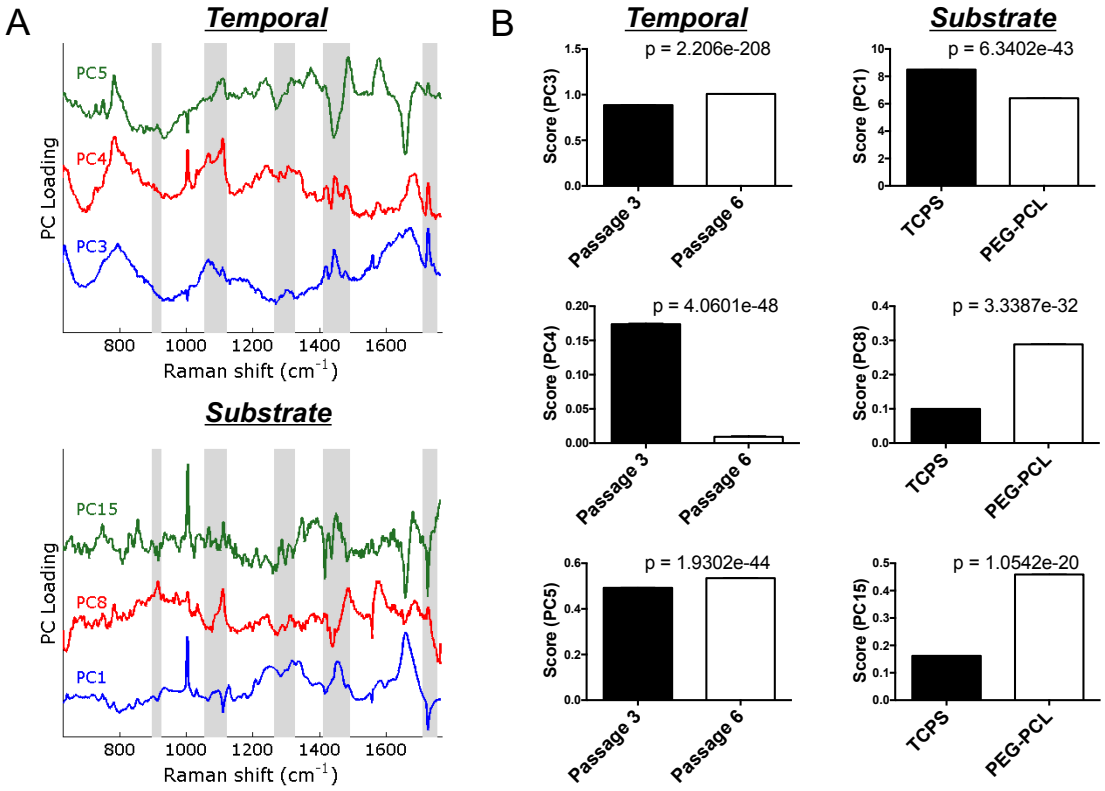

Figure 6-7 Whole Spectra Principal Component Comparison.
(A) Principal component loadings for PCs that most significantly differed between temporal passage (PCs 3, 4, & 5) and substrate (PCs 1, 8, & 15) indicate Raman spectral features that are strongly represented in the data. The vertical gray bands indicate spectral regions that correspond to strong features from the substrate material. **(B)** The top three most significant principal component scores for temporal (differences between passage number on constant substrate, left column) and substrate (differences between TCPS and PEG-PCL at given passage number, right column) based on a rank sum test. All principal components explain greater than 5% of the total variance in the data set. Mean ± SEM is plotted with calculated p-value.

The second analysis of the Raman spectra investigated if certain metabolites within the cells were changing. Several metabolites were selected and inputted into a biomolecules library. The library comparison results are presented in Tables 1 & S1. For each biomolecule, a ratio the mean PC scores are presented for hMSCs at a given passage number on PEG-PCL versus TCPS (Table 1). Biomolecules that show increased score ratios are indicated in red while those that decreased are in green. With respect to temporal change on a given substrate, nearly 50% of the metabolites did not significantly change over serial passage. However, when passage number was held constant and TCPS and PEG-PCL were compared, both upregulation and downregulation of metabolites were found across the entire biomolecule library. To start, the overwhelming majority of fatty acids, triglycerols, cholesterol & cholesterol esters, and membrane lipids were in higher quantity for PEG-PCL compared to TCPS. On the other hand, slightly less than half of the amino acids decreased in relative amount while slightly more than half increased. Interestingly, DNA nucleotides adenine and guanine increased while cytosine and thymine decreased. Finally, metabolites associated with glycolysis and pentose phosphate pathway (e.g. GSSG, lactic acid) were increased with compensatory decrease in TCA cycle/oxidation associated pathways (e.g. pyruvate and Acetyl-CoA).

Table 6-1 Fold-change in Metabolite Signal Intensity with Respect to Fixed Substrate.
Red is upregulated and green is downregulated.

Biomolecule	PEG-PCL / TCPS at P3	PEG-PCL / TCPS at P6	P-value	Reference
Acetyl CoA	4.344	1.996	1.1E-03	[220]
Adenine	1.433	3.288	6.2E-17	[220]
Ammonia dimer	0.114	0.787	2.6E-03	[221]
Ammonia-water complex	0.113	0.778	1.1E-03	[221]
Coenzyme A	1.433	3.288	6.2E-17	[220]
Cytosine	1.688	0.096	4.9E-06	[220]
Glycine	1.688	0.096	4.9E-06	[220]
Reduced Glutathoine (GSH) (solid)	1.688	0.096	4.9E-06	[222]
Oxidized Glutathione (GSSG) (solid)	0.106	0.720	4.9E-06	[222]
Guanine	0.145	0.883	2.8E-12	[220]
Lactic Acid	1.433	3.288	6.2E-17	[223]
L-Glutamine	1.688	0.096	4.9E-06	[224]
Pyruvate	1.688	0.096	4.9E-06	[220]
Ribose (solid)	1.433	3.288	6.2E-17	[225]
Ribose-5P	1.688	0.096	4.9E-06	[225]
Thymine	1.688	0.096	4.9E-06	[220]
Uracil	1.688	0.096	4.9E-06	[220]
Amino Acids				
Alanine	0.530	14.793	5.9E-19	[226]
Arginine	0.530	14.793	5.9E-19	[226]
Aspartic Acid	1.688	0.096	4.9E-06	[226]
Cysteine	17.788	0.013	6.7E-10	[227]
Glutamic Acid	0.530	14.793	5.9E-19	[226]
Glycine	8.804	4.941	1.7E-02	[226]
Histidine	0.124	0.835	6.7E-10	[226]
Isoleucine	1.688	0.096	4.9E-06	[226]
Leucine	1.672	1.469	2.8E-12	[226]

Lysine	1.433	3.288	6.2E-17	[226]
Methionine	1.433	3.288	6.2E-17	[226]
Phenylalanine	5.596	0.638	4.9E-02	[226]
Proline	1.433	3.288	6.2E-17	[226]
Serine	1.688	0.096	4.9E-06	[226]
Threonine	4.051	10.896	8.2E-03	[226]
Tryptophan	1.672	1.469	2.8E-12	[226]
Tyrosine	0.162	0.787	6.7E-10	[226]
Valine	1.433	3.288	6.2E-17	[226]
Fatty Acids				
Arachidic Acid	1.433	3.288	6.2E-17	[228]
Arachidonic Acid	1.688	0.096	4.9E-06	[228]
Elaidic Acid	4.344	1.996	1.1E-03	[228]
Linoleic Acid	0.126	0.566	4.9E-06	[228]
Myristic Acid	1.433	3.288	6.2E-17	[228]
Oleic Acid	0.133	0.571	1.7E-02	[228]
Palmitic Acid	1.433	3.288	6.2E-17	[228]
Palmitoleic Acid	0.131	0.581	8.2E-03	[228]
Stearic Acid	0.170	0.937	4.4E-02	[228]
α -Linolenic Acid	0.530	14.793	5.9E-19	[228]
Triglycerols				
Tri-11-eicosenoin	0.119	0.796	4.9E-06	[228]
Triarachidin	6.471	4.523	3.3E-02	[228]
Tribehenin	6.471	4.523	3.3E-02	[228]
Tricaprin	4.379	0.260	1.9E-02	[228]
Trielaidin	4.051	10.896	8.2E-03	[228]
Trierucin	0.120	0.802	8.2E-03	[228]
Trilaurin	4.379	0.260	1.9E-02	[228]
Trilinolein	0.100	0.701	1.1E-03	[228]
Trilinolenin	0.530	14.793	5.9E-19	[228]
Trimyristin	0.122	0.827	3.2E-02	[228]
Triolein	0.530	14.793	5.9E-19	[228]
Tripalmitin	0.167	0.838	5.3E-03	[228]

Tripalmitolein	0.530	14.793	5.9E-19	[228]
Triparoin	0.114	1.046	1.8E-02	[228]
Tripetroselinin	0.104	0.703	4.9E-06	[228]
Tristearin	0.167	0.838	5.3E-03	[228]
Trucaprylin	0.112	1.038	2.6E-02	[228]
Cholesterol & Cholesterol esters				
Cholesterol	1.433	3.288	6.2E-17	[228]
Cholesteryl linoleate	0.104	0.703	4.9E-06	[228]
Cholesteryl oleate	0.104	0.703	4.9E-06	[228]
Cholesteryl stearate	1.433	3.288	6.2E-17	[228]
Choleteryl palmitate	1.433	3.288	6.2E-17	[228]
Membrane Lipids				
L- α -Phosphatidylcholine	4.344	1.996	1.1E-03	[228]
L-α-Phosphatidylethanolamine	0.167	0.869	1.1E-03	[228]
Sphingomyelin	4.344	1.996	1.1E-03	[228]

6.4 Discussion

Longitudinal, serial passage of hMSCs for regenerative medicine and tissue engineering-based therapies is undoubtedly a prerequisite critical to clinical success. Regardless of allogenic or autologous donor cells, ensuring a sizable stem cell mass is prepared for host injection enables the greatest chance for engraftment. However, in the process of expanding said stem cells, phenotype characteristics associated with senescence could inhibit success rates of future stem cell therapies and potentially raise the risk of harming patients. Therefore, different culture strategies ranging from pro-aggregate culture vessels to minimally-disrupted monolayer substrates have been explored for culturing hMSCs *ex vivo*[79-82, 214]. We sought to do the same but used aged human donor hMSCs and evaluated phenotype retention via functional assays.

Prior work in our lab discovered that carefully tuning of PEG-PCL copolymer composition manipulated the stemness homeostasis of hMSCs (in review). Similar to the aforementioned study, cells on the copolymer were into a forced aggregation state, but as the passage number increased, the size of these aggregates also increased (Figure 6-2). These formations with a small interfacing cell layer with the material like as a 'feeder layer' has been seen *in vivo* in the bone marrow[229-231]. Additionally, speculation of hMSCs being related to pericytes, which is still under debate in the field, demonstrates the same balance of cell-cell (pericyte-endothelial cell) and cell-matrix interaction (pericyte-surrounding ECM), and the PEG-PCL appears to cause the hMSCs to behave as if they were in a bone marrow or capillary-like environment[113].

Because the functional capacity of hMSCs have direct effects on their clinical usefulness, the first functional test was evaluated the ROS load in the hMSCs. It is well known that general cell health decreases as ROS increases in the cell as the likelihood of cancerous or apoptotic-inducing changes occurring[232]. ROS loads for hMSCs cultured on TCPS for both passages were higher than those cultured on PEG-PCL (Figure 6-3). This aligns with previous literature reporting stem cell niches or the small fractions of stem cells that replenish the stem cell population have naturally low amounts of ROS. This is also logical given that ROS can also damage DNA, which if damaged beyond repair halts replacement of damaged resident cells of a tissue or organ. Because hMSCs cultured on PEG-PCL maintained a similar level of ROS through passage 6, our substrate appears to keep these hMSCs in a pro-stem cell state and correlates with the growing size of the aggregates (Figure 6-2).

hMSCs used for future tissue engineering therapies will likely be differentiated into other cell types for healing damaged tissues. Hence, differentiation assays were conducted for osteogenesis and adipogenesis (Figure 6-4 and Figure 6-5). In the original publication defining the bone marrow stromal population, researchers confirmed that the stromal cells were multipotent and able to differentiate into multiple mesenchymal stem types include bone, cartilage and fat[1]. hMSCs have also been differentiated into neurons[233] and cardiac cells[234], but for this study osteogenesis and adipogenesis were employed in order to compared to the literature. Osteogenic potential was maintained for hMSCs cultured on PEG-PCL while the ability for successful mineralization was abrogated by passage 6 for TCPS. Loss of osteogenic potential is known to occur due to senescence-associated changes[235-237], thus validating that the pro-stemness phenotype was maintained on PEG-PCL. However, no significant changes were seen in. This was likely due to age of the donors and resulted in reduced differentiation capacity[58]. Moreover, hMSC bone marrow-marrow derived might not readily differentiate into adipocytes compared to adipose-derived MSCs.

The final functional characterization of the cells was the use of Raman spectroscopy to observe changes in metabolite signatures. Raman spectroscopy has long been used to validate the quality of inorganic materials but also over the recent decades characterize fixed and live tissues including, but no limited to, how bone mineralization occurs among different cell types[238] and how engineering substrate platforms can alter bone regeneration[239]. Therefore, we interrogated the cells with Raman spectroscopy to measure biomolecule changes. To the best of our knowledge, this has been the first Raman profile of serially passaged hMSCs to-date.

Mentioned in Section 3.5, nearly 50% of the biomolecule library did not report significant changes when compared temporally (Table C-1). We reason that inherent changes in protein expression on a substrate are primed to a particular cell state, as was seen in the ROS data where both TCPS and PEG-PCL ROS loads were relatively unchanged between passage 3 and 6. If biomolecule changes were compared between substrates at a fixed passage, the ratio of a known ROS sink, GSSG, increased at passage 6, indicating a compensation mechanism was in place to keep the ROS in PEG-PCL low or unchanged relative to TCPS. Conversely, GSH follows the opposite trend, suggesting that changes of this cell metabolite at low passage were not needed prior to the senescence-associated passage 6.

Raman data also supported previous literature suggesting that stem cells primarily utilize glycolysis and non-oxidative mechanisms to generate cellular energy. Lactic acid and Coenzyme A (coupled with low Acetyl-CoA) were markedly increased by passage 6 on PEG-PCL relative to TCPS, representing a shift to glycolysis and less TCA cycle, while ribose-5-P likely decreased due to highly activated pentose phosphate shunt pathway. The increase of ribose in PEG-PCL is intriguing given that previous literature has shown hMSCs upregulate RNA expression and requires additional ribose for post-translational modifications[140, 240]. We cannot make any conjectures on the changes in amino acid levels other than reporting their shifts given the lack of hMSC-specific literature on amino acid metabolism.

Finally, an increase in most all of the fat-based metabolites was observed PEG-PCL hMSCs. Breakdown of these biomolecules requires beta-oxidation, and it has been reported that hMSC stem cell properties are lost when fatty acids are increasingly used as

energy sources[241]. Some fatty acids, like myristic acid, have anti-apoptotic activities in hMSC populations and was significantly increased on PEG-PCL hMSCs[242]. Overall, the overwhelming trend of increased fat-based biomolecule composition in PEG-PCL hMSCs reinforces glycolysis-based shift in metabolism.

6.5 Conclusion

In this study, we explored the ramifications of serially passaging human bone marrow-derived hMSCs from aged patient donors on a novel PEG-PCL copolymer film to maintain functional capacity and stem cell phenotype for future tissue engineering applications. hMSCs grown on the films illustrated morphologies representative of hMSCs found *in vivo* and maintained low ROS loads that if unchecked are known to be associated with the progression of senescence-associated changes. Moreover, the maintenance of differentiation capacity of PEG-PCL hMSCs demonstrated relevance of using our alternative copolymer film to maintain stem cell functionality for downstream hMSC adoption of target tissue cell types. Finally, first-of-its-kind Raman analysis of hMSC biomolecule profile illustrated the metabolic snapshot of PEG-PCL hMSCs maintaining metabolic fluxes representative of stem cell homeostasis relative to TCPS.

Chapter 7: Summary and Future Directions

7.1 Summary

Discovery and development of biomaterials that maintain the stemness phenotype of stem cells remains an underdeveloped sub-field of research. Because of the anticipated future demand for regenerative medicine therapies that rely on autologous or allogenic stem cells to create tissue or organ replacements, the ability for clinicians to safely and effectively culture said stem cells *ex vivo* without modification of phenotype is paramount. Therefore, the purpose of this dissertation was to address this unmet need as it pertained to hMSCs through the careful synthesis and investigation of PEG-PCL copolymers and the subsequent hMSC response to *in vitro* culture on these materials.

In Aim 1, experiments utilizing the first copolymer library containing PEG, PCL and cPCL demonstrated that PEG content prevented protein adsorption and stiffened the gels due to its known crystallinity. cPCL was proven to be a rescue subunit that counteracted the PEG but maintained hydrophilic properties similar to PEG. Culturing hMSCs on the library illustrated that a PEG-PCL copolymers yielded spheroid-like morphologies of the cells while cPCL and PCL-only controls had cell morphologies similar to TCPS controls. Intracellular ROS correlated with the morphology findings where PEG-PCL substrates had lower ROS and TCPS and cPCL-containing copolymers had higher ROS loads. Expression of stemness genes *NANOG* and *SOX2* peaked on 10%PEG-90%PCL, and surprisingly the *in vivo* marker of bone marrow hMSCs, STRO-1, was reactivated on this polymer and not present on TCPS, as expected. Pre-coating of the 10%PEG-90%PCL substrate with different ECM molecules confirmed that the surface chemistry was the primary driver of the hMSC response, as even the smallest of

pre-coat ECM mass abrogated the increase in stemness gene upregulation. Finally, when the PEG-PCL copolymer library was expanded based on mol% and PEG molecular weight, it was reported that very high molecular weight PEG (5000 Da) prevented cell attachment, very low molecular weight PEG (750 Da) allowed maximal cell attachment, and an intermediate molecular weight PEG (2000 Da) allowed cell attachment provided that the mol% did not exceed 10%PEG. Isolated four copolymer compositions to decouple the mol% and PEG molecular weight effects, hMSCs cultured on all substrates had increased stemness gene and redox gene expression coupled with decreased ROS load and proliferation rates, all of which are indicative of stem cell homeostasis.

In Aim 2, nanoscale characterization of the copolymer surface was studied to determine how the chemical features of the copolymers were organizing themselves, and if the responsive cell machinery that adheres to the copolymers organized in a similar manner. Because of the resolution and feasibility challenges of other imaging and analytical techniques (e.g. atomic force microscopy and confocal fluorescent microscopy), the ability to visualize the potential phase separation between PEG and PCL domains are severely hindered. However, other high-energy physics tools, like x-ray and neutron beam scattering, have the sufficient prerequisites to decipher the domain separation with reasonably applicable computational analysis. As such, the entire PEG-PCL copolymer library that formed the basis of the second half of Aim 1 was subjected to x-ray scattering and scattering patterns for small-, medium- and wide-angle spectra were collected. PCL lamella were found to increase as the PEG molecular weight increased, and was not responsive to PEG mol%. The degree of phase separation was stronger for PEG_{2k} and PEG_{5k} compared to PEG_{750}, and was further confirmed by the correlative

increase in PCL crystallinity. To our surprise, the PEG_{750} interdigitated with amorphous PCL, which explained why the lamellar spacing was less than 100%PCL controls and the PCL crystallinity being unchanged between dry and wet states. This implied that the large PEG chains were swelling and therefore both covering the remaining amorphous PCL that cells could adhere to and push apart the PCL crystalline domains coupled with increased degree of PCL crystallinity. Verification that the hMSCs were in fact able to interpret phase separation of this resolution was conducted using super resolution microscopy. Mature focal adhesion marker paxillin was stained and both number and morphology of focal adhesions were significantly altered for PEG_{2k} copolymers compared to Glass, 100%PCL and PEG_{750} groups. This served as evidence that the phase separation event that occurs in substrate formation and further enhanced in wetting was indeed sensed by the relevant hMSC cell attachment machinery that primarily interacts with the copolymer surface.

In Aim 3, patient-derived hMSCs from Vanderbilt University Medical Center were harvested in order to test if the an optimal PEG-PCL copolymer ($5\%PEG_{2k}$) elicited the same phenotype response from a less restricted donor population compared to Lonza hMSCs, which have strict donor criteria and not representative of the potential broader patient population that would utilize regenerative medicine hMSC-based therapies. hMSCs from three male donors over 65 years old were successfully isolated, purified and expanded for future cell experiments. None of the donors has known genetic blood disorders nor had known cancer diagnoses at the time of bone marrow harvest. When each of the donors was cultured on $5\%PEG_{2k}$, *NANOG* and *SOX2*, along with the previously tested redox genes, were significantly upregulated. Additionally, ROS load

was decreased on the copolymer substrate compared to tissue culture plate for all donor lines. Therefore, it could be concluded that 5%PEG_{2k}, and by extension the PEG-PCL library itself, exuded a universal effect on hMSCs that was not donor specific. Following up this finding, qPCR screening of cell-cell and cell-matrix genes was conducted, followed by western blotting significant hits, in order to determine what proteins may be causatively changing hMSC phenotype at the early stages of cell-material interface. Of the four candidate proteins (ITGA2, ITGB3, ITGB5, and CX43), only chemical inhibition of CX43 resulted in abrogating the observed gene upregulation coupled with similar cell morphology to that of TCPS. This implied that the forced cell aggregation driven by steric hindrance of the PEG likely initiated the phenotype response by the hMSCs to reflect cell properties indicative of hMSCs found in their native bone marrow niche.

In Aim 4, hMSCs were serially passaged on either TCPS or 5%PEG_{2k} to see if this new substrate platform could feasibly maintain the hMSC stemness phenotype over multiple passages. As has been reported for TCPS surfaces, serial passaging of hMSCs results in senescence-associated qualities that hinder the regenerative potency of hMSCs. Thus, provided the findings of the first three aims, the optimal PEG-PCL copolymer would mitigate this acquisition of senescence-associated qualities over several passages. Using functional assays as the majority of readouts, all three donor lines responded in similar manners. Cell morphologies were similar to those found in Aim 1 and ROS loads were also decreased and stayed decreased at both passages 3 and 6. When induced to differentiate into either adipocytes or osteocytes, a divergent response was observed. For adipogenesis, little significant differences in degree of differentiation were reported,

which was likely due to the fact these hMSCs were obtained from bone marrow and preferably form bone tissue. The finding was also speculated to be due to the fact the donors had aged cells as donors were 65 years or older. In contrast, for osteogenesis, the degree of mineralization was significantly increased and maintained through passage 6 from hMSCs grown on 5%PEG_{2k}. Finally, the metabolic profiles of the hMSCs were evaluated using confocal Raman spectroscopy demonstrating the substrate type heavily influenced hMSC health towards glycolysis/low ROS (pro-stemness) over several passages likely due to the spheroid-promoting abilities of PEG-PCL.

7.2 Future Work

7.2.1 Parallel Sequencing

The gene screening that was conducted for this dissertation was limited with respect to breadth and depth of genes in human genome. While it is obvious that a majority of genes in the human genome will contain relevant and/or critical roles in the physiology being studied with respect to hMSCs on these copolymers, there are likely many signaling pathways, both chemical and mechanical, being triggered or suppressed. RNAseq and mass spectroscopy would appear relevant for the future of this work that similar methods are employed across the copolymer library to better address 1) what is changing, and 2) what is the causative mechanism triggered inside hMSCs once exposed to the copolymer substrates. Additional inhibition experiments could follow the sequencing experiment to further verify targets of importance to maintaining the stem cell phenotype.

7.2.2 Variation in Copolymer Subunits

A second area of further study involved changing the PEG and PCL subunits. Although PCL is a special polymer with unique semi-crystalline properties, swapping out PEG and PCL with similar polymers and adjusting the molecular weight and mol% could provide insight into global biomaterial design. The interfaces that are created with different copolymer subunits could produce data that indicate different physicochemical variables alter hMSC phenotype despite the copolymer library being synthesized in the same manner as the PEG-PCL library (i.e. only adjusting molecular weight and mol%). Subunits that are replaced need not only be synthetic polymer because natural polymers, many of which can be constituents in ECM, could be experimented with.

The shape of the copolymer subunits can also be adjusted given that linear block copolymers were utilized. PEG can take many formats beyond the linear format. Multiarm PEG is readily available and additional terminal functional groups can be added to the arms. Furthermore, the PCL component could be replaced with multiarm components or ring shapes, which alter phase separation.

7.2.3 Additional X-ray and Neutron Scattering

SAXS, MAXS and WAXS are not the only means to obtain nanoscale structural features of the copolymer films. Two different sets of experiments could be carried out to better inform what the material surface looks like. In the first experiment, small-, medium- and wide-angle neutron scattering could elucidate the PEG domain shapes and provide specific swelling volumes that were only speculated on from the x-ray scattering experiments in Aim 2. This could be done by soaking the copolymer films in deuterated water and use similar analytical methods for x-ray scattering. The second experiment

takes both x-ray and neutron scattering, but instead of the incident beam being perpendicular to the film surface, a grazing incident beam can be directed across the surface area of the film and provide a two-dimensional image of the phase separated features. Grazing incident methods are both more precise and more accurate than the x-ray scattering performed in Aim 2, however the preparation and execution of this alternative method is often difficult.

7.2.4 Other Classes of Stem Cells for Culture

The remaining unanswered question based on this dissertation work is investigating if other types of stem cells could benefit from culture on the PEG-PCL substrate. Many stem cells in the past required special suspension bioreactors or feeder cells in order to maintain stem cell homeostasis, but newer biochemical supplements and protocols have steered the stem cell field away from the antiquated techniques. It would be fascinating if these substrates contributed towards the same goal with difficult stem cells such as induced pluripotent stem cells, embryonic stem cells, intestinal stem cells, and hematopoietic stem cells, to name a few. If these copolymers could maintain these stem cell cultures and with less biochemical supplement burden, the cost of developing stem cell lines for regenerative medicine may drastically decrease.

Appendix A: Antibody and Primer Tables

A.1 Antibody Table

Table A-1:Antibody Table with Dilutions

			Dilution Factors	
Target	**Host**	**Company**	**IF, FCM**	**WB**
STRO-1	Mouse	Santa Cruz Biotech	1:50	N/A
Paxillin	Mouse	BD Transduction Laboratories	1:200	N/A
Integrin-α2	Rabbit	Santa Cruz Biotech	N/A	1:200
Integrin-β3	Rabbit	Cell Signalling Technologies	N/A	1:200
Integrin-β5	Rabbit	Cell Signalling Technologies	N/A	1:200
Connexin-43	Rabbit	Cell Signalling Technologies	N/A	1:200
GAPDH	Rabbit	Cell Signalling Technologies	N/A	1:5000
β-Actin	Rabbit	Santa Cruz Biotech	N/A	1:2000

A.2 Primer Table

Table A-2: Primer Table

Gene	Accession Number	Forward Primer (5' – 3')	Reverse Primer (3' – 5')	Amplicon (bp)
SOX2	NM_003106.3	ATCAGGAGTTGTCAAGGCAGAG	CGCCGCCGATGATTGTTATT	172
Nanog	NM_024865.2	AATACCTCAGCCTCCAGCAGATG	TGCGTCACACCATTGCTATTCTTC	148
SESN1	NM_001199933	CGACCAGGACGAGGAACTT	CCAATGTAGTGACGATAATGTAGG	273
SOD2	NM_000636	GCTGACGGCTGCATCTGTT	CCTGATTTGGACAAGCAGCAA	101
TRX	NM_003329	TGAAGCAGATCGAGAGCAAGAC	TTCATTAATGGTGGCTTCAAGC	305
APE/REF-1	NM_001641	GCAGATACGGGGTTGCTCTT	TTTTACCGCGTTGCCCTACT	136
CX43	NM_000165.3	TCATTAGGGGGAAGGCGTGA	GGGCACCACTCTTTTGCTTAAA	164
ICAM-1	NM_000201.2	TGTGACCAGCCCAAGTTGTT	TGGAGTCCAGTACACGGTGA	186
N-Cadherin	NM_001792	CGAGCCGCCTGCGCTGCCAC	CGCTGCTCTCCGCTCCCCGC	199
ITGA1	NM_181501.1	ACGCTGCTGCGTATCATTCA	CACCTCTCCCAACTGGACAC	194
ITGA2	NM_002203.3.	TTAGCGCTCAGTCAAGGCAT	CGGTTCTCAGGAAAGCCACT	179
ITGA3	NM_002204.2	GCTGACCGACGACTACTGAG	CTGGTCACCCAGTGCTTCTT	178
ITGA5	NM_002205.2	AGACTTCTTTGGCTCTGCCC	CGCTCCTCTGGGTTGAACAT	174
ITGA6	NM_001079818.1	TCATGGATCTGCAAATGGAA	AGGGAACCAACAGCAACATC	135
ITGA11	NM_001004439	GCCTACTGAAGCTGAGGGAC	TGTGATTCAGCTGTGGAGCA	129
ITGAv	NM_002210.4	TCCGATTCCAAACTGGGAGC	AAGGCCACTGAAGATGGAGC	137
ITGB1	NM_002211.3	GCGCGGAAAAGATGAATTTACAAC	ATCTGGAGGGCAACCCTTCT	245
ITGB3	NM_000212.2	ACCAGTAACCTGCGGATTGG	TCCGTGACACACTCTGCTTC	208
ITGB5	NM_002213.3	TACCTGGAACAACGGTGGAG	GCTTCGGGCCTCCAATGATA	242
GAPDH	NM_002046.4	GCACCGTCAAGGCTGAGAAC	TGGTGAAGACGCCAGTGGA	138

Appendix B: LC/MS Data

B.1 Connexin-43 Inhibitor Peptide (GAP26) Validation by LC/MS

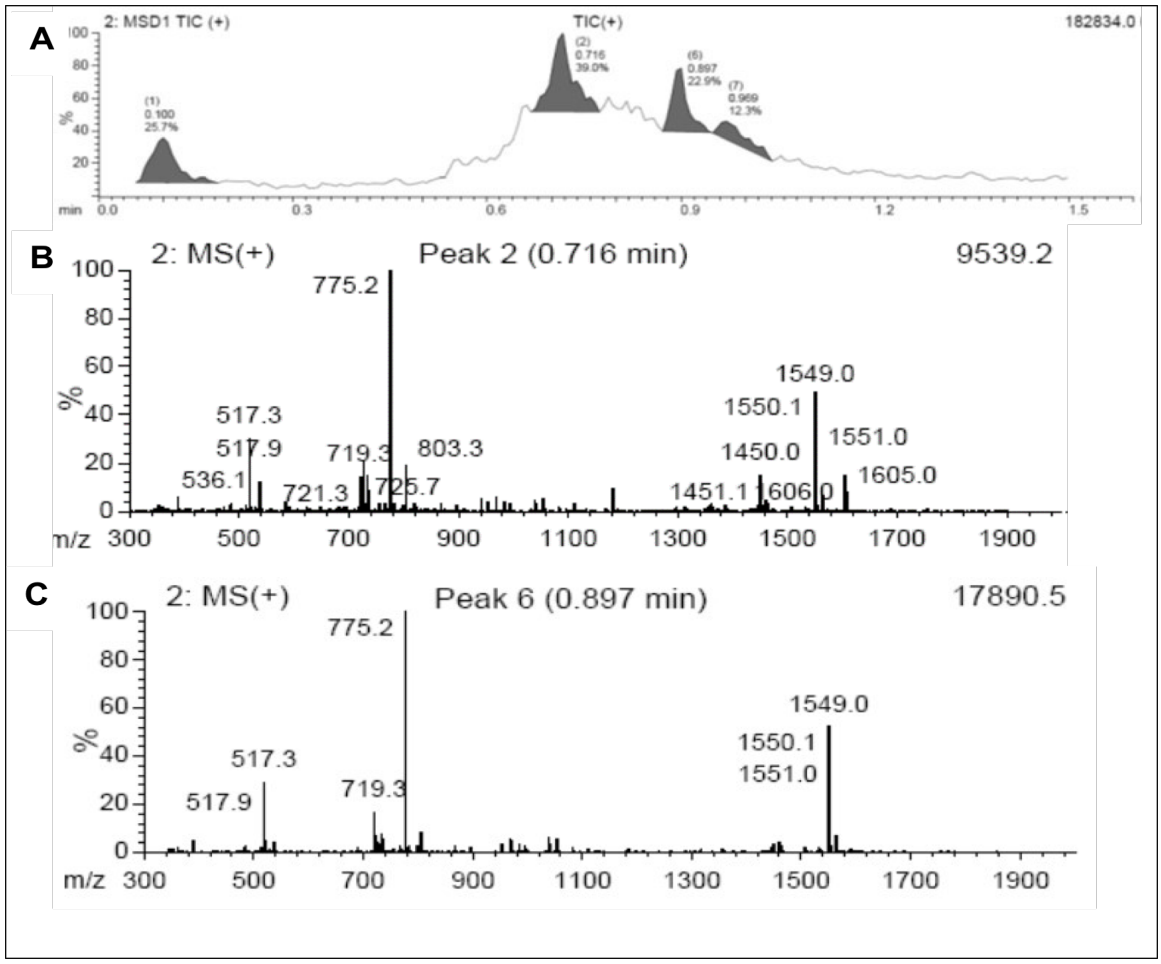

Figure B-1 LC/MS of Connexin-43 Inhibitor Gap26.
LC-MS spectra of Gap26 (Val-Cys-Tyr-Asp-Lys-Ser-Phe-Pro-Ile-Ser-His-Val-Arg) peptide (A) Total ion current (TIC) spectrum of Gap26 peptide, (B, C) Mass spectrum of peptide ion at 0.716 (B), and 0.897 (C) retention time indicate characteristic mass peak of peptide at m/z 1550, the expected molecular weight of Gap26.

Appendix C: Temporal Raman Spectra Data

C.1 Raman Table at Fixed Passage

Table C-1 Fold-change in Metabolite Signal Intensity with Respect to Fixed Passage Number.
Red is upregulated and green is downregulated.

Biomolecule	P6 / P3 on TCPS	P6 / P3 on PEG-PCL	P-value	Reference
Coenzyme A	1.377	3.158	6.24E-17	[220]
Cytosine	2.219	0.126	4.94E-06	[220]
Guanine	1.377	3.158	6.24E-17	[220]
Lactic Acid	1.377	3.158	6.24E-17	[223]
Ribose (solid)	1.377	3.158	6.24E-17	[225]
Ribose-5P	2.219	0.126	4.94E-06	[225]
Thymine	2.219	0.126	4.94E-06	[220]
Amino Acids				
Alanine	0.111	3.104	5.91E-19	[226]
Aspartic Acid	2.219	0.126	4.94E-06	[226]
Cysteine	0.350	0.000	6.67E-10	[227]
Glutaminc Acid	0.111	3.104	5.91E-19	[226]
Isoleucine	2.219	0.126	4.94E-06	[226]
Leucine	2.219	0.126	4.94E-06	[226]
Lysine	1.377	3.158	6.24E-17	[226]
Proline	1.377	3.158	6.24E-17	[226]
Serine	2.219	0.126	4.94E-06	[226]
Valine	1.377	3.158	6.24E-17	[226]
Fatty Acids				
Arachidic Acid	1.377	3.158	6.24E-17	[228]
Arachidonic Acid	2.219	0.126	4.94E-06	[228]
Myristic Acid	1.377	3.158	6.24E-17	[228]
Oleic Acid	0.111	3.104	5.91E-19	[220]
Palmitic Acid	1.377	3.158	6.24E-17	[228]
Stearic Acid	1.377	3.158	6.24E-17	[220]
α-Linolenic Acid	0.111	3.104	5.91E-19	[228]

Triglycerols				
Trilinolein	0.525	3.556	4.94E-06	[228]
Trilinolenin	0.111	3.104	5.91E-19	[228]
Trucaprylin	0.111	3.104	5.91E-19	[228]
Cholesterol & Cholesterol esters				
Cholesterol	1.377	3.158	6.24E-17	[228]
Cholesteryl linoleate	0.525	3.556	4.94E-06	[228]
Cholesteryl oleate	0.525	3.556	4.94E-06	[228]
Membrane lipids				
L- α -Phosphatidylethanolamine	1.377	3.158	6.24E-17	[228]

Appendix D: Copolymer-Mediated Cell Aggregation Promotes a Pro-angiogenic Stem Cell Phenotype *In Vitro* and *In Vivo*

D.1 Introduction

Human bone marrow-derived mesenchymal stem cells (hMSCs) have become immensely popular for tissue engineering and regenerative therapies over the past two decades. hMSCs have been used not only to generate new bone[210] or cartilage[211] to replace degenerate tissues, they have also been injected into damaged heart[212] or peripheral arteries[213], which are highly vascularized. Choosing hMSCs to regenerate tissues that require significant vasculature is based on the fact that hMSCs are pro-angiogenic, likely due to their perivascular localization within the physiological niche[113], and can both stimulate and stabilize the formation of vasculature over long periods of time[122]. Furthermore, hMSCs have moved rapidly into clinical trials for modulation of the immune system in graft-versus-host disease[243, 244] due to their immunomodulatory capabilities. To reach relevant numbers for clinical therapy, hMSCs must undergo serial *in vitro* expansion on tissue culture polystyrene (TCPS) plates, which alters their transcriptional profile similar to natural aging[42, 43]. Application of biomaterial systems that impart therapeutically-beneficial properties to hMSCs during this expansion phase would prime cells prior to *in vivo* implantation. Therefore, identifying a material type that regulates the pro-angiogenic and anti-inflammatory capabilities of hMSCs would enhance successful outcomes of hMSC-derived therapies.

Previous work has demonstrated that forced aggregation of hMSCs, also known as "hanging drops" (HDs), stimulates a drastic increase in both their anti-inflammatory [79, 245-247] and pro-angiogenic [248] expression profiles. A range of techniques have been leveraged to enhance and exploit these characteristics for both *in vitro* and *in vivo*

applications[249], and encapsulation of hMSC HDs for therapeutic delivery has become an area of recent interest[250]. Similarly, a series of papers has investigated chitosan-based substrates that promote hMSC aggregation, demonstrating that gene regulation and differentiation capacity are affected by the semi-repellent surfaces[75, 251, 252]. To date these studies have not addressed the therapeutic capacity of hMSC HDs although a pro-angiogenic, anti-inflammatory cellular system would have excellent clinical benefit. Since the anti-inflammatory profile of HDs is clearly established, and inflammation and angiogenesis are intrinsically linked processes[253], we hypothesized that synthetic copolymers of moderate surface repellency could promote the HD-like aggregation of hMSCs, and that this would correlate with a pro-angiogenic, anti-inflammatory phenotype. Here, we demonstrate that formation of hMSC clusters on copolymers that contain competing cell-repellant and cell-adhesive units results in a functional pro-angiogenic phenotype both *in vitro* and *in vivo.* These findings provide new insight into material-mediated control of the therapeutic capacity of adult-derived stem cells and can be used for improving the design of cell-instructive scaffolds for tissue engineering and regenerative medicine.

D.2 Methods

D.2.1 Substrate Preparation

Copolymers were synthesized by methods previously described, and compositions were verified by ^{1}H NMR. The specific compositions of PEG in each copolymer was 5.6% (5%PEG750), 20.6% (20%PEG750), 5.5% (5%PEG2k), and 9.3% (10%PEG2k); percentages were rounded to 5/10/20% for simplicity of presentation and discussion. For two-dimensional cell culture experiments, glass cover slips (15 mm diameter, Fisher

Scientific, Waltham, MA, USA) were cleaned with 100% ethanol (Sigma Aldrich, St. Louis, MO, USA), rinsed with dH_2O, and heated to 80°C for 20 min to dry. A 1% weight/volume copolymer solution in tetrahydrofuran (THF, Sigma Aldrich) was spun for 30 seconds at 3,000 RPM. Excess solvent was then removed from samples by exposure to a constant cold-trap vacuum for ≥ 30 min. Samples were UV sterilized for 30-60 min on each side before use and secured with an autoclaved silicon O-ring (McMaster Carr, Atlanta, GA, USA) during cell culture experiments.

D.2.2 Cell Culture

hMSCs were purchased from Lonza (Walkersville, MD, USA), maintained in complete media (CM) composed of alpha-minimum essential media with nucleosides (αMEM, Life Technologies, Carlsbad, CA, USA) with 16.7% fetal bovine serum (Life Technologies), 1% penicillin/streptomycin (Life Technologies), and 4 μg/ml plasmocin (InvivoGen, San Diego, CA, USA). Cells were kept in a humidified incubator at 37°C and 5% CO_2, and media was replaced twice each week. When ~80% confluent, hMSCs were detached with 0.05% trypsin-EDTA, re-seeded at a density of 100 - 500 cell/cm^2, and cultured for 7-14 days before reaching confluence. For all experiments, hMSCs (page < 6) were seeded at a density of 10,000 viable cells/cm^2, as determined by exclusion of Trypan blue, and cultured for three to four days.

D.2.3 Immunocytochemistry and Scanning Electron Microscopy

hMSCs were fixed with 4% paraformaldehyde (PFA, Sigma Aldrich) for 15 min, permeabilized with 0.3% Triton-X (Sigma Aldrich) for 15 min, and blocked with 10% goat serum (Sigma Aldrich) for >2 hours, all at room temperature. hMSCs were then incubated with Alexa488-phallodin (1:40 v/v in PBS, Life Technologies) for 10 minutes

followed by counterstaining with Hoechst (Sigma Aldrich, 2 μg/ml) for 20 minutes at room temperature. Imaging was performed with either a Nikon Ti inverted microscope (Nikon Instruments Inc., Melville, NY, USA) or a Zeiss LSM 710 confocal microscope (Carl Zeiss, Oberkochen, Germany), and images were processed with ImageJ (National Institutes of Health, Bethesda, MD, USA).

For SEM, hMSCs were fixed and then dehydrated with a series of graded ethanol washes (25%, 50%, 60%, 70%, 80%, 90%, 95%, 100% x 3; 10 minutes each) before being stored in a desiccator overnight. Samples were then sputter coated with gold (Cressington Scientific, Watford, United Kingdom) and imaged under SEM (Hitachi S-4200, Tokyo, Japan) at an accelerating voltage of 1-10 kV.

D.2.4 Quantitative Real-Time Polymerase Chain Reaction

hMSCs on spin-coated substrates were homogenized with the Trizol reagent (Life Technologies), mixed with chloroform (1:5 Trizol:chloroform), and separated by centrifugation (12,000x g, 15 min, 4°C). The RNA contained within the aqueous phase was then isolated with RNeasy columns (Bio-Rad, Hercules, CA, USA), according to the manufacturer's instructions. cDNA was synthesized using a kit (Applied Biosystems, Life Technologies), and qRT-PCR was performed with a SYBR Green master mix (Bio-Rad) with 15 - 20ng cDNA and 500nM each of forward and reverse primers, using a CFX Real-Time PCR System (Bio-Rad). The qRT-PCR protocol included: 95°C for 3 min, followed by 40 cycles of denaturation at 95°C for 30 sec, annealing at 58°C 30 sec, and extension at 72°C for 30 sec. For cPCR, products were separated on a 2% agarose gel containing ethidium bromide for 15 minutes at 100V, and bands were visualized with a gel imaging station. For qRT-PCR, the expression of each gene of interest was

normalized to expression of glyceraldehyde 3-phosphate dehydrogenase (GAPDH) as a housekeeping gene, generating the $\Delta C(t)$ value, and expression of $2^{-\Delta\Delta C(t)}$ relative to the TCPS control with $n \geq 3$ biological replicates for each experiment is reported. Primer sequences are listed in Table D-1 and only those that showed single, specific amplicons were used for qRT-PCR experiments.

D.2.5 *In Vivo* Experiments

Three-dimensional scaffolds of either 100%PCL or 10%PEG-90%PCL were cut into 6 mm discs, sterilized by UV exposure for 1 hour on each side, placed into 96-well plates, and held in place with silicon O-rings. The bottom of the 96-well plates was first coated with 1% agarose to prevent cell attachment, following previously published protocols [71]. hMSCs were seeded at a density of 10^5 cells / scaffold (or left in culture media for "blank" scaffolds) and cultured for one week in complete media before subcutaneous implantation into the ventral region of athymic, NU/J Foxn1$^{nu/nu}$ male nude mice (6-8 weeks of age, n = 7 animals, The Jackson Laboratory, Bar Harbor, ME, USA). Four types of scaffolds were used for this experiment: 100%PCL without cells ("blank"), 100%PCL seeded with hMSCs, 10%PEG-90%PCL without cells ("blank"), and 10%PEG-90%PCL seeded with hMSCs. One of each scaffold type was implanted into the same animal, totaling four scaffolds per animal into eight animals. Four of the eight animals were used for fluorescence microangiography to visualize functional vasculature, as previously described [253]. Scaffolds were then excised and fixed in 4% PFA overnight at 4 °C before being subjected to graded soaks in optimal cutting temperature compound (OCT, Tissue-Tek) with sucrose and snap-frozen in OCT. Samples were cryosectioned to 5 μm-sections, and stained with goat anti-mouse CD31 antibody (sc-1505, Santa Cruz

Biotechnology) and IRdye 680 tagged anti-goat secondary antibody (926-68024, Li-Cor Biosciences) before confocal imaging on Zeiss LSM 710 microscope.

Speckle variance optical coherence tomography (OCT) was used for *in vivo* imaging [254]. To visualize projection images of the vasculature within the implanted scaffolds, volume data sets were processed with a speckle variance technique that computes the variance in each pixel over seven repeated A-lines at each lateral position. The resulting speckle variance images represent OCT flow signal for perfused vessels within the imaged volume. Noise due to signal fall-off was excluded by thresholding the corresponding structural images to create a mask, and an average signal projection over the depth (~1 mm) of the speckle variance OCT data was used to visualize all vessels present in the volume. Images were enhanced with an optimized, modified Frangi filter[255] to enhance vessel-like features, and the enhanced image was multiplied by the initial image to accentuate the vessels. Quantification of vessel density was performed using MATLAB (MathWorks, Natick, MA, USA) built-in Canny edge detection [256] to find edge features, and active contours to mask in edges, and the vessel density was calculated as the mask pixels over total pixels in the image.

D.2.6 Statistical Analysis

Comparisons between two groups were performed with a Student's unpaired t test. Comparisons between multiple groups were performed with a one- or two-way analysis of variance (ANOVA) with a Tukey *post hoc* test to adjust p-values for multiple comparisons. In all cases, $p < 0.05$ is considered statistically significant. Mean ± standard deviation is reported, unless otherwise noted.

D.3 Results, Discussion and Conclusion

We first synthesized block copolymers comprised of a cell-repellant unit, poly(ethylene glycol) (PEG), and a cell-adhesive unit, poly(ε-caprolactone) (PCL) at varying compositions (Figure D-1A). Specifically, the length and molar percentage (mol%) of the repellant PEG unit was varied to modulate the cellular response. Copolymer names are abbreviated by the mol% and chain length of the PEG unit, and the remaining content is PCL (i.e. 5%PEG750Da and 5%PEG2kDa are both 95mol% PCL). Based upon our previous findings that PEG chain length and mol% impacts the expression of stemness genes and redox capacity (manuscript under review), we sought to investigate how these factors influence the expression of tissue-reparative, pro-angiogenic factors. Copolymers containing the shorter 750Da PEG chain allowed for moderate cell attachment and spreading (Figure D-1B-C), but cells began aggregating at higher PEG mol%. In contrast the longer 2kDa PEG chains forced cell aggregation or extreme elongation at both PEG mol% tested (Figure D-1D-E). Of note, PEG2kDa copolymers greater than 10 mol% abrogated all cell attachment and were not used for these studies. Representative confocal **(**Figure D-1F-G) and scanning electron (Figure D-1H-I) microscopy images verify the pseudo-three dimensionality of these aggregates; a cell-matrix interactive layer attaches to the material surface, upon which hMSCs aggregate into three-dimensional clusters with limited cytoskeletal staining.

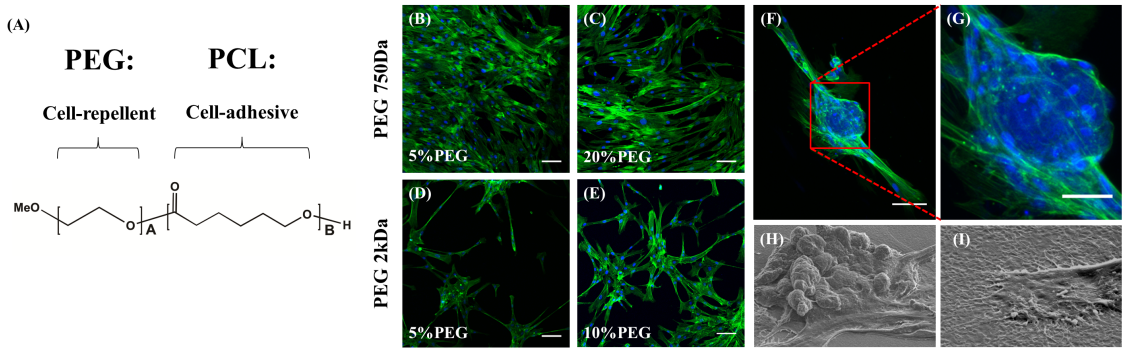

Figure D-1 Copolymers Composed of Cell-repellent and Cell-adhesive Domains Differentially Regulate Cell Attachment and Spreading.
(A) Copolymer structure: a repellent poly(ethylene glycol) (PEG) unit was copolymerized with adhesive poly(ε-caprolactone) (PCL). The length and molar percentage (mol%) of the PEG unit was altered to modulate the degree of repellency. **(B-F)** After four days in culture, hMSCs on PEG750Da substrates were able to attach and spread, but moderate aggregation was observed as the PEG mol% was increased; in contrast, cells on PEG2kDa were highly elongated at the material surface and mostly formed aggregates (green – phalloidin; blue – DAPI). Scale bars = 100 μm. **(F-G)** Representative confocal z-stack projection of hMSC aggregate on 10%PEG2kDa copolymer demonstrating that a matrix-interactive layer of cells forms at the material surface with strong actin staining, and hMSC aggregates with reduced actin signal form on top. Scale bars = (F) 100 μm and (G) 50 μm**.** Scanning electron micrographs of **(H)** a cell aggregate, demonstrating that multiple cells cluster atop a thin cell layer, and **(I)** a cellular protrusion that interacts directly with the material surface.

We next investigated how culture on copolymer substrates modulated the expression profile of beneficial factors. Since HD cultures have been shown to generate a strong anti-inflammatory/pro-angiogenic profile, we first tested how expression of these genes was regulated in our system. TCPS was used as a control substrate since this is the most common culture material used in both laboratory and clinical settings. As seen in Figure 2, expression of the anti-inflammatory cytokines, tumor necrosis factor-inducible gene 6 protein (*TSG-6),* stanniocalcin 1 *(STC1)*, and interleukin-6 (*IL-6)* was drastically enhanced for hMSCs cultured on all copolymer types (Figure D-2A-C). Similarly, expression of the pro-angiogenic factors interleukin-8 (*IL-8)*, angiopoietin-1 *(ANGPT1)*,

epidermal growth factor *(EGF)*, vascular endothelial growth factor A *(VEGF-A)*, and angiogenin *(ANG)* was all enhanced to varying levels on all substrates tested (Figure D-2D-H). Akin to blood vessel formation in the body, hMSCs can organize endothelial cells into tube-like formations and maintain abluminal localization[124]. Therefore, a functional test for proangiogenic potential was performed to verify the regenerative phenotype. hMSCs were cultured on copolymer substrates and TCPS for 3 days and subsequently removed to be co-cultured with endothelial cells on growth factor-reduced Matrigel. Red fluorescent protein (RFP)-expressing human umbilical vein endothelial cells (HUVECs) were used to track endothelial tubes and hMSCs were given a green counterstain (PKH-67) (Figure D-2I). After 8 hours in culture, tube formation was observed for all groups tested. HUVECs alone (EC only) formed an elaborate tube network, and the presence of hMSCs from any material type did not interfere with this behavior. However, at 24 hours, HUVECs alone did not maintain tube formation, and hMSCs from TCPS or 5%PEG750Da substrates did not aid in tube stablization, which led to the formation of large heterogeneous cell clumping. However, hMSCs that had been cultured on 20%PEG750Da, 5%PEG2kDa, or 10%PEG2kDa strongly supported tube stablization and assumed an abluminal localization, similar to what is observed for hMSCs within their *in vivo* niche[113]. In Figure D-2J, the cumulative tube length per image confirms the functional pro-angiogenic capability of hMSCs cultured upon 20%PEG750Da, 5%PEG2kDa, or 10%PEG2kDa copolymer substrates.

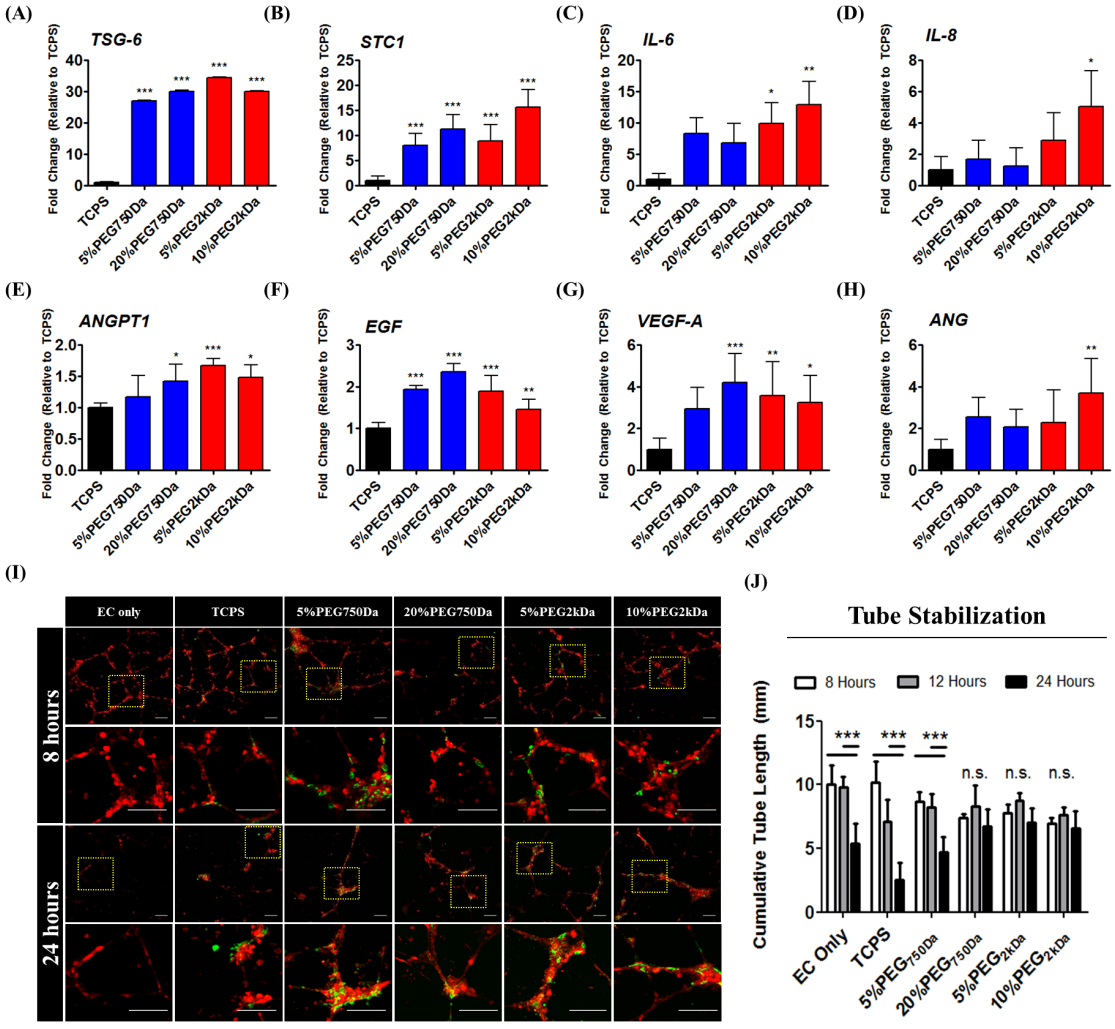

Figure D-2 Copolymers Promote a Pro-angiogenic Expression profile that is Functional *in vitro*.
qRT-PCR analysis of **(A-C)** anti-inflammatory factors *TSG-6, STC1*, and *IL-6* and **(D-H)** pro-angiogenic factors *IL-8, ANGPT1, EGF, VEGF-A,* and *ANG* demonstrates that culture on all copolymer substrates enhances the expression of the tested cytokines. **(I-J)** Tube formation and stabilization assay with RFP-expressing HUVECs. hMSCs were cultured on the different substrates for three days and then moved to co-culture with HUVECs for the indicated time period. After 8 hours, all conditions exhibited tube network formation; however, after 24 hours, only hMSCs that had been cultured on 20%PEG750Da, 5%PEG2kDa, or 10%PEG2kDa were able to stabilize endothelial tube formation. For each time point, the yellow box indicates the area magnified for the image immediately below. Scale bars = 200 μm. The cumulative tube length per image is quantified, verifying these data. $*p < 0.05$, $**p < 0.01$, $***p < 0.005$ versus TCPS control or between groups as indicated by the lines.

Finally, we tested if this effect was functionally conserved hMSCs when cultured within three-dimensional (3D) scaffolds and implanted *in vivo*. For these experiments, 10%PEG2k was fabricated into 3D scaffolds (PEG-PCL) and compared against 100%PCL scaffolds as a "PEG-free" control. As seen in Figure 3, the formation and stabilization of vasculature over a three-week period was the strongest for hMSC-loaded PEG-PCL scaffolds, as evidenced by optical coherence tomography (OCT) imaging (Figure D-3A); of note, these images were collected from the same animal over time. When quantified (N = 7 animals, two-way ANOVA), hMSC-loaded PEG-PCL scaffolds demonstrated a higher density of vessels in each OCT image, as compared to hMSC-loaded PCL scaffolds (Figure D-3B, $p = 0.05$). The increased presence of vasculature was verified *post mortem* by two techniques: fluorescence microangiography (Figure D-3C) and positive staining for the endothelial-specific marker CD31 (Figure D-3D). For both imaging analyses, staining was weakest for PCL scaffolds without hMSCs and strongest for hMSC-loaded PEG-PCL scaffolds. For hMSC-loaded PCL scaffolds, vasculature appeared immature (Figure D-3C) and did not penetrate into the interior of the scaffold (INT, Figure D-3D). In contrast, both the blank and hMSC-loaded PEG-PCL scaffolds promoted strong, stable vascular networks that traversed throughout the material interior. It can be hypothesized that the blank PEG-PCL scaffolds allowed for potent vascularization due to the enhanced degradability derived from PEG-mediated wettability; however, material may also promote a pro-angiogenic response by the host cells with which it interacts.

In summary, the data presented here verify the functionality of PEG-PCL in enhancing a pro-angiogenic, anti-inflammatory phenotype of hMSCs, in both two- and

three-dimensional formats, *in vitro* and *in vivo*. Future work deploying these scaffolds will center on co-culture of hMSC-loaded PEG-PCL scaffolds with other cell types as well as implantation of hMSC-loaded PEG-PCL scaffolds at highly vascularized injury sites such as skin ulcers. Finally, these findings are currently being used to further optimize cell-instructive scaffolds comprised of other synthetic polymer constituents for enhanced therapeutic benefit and regulation of hMSC phenotype.

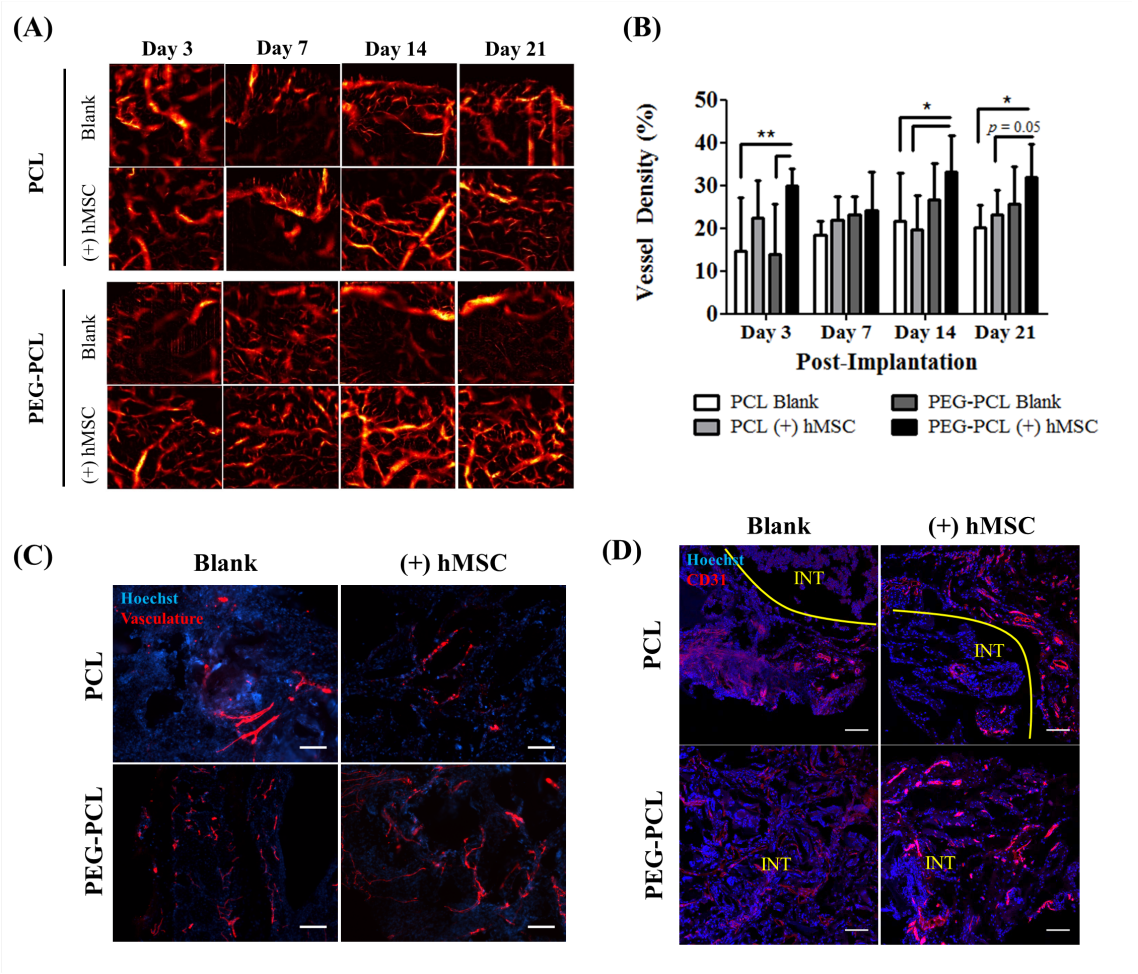

Figure D-3 Pro-angiogenic Capacity of hMSCs is Retained During Culture Within Three-dimensional (3D) PEG-PCL Scaffolds *in vivo*.
Porous, 3D scaffolds were fabricated from 10%PEG2kDa (PEG-PCL) or 100%PCL (PCL) by salt-leaching, and were either left without cells (Blank) or loaded with hMSCs prior to subcutaneous implantation (+ hMSCs). **(A)** Optical coherence tomography (OCT) was used to non-invasively monitor the formation and retention of vasculature over a three-week period. Of note, all OCT images were collected from the same animal over time. **(B)** When quantified, vessel density per image was shown to be highest for the hMSC-loaded PEG-PCL scaffolds, although hMSC-loaded PCL scaffolds demonstrated a similar response. **(C)** Fluorescent microangiographs reveal limited vasculature (red) in blank PCL scaffolds, which was enhanced by the presence of hMSCs; in contrast, both blank and hMSC-loaded PEG-PCL scaffolds exhibited strong signal from the vasculature. All microangiographs were taken from within the scaffold area. **(D)** Immunohistochemistry for CD31 (red) reveals that the interior (INT) of PCL scaffolds for both blank and hMSC-loaded conditions contained relatively poor vascular networks, whereas the PEG-PCL material demonstrated pronounced vasculature throughout the scaffold. Scale bars = 100 μm. $*p < 0.05$, $**p < 0.01$ between groups indicated by the lines.

Table D-1 Primer Sequences

Gene	Accession Number	Forward Primer (5' – 3')	Reverse Primer (3' – 5')	Amplicon (bp)
TSG-6	NM_007115.3	CTCAGCCCTCTTCAAAAACTTCT	TTCACACACCGCCTTAGCTT	95
STC1	NM_003155.2	CACTCAGGGAAAAGCATTCGT	GAAAGTGGAGCACCTCCGAA	97
IL-6	NM_000600.4	CAATGAGGAGACTTGCCTGGTG	GGTTGGGTCAGGGGTGGTTA	193
IL-8	NM_00584.3	ACTCCAAACCTTTCCACCCC	CTCAGCCCTCTTCAAAAACTTCT	173
ANGPT1	NM_001146.3	GCTGACAGATGTTGAGACCCA	TTCCTCCCTTTAGTAAAACACCTTC	395
EGF	NM_001963.4	TGTCCCTTTTTGGTGACCGT	TGTCCCTTTTTGGTGACCGT	197
VEGF-A	NM_001025366.2	CGAGAAGTGCTAGCTCGGG	CTGGGACCACTTGGCATGG	377
ANG	NM_001145.4	GGATCCCAGGCTCGTTCTTT	CTTCCAACACAGGCTCCTCG	378
GAPDH	NM_002046.4	GCACCGTCAAGGCTGAGAAC	TGGTGAAGACGCCAGTGGA	138

REFERENCES

1. Friedenstein AJ, Piatetzky S, II, Petrakova KV. Osteogenesis in transplants of bone marrow cells. *Journal of embryology and experimental morphology*. 1966;16:381-390
2. Pittenger MF, Mackay AM, Beck SC, Jaiswal RK, Douglas R, Mosca JD, Moorman MA, Simonetti DW, Craig S, Marshak DR. Multilineage potential of adult human mesenchymal stem cells. *Science*. 1999;284:143-147
3. Benoit DS, Schwartz MP, Durney AR, Anseth KS. Small functional groups for controlled differentiation of hydrogel-encapsulated human mesenchymal stem cells. *Nat Mater*. 2008;7:816-823
4. Boland GM, Perkins G, Hall DJ, Tuan RS. Wnt 3a promotes proliferation and suppresses osteogenic differentiation of adult human mesenchymal stem cells. *J Cell Biochem*. 2004;93:1210-1230
5. Dalby MJ, Gadegaard N, Tare R, Andar A, Riehle MO, Herzyk P, Wilkinson CD, Oreffo RO. The control of human mesenchymal cell differentiation using nanoscale symmetry and disorder. *Nat Mater*. 2007;6:997-1003
6. Jaiswal RK, Jaiswal N, Bruder SP, Mbalaviele G, Marshak DR, Pittenger MF. Adult human mesenchymal stem cell differentiation to the osteogenic or adipogenic lineage is regulated by mitogen-activated protein kinase. *J Biol Chem*. 2000;275:9645-9652
7. Luu HH, Song WX, Luo X, Manning D, Luo J, Deng ZL, Sharff KA, Montag AG, Haydon RC, He TC. Distinct roles of bone morphogenetic proteins in osteogenic differentiation of mesenchymal stem cells. *J Orthop Res*. 2007;25:665-677
8. Salasznyk RM, Williams WA, Boskey A, Batorsky A, Plopper GE. Adhesion to vitronectin and collagen i promotes osteogenic differentiation of human mesenchymal stem cells. *J Biomed Biotechnol*. 2004;2004:24-34
9. Barry F, Boynton RE, Liu B, Murphy JM. Chondrogenic differentiation of mesenchymal stem cells from bone marrow: Differentiation-dependent gene expression of matrix components. *Exp Cell Res*. 2001;268:189-200
10. Bosnakovski D, Mizuno M, Kim G, Takagi S, Okumura M, Fujinaga T. Chondrogenic differentiation of bovine bone marrow mesenchymal stem cells (mscs) in different hydrogels: Influence of collagen type ii extracellular matrix on msc chondrogenesis. *Biotechnol Bioeng*. 2006;93:1152-1163
11. Cho JH, Kim SH, Park KD, Jung MC, Yang WI, Han SW, Noh JY, Lee JW. Chondrogenic differentiation of human mesenchymal stem cells using a thermosensitive poly(n-isopropylacrylamide) and water-soluble chitosan copolymer. *Biomaterials*. 2004;25:5743-5751
12. Solchaga LA, Penick KJ, Welter JF. Chondrogenic differentiation of bone marrow-derived mesenchymal stem cells: Tips and tricks. *Methods Mol Biol*.698:253-278
13. Scott MA, Nguyen VT, Levi B, James AW. Current methods of adipogenic differentiation of mesenchymal stem cells. *Stem Cells Dev*.20:1793-1804
14. Herzog EL, Chai L, Krause DS. Plasticity of marrow-derived stem cells. *Blood*. 2003;102:3483-3493

15. Wagers AJ, Weissman IL. Plasticity of adult stem cells. *Cell*. 2004;116:639-648
16. Uccelli A, Moretta L, Pistoia V. Mesenchymal stem cells in health and disease. *Nature reviews. Immunology*. 2008;8:726-736
17. Branch MJ, Hashmani K, Dhillon P, Jones DR, Dua HS, Hopkinson A. Mesenchymal stem cells in the human corneal limbal stroma. *Investigative ophthalmology & visual science*. 2012;53:5109-5116
18. Ghaemi SR, Harding FJ, Delalat B, Gronthos S, Voelcker NH. Exploring the mesenchymal stem cell niche using high throughput screening. *Biomaterials*. 2013;34:7601-7615
19. Eglitis MA, Mezey E. Hematopoietic cells differentiate into both microglia and macroglia in the brains of adult mice. *Proceedings of the National Academy of Sciences of the United States of America*. 1997;94:4080-4085
20. Ferrari G, Cusella-De Angelis G, Coletta M, Paolucci E, Stornaiuolo A, Cossu G, Mavilio F. Muscle regeneration by bone marrow-derived myogenic progenitors. *Science*. 1998;279:1528-1530
21. Mezey E, Chandross KJ, Harta G, Maki RA, McKercher SR. Turning blood into brain: Cells bearing neuronal antigens generated in vivo from bone marrow. *Science*. 2000;290:1779-1782
22. Orlic D, Kajstura J, Chimenti S, Jakoniuk I, Anderson SM, Li B, Pickel J, McKay R, Nadal-Ginard B, Bodine DM, Leri A, Anversa P. Bone marrow cells regenerate infarcted myocardium. *Nature*. 2001;410:701-705
23. Kolf CM, Cho E, Tuan RS. Mesenchymal stromal cells. Biology of adult mesenchymal stem cells: Regulation of niche, self-renewal and differentiation. *Arthritis Res Ther*. 2007;9:204
24. McMurray RJ, Gadegaard N, Tsimbouri PM, Burgess KV, McNamara LE, Tare R, Murawski K, Kingham E, Oreffo RO, Dalby MJ. Nanoscale surfaces for the long-term maintenance of mesenchymal stem cell phenotype and multipotency. *Nat Mater*.10:637-644
25. Mirmalek-Sani SH, Tare RS, Morgan SM, Roach HI, Wilson DI, Hanley NA, Oreffo RO. Characterization and multipotentiality of human fetal femur-derived cells: Implications for skeletal tissue regeneration. *Stem Cells*. 2006;24:1042-1053
26. Lange C, Bassler P, Lioznov MV, Bruns H, Kluth D, Zander AR, Fiegel HC. Liver-specific gene expression in mesenchymal stem cells is induced by liver cells. *World journal of gastroenterology*. 2005;11:4497-4504
27. Houghton J, Stoicov C, Nomura S, Rogers AB, Carlson J, Li H, Cai X, Fox JG, Goldenring JR, Wang TC. Gastric cancer originating from bone marrow-derived cells. *Science*. 2004;306:1568-1571
28. Choi KS, Shin JS, Lee JJ, Kim YS, Kim SB, Kim CW. In vitro trans-differentiation of rat mesenchymal cells into insulin-producing cells by rat pancreatic extract. *Biochemical and biophysical research communications*. 2005;330:1299-1305
29. Sato Y, Araki H, Kato J, Nakamura K, Kawano Y, Kobune M, Sato T, Miyanishi K, Takayama T, Takahashi M, Takimoto R, Iyama S, Matsunaga T, Ohtani S, Matsuura A, Hamada H, Niitsu Y. Human mesenchymal stem cells xenografted directly to rat liver are differentiated into human hepatocytes without fusion. *Blood*. 2005;106:756-763

30. Kopen GC, Prockop DJ, Phinney DG. Marrow stromal cells migrate throughout forebrain and cerebellum, and they differentiate into astrocytes after injection into neonatal mouse brains. *Proceedings of the National Academy of Sciences of the United States of America*. 1999;96:10711-10716
31. da Silva Meirelles L, Chagastelles PC, Nardi NB. Mesenchymal stem cells reside in virtually all post-natal organs and tissues. *Journal of cell science*. 2006;119:2204-2213
32. Sakaguchi Y, Sekiya I, Yagishita K, Muneta T. Comparison of human stem cells derived from various mesenchymal tissues: Superiority of synovium as a cell source. *Arthritis and rheumatism*. 2005;52:2521-2529
33. Majumdar MK, Thiede MA, Mosca JD, Moorman M, Gerson SL. Phenotypic and functional comparison of cultures of marrow-derived mesenchymal stem cells (mscs) and stromal cells. *Journal of cellular physiology*. 1998;176:57-66
34. Jansen BJ, Gilissen C, Roelofs H, Schaap-Oziemlak A, Veltman JA, Raymakers RA, Jansen JH, Kogler G, Figdor CG, Torensma R, Adema GJ. Functional differences between mesenchymal stem cell populations are reflected by their transcriptome. *Stem Cells Dev*. 2010;19:481-490
35. Behfar A, Crespo-Diaz R, Terzic A, Gersh BJ. Cell therapy for cardiac repair--lessons from clinical trials. *Nature reviews. Cardiology*. 2014;11:232-246
36. Mendicino M, Bailey AM, Wonnacott K, Puri RK, Bauer SR. Msc-based product characterization for clinical trials: An fda perspective. *Cell Stem Cell*.14:141-145
37. LeBlanc K, Frassoni F, Ball L, Locatelli F, Roelofs H, Lewis I, Lanino E, Sundberg B, Bernardo ME, Remberger M, Dini G, Egeler RM, Bacigalupo A, Fibbe W, Ringden O, M DCEGB. Mesenchymal stem cells for treatment of steroid-resistant, severe, acute graft-versus-host disease: A phase ii study. *Lancet*. 2008;371:1579-1586
38. Ranganath SH, Levy O, Inamdar MS, Karp JM. Harnessing the mesenchymal stem cell secretome for the treatment of cardiovascular disease. *Cell Stem Cell*.10:244-258
39. Bianco P, Cao X, Frenette PS, Mao JJ, Robey PG, Simmons PJ, Wang CY. The meaning, the sense and the significance: Translating the science of mesenchymal stem cells into medicine. *Nature medicine*. 2013;19:35-42
40. Roobrouck VD, Ulloa-Montoya F, Verfaillie CM. Self-renewal and differentiation capacity of young and aged stem cells. *Exp Cell Res*. 2008;314:1937-1944
41. Stolzing A, Jones E, McGonagle D, Scutt A. Age-related changes in human bone marrow-derived mesenchymal stem cells: Consequences for cell therapies. *Mechanisms of ageing and development*. 2008;129:163-173
42. Wagner W, Bork S, Horn P, Krunic D, Walenda T, Diehlmann A, Benes V, Blake J, Huber FX, Eckstein V, Boukamp P, Ho AD. Aging and replicative senescence have related effects on human stem and progenitor cells. *PLoS One*. 2009;4:e5846
43. Wagner W, Horn P, Castoldi M, Diehlmann A, Bork S, Saffrich R, Benes V, Blake J, Pfister S, Eckstein V, Ho AD. Replicative senescence of mesenchymal stem cells: A continuous and organized process. *PLoS One*. 2008;3:e2213
44. Hayflick L, Moorhead PS. The serial cultivation of human diploid cell strains. *Exp Cell Res*. 1961;25:585-621

45. Shay JW, Wright WE. Hayflick, his limit, and cellular ageing. *Nature reviews. Molecular cell biology*. 2000;1:72-76
46. Blackburn EH, Gall JG. A tandemly repeated sequence at the termini of the extrachromosomal ribosomal rna genes in tetrahymena. *Journal of molecular biology*. 1978;120:33-53
47. Hayflick L. The coming of age of wi-38. *Advances in Cell Culture*. 1984;3:303-316
48. Wright WE, Hayflick L. Nuclear control of cellular aging demonstrated by hybridization of anucleate and whole cultured normal human fibroblasts. *Exp Cell Res*. 1975;96:113-121
49. Hayflick L. How and why we age. *Experimental gerontology*. 1998;33:639-653
50. Sames K, Stolzing A. *Extending the lifespan: Biotechnical, gerontological, and social problems*. LIT Verlag; 2005.
51. Campisi J. Cancer, aging and cellular senescence. *In vivo*. 2000;14:183-188
52. Itahana K, Dimri G, Campisi J. Regulation of cellular senescence by p53. *European journal of biochemistry / FEBS*. 2001;268:2784-2791
53. Heo JY, Jing K, Song KS, Seo KS, Park JH, Kim JS, Jung YJ, Hur GM, Jo DY, Kweon GR, Yoon WH, Lim K, Hwang BD, Jeon BH, Park JI. Downregulation of ape1/ref-1 is involved in the senescence of mesenchymal stem cells. *Stem Cells*. 2009;27:1455-1462
54. Crowder SW, Horton LW, Lee SH, McClain CM, Hawkins OE, Palmer AM, Bae H, Richmond A, Sung HJ. Passage-dependent cancerous transformation of human mesenchymal stem cells under carcinogenic hypoxia. *FASEB J*.27:2788-2798
55. Stenderup K, Justesen J, Clausen C, Kassem M. Aging is associated with decreased maximal life span and accelerated senescence of bone marrow stromal cells. *Bone*. 2003;33:919-926
56. Mauney JR, Kaplan DL, Volloch V. Matrix-mediated retention of osteogenic differentiation potential by human adult bone marrow stromal cells during ex vivo expansion. *Biomaterials*. 2004;25:3233-3243
57. Baxter MA, Wynn RF, Jowitt SN, Wraith JE, Fairbairn LJ, Bellantuono I. Study of telomere length reveals rapid aging of human marrow stromal cells following in vitro expansion. *Stem Cells*. 2004;22:675-682
58. Muraglia A, Cancedda R, Quarto R. Clonal mesenchymal progenitors from human bone marrow differentiate in vitro according to a hierarchical model. *Journal of cell science*. 2000;113 (Pt 7):1161-1166
59. Rombouts WJ, Ploemacher RE. Primary murine msc show highly efficient homing to the bone marrow but lose homing ability following culture. *Leukemia*. 2003;17:160-170
60. Prockop DJ, Gregory CA, Spees JL. One strategy for cell and gene therapy: Harnessing the power of adult stem cells to repair tissues. *Proceedings of the National Academy of Sciences of the United States of America*. 2003;100 Suppl 1:11917-11923
61. Park JS, Kim HY, Kim HW, Chae GN, Oh HT, Park JY, Shim H, Seo M, Shin EY, Kim EG, Park SC, Kwak SJ. Increased caveolin-1, a cause for the declined adipogenic potential of senescent human mesenchymal stem cells. *Mechanisms of ageing and development*. 2005;126:551-559

62. Mendes SC, Tibbe JM, Veenhof M, Bakker K, Both S, Platenburg PP, Oner FC, de Bruijn JD, van Blitterswijk CA. Bone tissue-engineered implants using human bone marrow stromal cells: Effect of culture conditions and donor age. *Tissue engineering*. 2002;8:911-920
63. Liu L, DiGirolamo CM, Navarro PA, Blasco MA, Keefe DL. Telomerase deficiency impairs differentiation of mesenchymal stem cells. *Exp Cell Res*. 2004;294:1-8
64. Globerson A. Thymocytopoiesis in aging: The bone marrow-thymus axis. *Archives of gerontology and geriatrics*. 1997;24:141-155
65. Bruder SP, Jaiswal N, Haynesworth SE. Growth kinetics, self-renewal, and the osteogenic potential of purified human mesenchymal stem cells during extensive subcultivation and following cryopreservation. *J Cell Biochem*. 1997;64:278-294
66. Banfi A, Muraglia A, Dozin B, Mastrogiacomo M, Cancedda R, Quarto R. Proliferation kinetics and differentiation potential of ex vivo expanded human bone marrow stromal cells: Implications for their use in cell therapy. *Experimental hematology*. 2000;28:707-715
67. Petite H, Viateau V, Bensaid W, Meunier A, de Pollak C, Bourguignon M, Oudina K, Sedel L, Guillemin G. Tissue-engineered bone regeneration. *Nature biotechnology*. 2000;18:959-963
68. Bara JJ, Richards RG, Alini M, Stoddart MJ. Concise review: Bone marrow-derived mesenchymal stem cells change phenotype following in vitro culture: Implications for basic research and the clinic. *Stem Cells*. 2014;32:1713-1723
69. Sethe S, Scutt A, Stolzing A. Aging of mesenchymal stem cells. *Ageing research reviews*. 2006;5:91-116
70. Bartosh TJ, Ylostalo JH, Mohammadipoor A, Bazhanov N, Coble K, Claypool K, Lee RH, Choi H, Prockop DJ. Aggregation of human mesenchymal stromal cells (mscs) into 3d spheroids enhances their antiinflammatory properties. *Proceedings of the National Academy of Sciences of the United States of America*.107:13724-13729
71. Yu KR, Yang SR, Jung JW, Kim H, Ko K, Han DW, Park SB, Choi SW, Kang SK, Scholer H, Kang KS. Cd49f enhances multipotency and maintains stemness through the direct regulation of oct4 and sox2. *Stem Cells*.30:876-887
72. Sart S, Tsai AC, Li Y, Ma T. Three-dimensional aggregates of mesenchymal stem cells: Cellular mechanisms, biological properties, and applications. *Tissue engineering. Part B, Reviews*. 2013
73. Cesarz Z, Tamama K. Spheroid culture of mesenchymal stem cells. *Stem cells international*. 2016;2016:9176357
74. Mueller-Klieser W. Three-dimensional cell cultures: From molecular mechanisms to clinical applications. *The American journal of physiology*. 1997;273:C1109-1123
75. Huang GS, Dai LG, Yen BL, Hsu SH. Spheroid formation of mesenchymal stem cells on chitosan and chitosan-hyaluronan membranes. *Biomaterials*. 2011;32:6929-6945
76. Cheng NC, Wang S, Young TH. The influence of spheroid formation of human adipose-derived stem cells on chitosan films on stemness and differentiation capabilities. *Biomaterials*. 2012;33:1748-1758

77. Cheng NC, Chen SY, Li JR, Young TH. Short-term spheroid formation enhances the regenerative capacity of adipose-derived stem cells by promoting stemness, angiogenesis, and chemotaxis. *Stem cells translational medicine*. 2013;2:584-594
78. Frith JE, Thomson B, Genever PG. Dynamic three-dimensional culture methods enhance mesenchymal stem cell properties and increase therapeutic potential. *Tissue engineering. Part C, Methods*. 2010;16:735-749
79. Bartosh TJ, Ylostalo JH, Mohammadipoor A, Bazhanov N, Coble K, Claypool K, Lee RH, Choi H, Prockop DJ. Aggregation of human mesenchymal stromal cells (mscs) into 3d spheroids enhances their antiinflammatory properties. *Proceedings of the National Academy of Sciences of the United States of America*. 2010;107:13724-13729
80. Lin RZ, Chang HY. Recent advances in three-dimensional multicellular spheroid culture for biomedical research. *Biotechnology journal*. 2008;3:1172-1184
81. Leight JL, Liu WF, Chaturvedi RR, Chen S, Yang MT, Raghavan S, Chen CS. Manipulation of 3d cluster size and geometry by release from 2d micropatterns. *Cellular and molecular bioengineering*. 2012;5:299-306
82. Baraniak PR, McDevitt TC. Scaffold-free culture of mesenchymal stem cell spheroids in suspension preserves multilineage potential. *Cell and tissue research*. 2012;347:701-711
83. Tsai AC, Liu Y, Yuan X, Ma T. Compaction, fusion, and functional activation of three-dimensional human mesenchymal stem cell aggregate. *Tissue engineering. Part A*. 2015;21:1705-1719
84. Mueller-Klieser W. Multicellular spheroids. A review on cellular aggregates in cancer research. *Journal of cancer research and clinical oncology*. 1987;113:101-122
85. Wang W, Itaka K, Ohba S, Nishiyama N, Chung UI, Yamasaki Y, Kataoka K. 3d spheroid culture system on micropatterned substrates for improved differentiation efficiency of multipotent mesenchymal stem cells. *Biomaterials*. 2009;30:2705-2715
86. Miyagawa Y, Okita H, Hiroyama M, Sakamoto R, Kobayashi M, Nakajima H, Katagiri YU, Fujimoto J, Hata J, Umezawa A, Kiyokawa N. A microfabricated scaffold induces the spheroid formation of human bone marrow-derived mesenchymal progenitor cells and promotes efficient adipogenic differentiation. *Tissue engineering. Part A*. 2011;17:513-521
87. Hildebrandt C, Buth H, Thielecke H. A scaffold-free in vitro model for osteogenesis of human mesenchymal stem cells. *Tissue & cell*. 2011;43:91-100
88. Lee RH, Seo MJ, Pulin AA, Gregory CA, Ylostalo J, Prockop DJ. The cd34-like protein podxl and alpha6-integrin (cd49f) identify early progenitor mscs with increased clonogenicity and migration to infarcted heart in mice. *Blood*. 2009;113:816-826
89. Sart S, Tsai AC, Li Y, Ma T. Three-dimensional aggregates of mesenchymal stem cells: Cellular mechanisms, biological properties, and applications. *Tissue engineering. Part B, Reviews*.
90. Chan HF, Zhang Y, Ho YP, Chiu YL, Jung Y, Leong KW. Rapid formation of multicellular spheroids in double-emulsion droplets with controllable microenvironment. *Sci Rep-Uk*. 2013;3

91. Wang WJ, Itaka K, Ohba S, Nishiyama N, Chung UI, Yamasaki Y, Kataoka K. 3d spheroid culture system on micropatterned substrates for improved differentiation efficiency of multipotent mesenchymal stem cells. *Biomaterials*. 2009;30:2705-2715
92. Lepperdinger G, Brunauer R, Jamnig A, Laschober G, Kassem M. Controversial issue: Is it safe to employ mesenchymal stem cells in cell-based therapies? *Experimental gerontology*. 2008;43:1018-1023
93. Jiang S, Kh Haider H, Ahmed RP, Idris NM, Salim A, Ashraf M. Transcriptional profiling of young and old mesenchymal stem cells in response to oxygen deprivation and reparability of the infarcted myocardium. *Journal of molecular and cellular cardiology*. 2008;44:582-596
94. Fehrer C, Lepperdinger G. Mesenchymal stem cell aging. *Experimental gerontology*. 2005;40:926-930
95. Crisostomo PR, Wang M, Wairiuko GM, Morrell ED, Terrell AM, Seshadri P, Nam UH, Meldrum DR. High passage number of stem cells adversely affects stem cell activation and myocardial protection. *Shock*. 2006;26:575-580
96. Campisi J. From cells to organisms: Can we learn about aging from cells in culture? *Experimental gerontology*. 2001;36:607-618
97. Campisi J. Replicative senescence: An old lives' tale? *Cell*. 1996;84:497-500
98. Armulik A, Genove G, Betsholtz C. Pericytes: Developmental, physiological, and pathological perspectives, problems, and promises. *Dev Cell*.21:193-215
99. Armulik A, Abramsson A, Betsholtz C. Endothelial/pericyte interactions. *Circ Res*. 2005;97:512-523
100. Gerhardt H, Betsholtz C. Endothelial-pericyte interactions in angiogenesis. *Cell and tissue research*. 2003;314:15-23
101. Ribatti D, Nico B, Crivellato E. The role of pericytes in angiogenesis. *Int J Dev Biol*.55:261-268
102. Stratman AN, Davis GE. Endothelial cell-pericyte interactions stimulate basement membrane matrix assembly: Influence on vascular tube remodeling, maturation, and stabilization. *Microsc Microanal*.18:68-80
103. Davis S, Aldrich TH, Jones PF, Acheson A, Compton DL, Jain V, Ryan TE, Bruno J, Radziejewski C, Maisonpierre PC, Yancopoulos GD. Isolation of angiopoietin-1, a ligand for the tie2 receptor, by secretion-trap expression cloning. *Cell*. 1996;87:1161-1169
104. Shyu KG, Manor O, Magner M, Yancopoulos GD, Isner JM. Direct intramuscular injection of plasmid DNA encoding angiopoietin-1 but not angiopoietin-2 augments revascularization in the rabbit ischemic hindlimb. *Circulation*. 1998;98:2081-2087
105. Kobayashi H, DeBusk LM, Babichev YO, Dumont DJ, Lin PC. Hepatocyte growth factor mediates angiopoietin-induced smooth muscle cell recruitment. *Blood*. 2006;108:1260-1266
106. Gale NW, Thurston G, Hackett SF, Renard R, Wang Q, McClain J, Martin C, Witte C, Witte MH, Jackson D, Suri C, Campochiaro PA, Wiegand SJ, Yancopoulos GD. Angiopoietin-2 is required for postnatal angiogenesis and lymphatic patterning, and only the latter role is rescued by angiopoietin-1. *Dev Cell*. 2002;3:411-423

107. Fiedler U, Scharpfenecker M, Koidl S, Hegen A, Grunow V, Schmidt JM, Kriz W, Thurston G, Augustin HG. The tie-2 ligand angiopoietin-2 is stored in and rapidly released upon stimulation from endothelial cell weibel-palade bodies. *Blood*. 2004;103:4150-4156
108. Saharinen P, Alitalo K. The yin, the yang, and the angiopoietin-1. *J Clin Invest*.121:2157-2159
109. Caplan AI. All mscs are pericytes? *Cell Stem Cell*. 2008;3:229-230
110. Tsai CC, Su PF, Huang YF, Yew TL, Hung SC. Oct4 and nanog directly regulate dnmt1 to maintain self-renewal and undifferentiated state in mesenchymal stem cells. *Mol Cell*.47:169-182
111. Corselli M, Chin CJ, Parekh C, Sahaghian A, Wang W, Ge S, Evseenko D, Wang X, Montelatici E, Lazzari L, Crooks GM, Peault B. Perivascular support of human hematopoietic stem/progenitor cells. *Blood*.121:2891-2901
112. Kusumbe AP, Ramasamy SK, Adams RH. Coupling of angiogenesis and osteogenesis by a specific vessel subtype in bone. *Nature*. 2014;507:323-328
113. Crisan M, Yap S, Casteilla L, Chen CW, Corselli M, Park TS, Andriolo G, Sun B, Zheng B, Zhang L, Norotte C, Teng PN, Traas J, Schugar R, Deasy BM, Badylak S, Buhring HJ, Giacobino JP, Lazzari L, Huard J, Peault B. A perivascular origin for mesenchymal stem cells in multiple human organs. *Cell Stem Cell*. 2008;3:301-313
114. Winkler EA, Bell RD, Zlokovic BV. Central nervous system pericytes in health and disease. *Nature neuroscience*. 2011;14:1398-1405
115. Armulik A, Genove G, Betsholtz C. Pericytes: Developmental, physiological, and pathological perspectives, problems, and promises. *Dev Cell*. 2011;21:193-215
116. Riha GM, Lin PH, Lumsden AB, Yao Q, Chen C. Review: Application of stem cells for vascular tissue engineering. *Tissue engineering*. 2005;11:1535-1552
117. Doorn J, Fernandes HA, Le BQ, van de Peppel J, van Leeuwen JP, De Vries MR, Aref Z, Quax PH, Myklebost O, Saris DB, van Blitterswijk CA, de Boer J. A small molecule approach to engineering vascularized tissue. *Biomaterials*.34:3053-3063
118. O'Cearbhaill ED, Murphy M, Barry F, McHugh PE, Barron V. Behavior of human mesenchymal stem cells in fibrin-based vascular tissue engineering constructs. *Ann Biomed Eng*.38:649-657
119. Dong JD, Gu YQ, Li CM, Wang CR, Feng ZG, Qiu RX, Chen B, Li JX, Zhang SW, Wang ZG, Zhang J. Response of mesenchymal stem cells to shear stress in tissue-engineered vascular grafts. *Acta Pharmacol Sin*. 2009;30:530-536
120. Krawiec JT, Vorp DA. Adult stem cell-based tissue engineered blood vessels: A review. *Biomaterials*.33:3388-3400
121. Ball SG, Shuttleworth CA, Kielty CM. Mesenchymal stem cells and neovascularization: Role of platelet-derived growth factor receptors. *J Cell Mol Med*. 2007;11:1012-1030
122. Au P, Tam J, Fukumura D, Jain RK. Bone marrow-derived mesenchymal stem cells facilitate engineering of long-lasting functional vasculature. *Blood*. 2008;111:4551-4558

123. Zouani OF, Lei Y, Durrieu MC. Pericytes, stem-cell-like cells, but not mesenchymal stem cells are recruited to support microvascular tube stabilization. *Small*.9:3070-3075
124. Blocki A, Wang Y, Koch M, Peh P, Beyer S, Law P, Hui J, Raghunath M. Not all mscs can act as pericytes: Functional in vitro assays to distinguish pericytes from other mesenchymal stem cells in angiogenesis. *Stem Cells Dev*.22:2347-2355
125. He W, Nieponice A, Soletti L, Hong Y, Gharaibeh B, Crisan M, Usas A, Peault B, Huard J, Wagner WR, Vorp DA. Pericyte-based human tissue engineered vascular grafts. *Biomaterials*. 2010;31:8235-8244
126. Fuoco C, Sangalli E, Vono R, Testa S, Sacchetti B, Latronico MV, Bernardini S, Madeddu P, Cesareni G, Seliktar D, Rizzi R, Bearzi C, Cannata SM, Spinetti G, Gargioli C. 3d hydrogel environment rejuvenates aged pericytes for skeletal muscle tissue engineering. *Frontiers in physiology*. 2014;5:203
127. Saik JE, Gould DJ, Watkins EM, Dickinson ME, West JL. Covalently immobilized platelet-derived growth factor-bb promotes angiogenesis in biomimetic poly(ethylene glycol) hydrogels. *Acta biomaterialia*. 2011;7:133-143
128. Guijarro-Munoz I, Compte M, Alvarez-Cienfuegos A, Alvarez-Vallina L, Sanz L. Lipopolysaccharide activates toll-like receptor 4 (tlr4)-mediated nf-kappab signaling pathway and proinflammatory response in human pericytes. *J Biol Chem*. 2014;289:2457-2468
129. Murphy WL, McDevitt TC, Engler AJ. Materials as stem cell regulators. *Nat Mater*. 2014;13:547-557
130. Pelham RJ, Jr., Wang Y. Cell locomotion and focal adhesions are regulated by substrate flexibility. *Proceedings of the National Academy of Sciences of the United States of America*. 1997;94:13661-13665
131. Huebsch N, Arany PR, Mao AS, Shvartsman D, Ali OA, Bencherif SA, Rivera-Feliciano J, Mooney DJ. Harnessing traction-mediated manipulation of the cell/matrix interface to control stem-cell fate. *Nat Mater*. 2010;9:518-526
132. Khetan S, Guvendiren M, Legant WR, Cohen DM, Chen CS, Burdick JA. Degradation-mediated cellular traction directs stem cell fate in covalently crosslinked three-dimensional hydrogels. *Nat Mater*. 2013;12:458-465
133. Engler AJ, Sen S, Sweeney HL, Discher DE. Matrix elasticity directs stem cell lineage specification. *Cell*. 2006;126:677-689
134. Trappmann B, Gautrot JE, Connelly JT, Strange DG, Li Y, Oyen ML, Cohen Stuart MA, Boehm H, Li B, Vogel V, Spatz JP, Watt FM, Huck WT. Extracellular-matrix tethering regulates stem-cell fate. *Nat Mater*. 2012;11:642-649
135. Wen JH, Vincent LG, Fuhrmann A, Choi YS, Hribar KC, Taylor-Weiner H, Chen S, Engler AJ. Interplay of matrix stiffness and protein tethering in stem cell differentiation. *Nat Mater*. 2014
136. Gilbert PM, Havenstrite KL, Magnusson KE, Sacco A, Leonardi NA, Kraft P, Nguyen NK, Thrun S, Lutolf MP, Blau HM. Substrate elasticity regulates skeletal muscle stem cell self-renewal in culture. *Science*. 2010;329:1078-1081
137. Aragona M, Panciera T, Manfrin A, Giulitti S, Michielin F, Elvassore N, Dupont S, Piccolo S. A mechanical checkpoint controls multicellular growth through yap/taz regulation by actin-processing factors. *Cell*. 2013;154:1047-1059

138. Dupont S, Morsut L, Aragona M, Enzo E, Giulitti S, Cordenonsi M, Zanconato F, Le Digabel J, Forcato M, Bicciato S, Elvassore N, Piccolo S. Role of yap/taz in mechanotransduction. *Nature*. 2011;474:179-183
139. Yang C, Tibbitt MW, Basta L, Anseth KS. Mechanical memory and dosing influence stem cell fate. *Nat Mater*. 2014;13:645-652
140. McMurray RJ, Gadegaard N, Tsimbouri PM, Burgess KV, McNamara LE, Tare R, Murawski K, Kingham E, Oreffo RO, Dalby MJ. Nanoscale surfaces for the long-term maintenance of mesenchymal stem cell phenotype and multipotency. *Nat Mater*. 2011;10:637-644
141. Kong YP, Tu CH, Donovan PJ, Yee AF. Expression of oct4 in human embryonic stem cells is dependent on nanotopographical configuration. *Acta biomaterialia*. 2013;9:6369-6380
142. Watari S, Hayashi K, Wood JA, Russell P, Nealey PF, Murphy CJ, Genetos DC. Modulation of osteogenic differentiation in hmscs cells by submicron topographically-patterned ridges and grooves. *Biomaterials*. 2012;33:128-136
143. Kim DH, Provenzano PP, Smith CL, Levchenko A. Matrix nanotopography as a regulator of cell function. *The Journal of cell biology*. 2012;197:351-360
144. Guvendiren M, Burdick JA. Stem cell response to spatially and temporally displayed and reversible surface topography. *Advanced healthcare materials*. 2013;2:155-164
145. Downing TL, Soto J, Morez C, Houssin T, Fritz A, Yuan F, Chu J, Patel S, Schaffer DV, Li S. Biophysical regulation of epigenetic state and cell reprogramming. *Nat Mater*. 2013;12:1154-1162
146. Li WJ, Laurencin CT, Caterson EJ, Tuan RS, Ko FK. Electrospun nanofibrous structure: A novel scaffold for tissue engineering. *Journal of biomedical materials research*. 2002;60:613-621
147. Flemming RG, Murphy CJ, Abrams GA, Goodman SL, Nealey PF. Effects of synthetic micro- and nano-structured surfaces on cell behavior. *Biomaterials*. 1999;20:573-588
148. Jang JH, Castano O, Kim HW. Electrospun materials as potential platforms for bone tissue engineering. *Advanced drug delivery reviews*. 2009;61:1065-1083
149. Curran JM, Chen R, Hunt JA. Controlling the phenotype and function of mesenchymal stem cells in vitro by adhesion to silane-modified clean glass surfaces. *Biomaterials*. 2005;26:7057-7067
150. Zonca MR, Jr., Yune PS, Heldt CL, Belfort G, Xie Y. High-throughput screening of substrate chemistry for embryonic stem cell attachment, expansion, and maintaining pluripotency. *Macromolecular bioscience*. 2013;13:177-190
151. Gandavarapu NR, Mariner PD, Schwartz MP, Anseth KS. Extracellular matrix protein adsorption to phosphate-functionalized gels from serum promotes osteogenic differentiation of human mesenchymal stem cells. *Acta biomaterialia*. 2013;9:4525-4534
152. Choi S, Murphy WL. The effect of mineral coating morphology on mesenchymal stem cell attachment and expansion. *Journal of materials chemistry*. 2012;22:25288-25295
153. Choi S, Yu X, Jongpaiboonkit L, Hollister SJ, Murphy WL. Inorganic coatings for optimized non-viral transfection of stem cells. *Sci Rep*. 2013;3:1567

154. Mei Y, Saha K, Bogatyrev SR, Yang J, Hook AL, Kalcioglu ZI, Cho SW, Mitalipova M, Pyzocha N, Rojas F, Van Vliet KJ, Davies MC, Alexander MR, Langer R, Jaenisch R, Anderson DG. Combinatorial development of biomaterials for clonal growth of human pluripotent stem cells. *Nat Mater*. 2010;9:768-778
155. Yang J, Mei Y, Hook AL, Taylor M, Urquhart AJ, Bogatyrev SR, Langer R, Anderson DG, Davies MC, Alexander MR. Polymer surface functionalities that control human embryoid body cell adhesion revealed by high throughput surface characterization of combinatorial material microarrays. *Biomaterials*. 2010;31:8827-8838
156. Huang GS, Dai LG, Yen BL, Hsu SH. Spheroid formation of mesenchymal stem cells on chitosan and chitosan-hyaluronan membranes. *Biomaterials*.32:6929-6945
157. Rustad KC, Wong VW, Sorkin M, Glotzbach JP, Major MR, Rajadas J, Longaker MT, Gurtner GC. Enhancement of mesenchymal stem cell angiogenic capacity and stemness by a biomimetic hydrogel scaffold. *Biomaterials*.33:80-90
158. Zhang D, Kilian KA. The effect of mesenchymal stem cell shape on the maintenance of multipotency. *Biomaterials*.34:3962-3969
159. Crowder SW, Leonardo V, Whittaker T, Papathanasiou P, Stevens MM. Material cues as potent regulators of epigenetics and stem cell function. *Cell Stem Cell*. 2016;18:39-52
160. Jeon H, Koo S, Reese WM, Loskill P, Grigoropoulos CP, Healy KE. Directing cell migration and organization via nanocrater-patterned cell-repellent interfaces. *Nat Mater*. 2015;14:918-923
161. Schieber M, Chandel NS. Ros function in redox signaling and oxidative stress. *Curr Biol*. 2014;24:R453-462
162. Ito K, Suda T. Metabolic requirements for the maintenance of self-renewing stem cells. *Nature reviews. Molecular cell biology*. 2014;15:243-256
163. Yao X, Peng R, Ding J. Cell-material interactions revealed via material techniques of surface patterning. *Adv Mater*. 2013;25:5257-5286
164. Bernard AB, Lin CC, Anseth KS. A microwell cell culture platform for the aggregation of pancreatic beta-cells. *Tissue engineering. Part C, Methods*. 2012;18:583-592
165. Hsu SH, Huang GS. Substrate-dependent wnt signaling in msc differentiation within biomaterial-derived 3d spheroids. *Biomaterials*. 2013;34:4725-4738
166. Crowder SW, Gupta MK, Hofmeister LH, Zachman AL, Sung HJ. Modular polymer design to regulate phenotype and oxidative response of human coronary artery cells for potential stent coating applications. *Acta biomaterialia*. 2012;8:559-569
167. Weber N, Wendel HP, Kohn J. Formation of viscoelastic protein layers on polymeric surfaces relevant to platelet adhesion. *J Biomed Mater Res A*. 2005;72:420-427
168. Sader JE, Chon JWM, Mulvaney P. Calibration of rectangular atomic force microscope cantilevers. *Rev Sci Instrum*. 1999;70:3967-3969
169. Poon B, Rittel D, Ravichandran G. An analysis of nanoindentation in linearly elastic solids. *Int J Solids Struct*. 2008;45:6018-6033

170. Choi C, Chae S, Kim T, Jang M, Cho C, Nah J. Preparation and characterizations of poly(ethylene glycol)-poly(ε-caprolactone) block copolymer nanoparticles. *Bulletin- Korean Chemical Society* 2005;26:523-528
171. Stevens D, Watson H, LeBlanc M, Wang R, Chou J, Bauer W, Harth E. Practical polymerization of functionalized lactones and carbonates with sn(otf)2 in metal catalysed ringopening polymerization methods. *Polymer Chemistry*. 2013;4
172. Go MJ, Takenaka C, Ohgushi H. Forced expression of sox2 or nanog in human bone marrow derived mesenchymal stem cells maintains their expansion and differentiation capabilities. *Exp Cell Res*. 2008;314:1147-1154
173. Tsai CC, Su PF, Huang YF, Yew TL, Hung SC. Oct4 and nanog directly regulate dnmt1 to maintain self-renewal and undifferentiated state in mesenchymal stem cells. *Mol Cell*. 2012;47:169-182
174. Sung HJ, Luk A, Murthy NS, Liu E, Jois M, Joy A, Bushman J, Moghe PV, Kohn J. Poly(ethylene glycol) as a sensitive regulator of cell survival fate on polymeric biomaterials: The interplay of cell adhesion and pro-oxidant signaling mechanisms. *Soft Matter*. 2010;6:5196-5205
175. Tziampazis E, Kohn J, Moghe PV. Peg-variant biomaterials as selectively adhesive protein templates: Model surfaces for controlled cell adhesion and migration. *Biomaterials*. 2000;21:511-520
176. Jacques DA, Trewhella J. Small-angle scattering for structural biology--expanding the frontier while avoiding the pitfalls. *Protein science : a publication of the Protein Society*. 2010;19:642-657
177. Neylon C. Small angle neutron and x-ray scattering in structural biology: Recent examples from the literature. *European biophysics journal : EBJ*. 2008;37:531-541
178. Universe It. The electromagnetic spectrum. 2013;2016
179. B D, L L, B L, J T. The physics of computed tomography. 2006;2016
180. M R. Basics of x-ray scattering. 2009;2016
181. X Z, A G. Solution small angle x-ray scattering: Basic principles and experimental aspects. 2009;2016
182. Y A, Y S. Small-angle x-ray scattering basics & applications. 2010;2016
183. C S. Small angle x-ray scattering and diffraction.
184. Leung BO, Chou KC. Review of super-resolution fluorescence microscopy for biology. *Applied spectroscopy*. 2011;65:967-980
185. Gustafsson MG. Nonlinear structured-illumination microscopy: Wide-field fluorescence imaging with theoretically unlimited resolution. *Proceedings of the National Academy of Sciences of the United States of America*. 2005;102:13081-13086
186. Schermelleh L, Heintzmann R, Leonhardt H. A guide to super-resolution fluorescence microscopy. *The Journal of cell biology*. 2010;190:165-175
187. Schermelleh L, Carlton PM, Haase S, Shao L, Winoto L, Kner P, Burke B, Cardoso MC, Agard DA, Gustafsson MG, Leonhardt H, Sedat JW. Subdiffraction multicolor imaging of the nuclear periphery with 3d structured illumination microscopy. *Science*. 2008;320:1332-1336

188. Kner P, Chhun BB, Griffis ER, Winoto L, Gustafsson MG. Super-resolution video microscopy of live cells by structured illumination. *Nature methods*. 2009;6:339-342
189. Hirvonen LM, Wicker K, Mandula O, Heintzmann R. Structured illumination microscopy of a living cell. *European biophysics journal : EBJ*. 2009;38:807-812
190. Baddeley D, Chagin VO, Schermelleh L, Martin S, Pombo A, Carlton PM, Gahl A, Domaing P, Birk U, Leonhardt H, Cremer C, Cardoso MC. Measurement of replication structures at the nanometer scale using super-resolution light microscopy. *Nucleic acids research*. 2010;38:e8
191. Bittiger H, Marchessault RH, Niegisch WD. Crystal structure of poly-e-caprolactone. *Acta Crystallographica Section B*. 1970;26
192. Sung HJ, Su J, Berglund JD, Russ BV, Meredith JC, Galis ZS. The use of temperature-composition combinatorial libraries to study the effects of biodegradable polymer blend surfaces on vascular cells. *Biomaterials*. 2005;26:4557-4567
193. Du H, Chandaroy P, Hui SW. Grafted poly-(ethylene glycol) on lipid surfaces inhibits protein adsorption and cell adhesion. *Biochimica et biophysica acta*. 1997;1326:236-248
194. Kingshott P, Wei J, Bagge-Ravn D, Gadegaard N, Gram L. Covalent attachment of poly(ethylene glycol) to surfaces, critical for reducing bacterial adhesion. *Langmuir*. 2003;19:6912-6921
195. Burridge K, Chrzanowska-Wodnicka M. Focal adhesions, contractility, and signaling. *Annual review of cell and developmental biology*. 1996;12:463-518
196. Gardel ML, Schneider IC, Aratyn-Schaus Y, Waterman CM. Mechanical integration of actin and adhesion dynamics in cell migration. *Annual review of cell and developmental biology*. 2010;26:315-333
197. Geiger B, Bershadsky A, Pankov R, Yamada KM. Transmembrane crosstalk between the extracellular matrix--cytoskeleton crosstalk. *Nature reviews. Molecular cell biology*. 2001;2:793-805
198. Humphrey JD, Dufresne ER, Schwartz MA. Mechanotransduction and extracellular matrix homeostasis. *Nature reviews. Molecular cell biology*. 2014;15:802-812
199. Parsons JT, Horwitz AR, Schwartz MA. Cell adhesion: Integrating cytoskeletal dynamics and cellular tension. *Nature reviews. Molecular cell biology*. 2010;11:633-643
200. Lonza. Poietics (tm) human bone marrow- technical sheet. 2013
201. Horton ER, Astudillo P, Humphries MJ, Humphries JD. Mechanosensitivity of integrin adhesion complexes: Role of the consensus adhesome. *Exp Cell Res*. 2016;343:7-13
202. West JJ, Harris TJ. Cadherin trafficking for tissue morphogenesis: Control and consequences. *Traffic*. 2016
203. Mui KL, Chen CS, Assoian RK. The mechanical regulation of integrin-cadherin crosstalk organizes cells, signaling and forces. *Journal of cell science*. 2016;129:1093-1100
204. Lecuit T, Yap AS. E-cadherin junctions as active mechanical integrators in tissue dynamics. *Nature cell biology*. 2015;17:533-539

205. Deskins DL, Bastakoty D, Saraswati S, Shinar A, Holt GE, Young PP. Human mesenchymal stromal cells: Identifying assays to predict potency for therapeutic selection. *Stem cells translational medicine*.2:151-158
206. Sung HJ, Yee A, Eskin SG, McIntire LV. Cyclic strain and motion control produce opposite oxidative responses in two human endothelial cell types. *Am J Physiol Cell Physiol*. 2007;293:C87-94
207. Ray R, Novotny NM, Crisostomo PR, Lahm T, Abarbanell A, Meldrum DR. Sex steroids and stem cell function. *Molecular medicine*. 2008;14:493-501
208. Dyce PW, Li D, Barr KJ, Kidder GM. Connexin43 is required for the maintenance of multipotency in skin-derived stem cells. *Stem Cells Dev*. 2014;23:1636-1646
209. Taniguchi Ishikawa E, Gonzalez-Nieto D, Ghiaur G, Dunn SK, Ficker AM, Murali B, Madhu M, Gutstein DE, Fishman GI, Barrio LC, Cancelas JA. Connexin-43 prevents hematopoietic stem cell senescence through transfer of reactive oxygen species to bone marrow stromal cells. *Proceedings of the National Academy of Sciences of the United States of America*. 2012;109:9071-9076
210. Robey PG, Kuznetsov SA, Ren J, Klein HG, Sabatino M, Stroncek DF. Generation of clinical grade human bone marrow stromal cells for use in bone regeneration. *Bone*. 2015;70:87-92
211. Fisher MB, Belkin NS, Milby AH, Henning EA, Soegaard N, Kim M, Pfeifer C, Saxena V, Dodge GR, Burdick JA, Schaer TP, Steinberg DR, Mauck RL. Effects of mesenchymal stem cell and growth factor delivery on cartilage repair in a mini-pig model. *Cartilage*. 2016;7:174-184
212. Russo V, Young S, Hamilton A, Amsden BG, Flynn LE. Mesenchymal stem cell delivery strategies to promote cardiac regeneration following ischemic injury. *Biomaterials*. 2014;35:3956-3974
213. Madonna R, Delli Pizzi S, Tartaro A, De Caterina R. Transplantation of mesenchymal cells improves peripheral limb ischemia in diabetic rats. *Molecular biotechnology*. 2014;56:438-448
214. Elseberg CL, Salzig D, Czermak P. Bioreactor expansion of human mesenchymal stem cells according to gmp requirements. *Methods Mol Biol*. 2015;1283:199-218
215. Ng CP, Sharif AR, Heath DE, Chow JW, Zhang CB, Chan-Park MB, Hammond PT, Chan JK, Griffith LG. Enhanced ex vivo expansion of adult mesenchymal stem cells by fetal mesenchymal stem cell ecm. *Biomaterials*. 2014;35:4046-4057
216. Duffy CR, Zhang R, How SE, Lilienkampf A, De Sousa PA, Bradley M. Long term mesenchymal stem cell culture on a defined synthetic substrate with enzyme free passaging. *Biomaterials*. 2014;35:5998-6005
217. Krause U, Seckinger A, Gregory CA. Assays of osteogenic differentiation by cultured human mesenchymal stem cells. *Methods Mol Biol*. 2011;698:215-230
218. Fink T, Zachar V. Adipogenic differentiation of human mesenchymal stem cells. *Methods Mol Biol*. 2011;698:243-251
219. Lieber CA, Mahadevan-Jansen A. Automated method for subtraction of fluorescence from biological raman spectra. *Applied spectroscopy*. 2003;57:1363-1367

220. De Gelder J, De Gussem K, Vandenabeele P, Moens L. Reference database of raman spectra of biological molecules. *Journal of Raman Spectroscopy*. 2007;38:1133-1147
221. Ujike T, Tominaga Y. Raman spectral analysis of liquid ammonia and aqueous solution of ammonia. *Journal of Raman Spectroscopy*. 2002;33:485-493
222. Ma S, Huang Q. A sers study of oxidation of glutathione under plasma irradiation. *RSC Advances*. 2015;5:57847-57852
223. Cassanas G, Morssli M, Fabrègue E, Bardet L. Vibrational spectra of lactic acid and lactates. *Journal of Raman Spectroscopy*. 1991;22:409-413
224. Pawlukojć A, Hołderna-Natkaniec K, Bator G, Natkaniec I. L-glutamine: Dynamical properties investigation by means of ins, ir, raman, 1h nmr and dft techniques. *Chemical Physics*. 2014;443:17-25
225. Carmona P, Molina M. Raman and infrared spectra of d-ribose and d-ribose 5-phosphate. *Journal of Raman Spectroscopy*. 1990;21:395-400
226. Zhu G, Zhu X, Fan Q, Wan X. Raman spectra of amino acids and their aqueous solutions. *Spectrochimica Acta Part A: Molecular and Biomolecular Spectroscopy*. 2011;78:1187-1195
227. Diaz Fleming G, Finnerty JJ, Campos-Vallette M, Célis F, Aliaga AE, Fredes C, Koch R. Experimental and theoretical raman and surface-enhanced raman scattering study of cysteine. *Journal of Raman Spectroscopy*. 2009;40:632-638
228. Czamara K, Majzner K, Pacia MZ, Kochan K, Kaczor A, Baranska M. Raman spectroscopy of lipids: A review. *Journal of Raman Spectroscopy*. 2015;46:4-20
229. Mendez-Ferrer S, Michurina TV, Ferraro F, Mazloom AR, Macarthur BD, Lira SA, Scadden DT, Ma'ayan A, Enikolopov GN, Frenette PS. Mesenchymal and haematopoietic stem cells form a unique bone marrow niche. *Nature*. 2010;466:829-834
230. Morikawa S, Mabuchi Y, Kubota Y, Nagai Y, Niibe K, Hiratsu E, Suzuki S, Miyauchi-Hara C, Nagoshi N, Sunabori T, Shimmura S, Miyawaki A, Nakagawa T, Suda T, Okano H, Matsuzaki Y. Prospective identification, isolation, and systemic transplantation of multipotent mesenchymal stem cells in murine bone marrow. *The Journal of experimental medicine*. 2009;206:2483-2496
231. Sacchetti B, Funari A, Michienzi S, Di Cesare S, Piersanti S, Saggio I, Tagliafico E, Ferrari S, Robey PG, Riminucci M, Bianco P. Self-renewing osteoprogenitors in bone marrow sinusoids can organize a hematopoietic microenvironment. *Cell*. 2007;131:324-336
232. Kobayashi CI, Suda T. Regulation of reactive oxygen species in stem cells and cancer stem cells. *Journal of cellular physiology*. 2012;227:421-430
233. Woodbury D, Schwarz EJ, Prockop DJ, Black IB. Adult rat and human bone marrow stromal cells differentiate into neurons. *Journal of neuroscience research*. 2000;61:364-370
234. Toma C, Pittenger MF, Cahill KS, Byrne BJ, Kessler PD. Human mesenchymal stem cells differentiate to a cardiomyocyte phenotype in the adult murine heart. *Circulation*. 2002;105:93-98
235. Sun Y, Li W, Lu Z, Chen R, Ling J, Ran Q, Jilka RL, Chen XD. Rescuing replication and osteogenesis of aged mesenchymal stem cells by exposure to a young extracellular matrix. *FASEB J*. 2011;25:1474-1485

236. Tan J, Xu X, Tong Z, Lin J, Yu Q, Lin Y, Kuang W. Decreased osteogenesis of adult mesenchymal stem cells by reactive oxygen species under cyclic stretch: A possible mechanism of age related osteoporosis. *Bone research*. 2015;3:15003
237. Wilson A, Shehadeh LA, Yu H, Webster KA. Age-related molecular genetic changes of murine bone marrow mesenchymal stem cells. *BMC genomics*. 2010;11:229
238. Gentleman E, Swain RJ, Evans ND, Boonrungsiman S, Jell G, Ball MD, Shean TA, Oyen ML, Porter A, Stevens MM. Comparative materials differences revealed in engineered bone as a function of cell-specific differentiation. *Nat Mater*. 2009;8:763-770
239. Autefage H, Gentleman E, Littmann E, Hedegaard MA, Von Erlach T, O'Donnell M, Burden FR, Winkler DA, Stevens MM. Sparse feature selection methods identify unexpected global cellular response to strontium-containing materials. *Proceedings of the National Academy of Sciences of the United States of America*. 2015;112:4280-4285
240. Kiss-Laszlo Z, Henry Y, Kiss T. Sequence and structural elements of methylation guide snornas essential for site-specific ribose methylation of pre-rrna. *The EMBO journal*. 1998;17:797-807
241. Fillmore N, Huqi A, Jaswal JS, Mori J, Paulin R, Haromy A, Onay-Besikci A, Ionescu L, Thebaud B, Michelakis E, Lopaschuk GD. Effect of fatty acids on human bone marrow mesenchymal stem cell energy metabolism and survival. *PLoS One*. 2015;10:e0120257
242. Chen DF, Zhang HL, Du SH, Li H, Zhou JH, Li YW, Zeng HP, Hua ZC. Cholesterol myristate suppresses the apoptosis of mesenchymal stem cells via upregulation of inhibitor of differentiation. *Steroids*. 2010;75:1119-1126
243. Kim N, Im KI, Lim JY, Jeon EJ, Nam YS, Kim EJ, Cho SG. Mesenchymal stem cells for the treatment and prevention of graft-versus-host disease: Experiments and practice. *Ann Hematol*. 2013;92:1295-1308
244. Le Blanc K, Frassoni F, Ball L, Locatelli F, Roelofs H, Lewis I, Lanino E, Sundberg B, Bernardo ME, Remberger M, Dini G, Egeler RM, Bacigalupo A, Fibbe W, Ringden O, Developmental Committee of the European Group for B, Marrow T. Mesenchymal stem cells for treatment of steroid-resistant, severe, acute graft-versus-host disease: A phase ii study. *Lancet*. 2008;371:1579-1586
245. Bartosh TJ, Ylostalo JH. Preparation of anti-inflammatory mesenchymal stem/precursor cells (mscs) through sphere formation using hanging-drop culture technique. *Curr Protoc Stem Cell Biol*. 2014;28:Unit 2B 6
246. Bartosh TJ, Ylostalo JH, Bazhanov N, Kuhlman J, Prockop DJ. Dynamic compaction of human mesenchymal stem/precursor cells into spheres self-activates caspase-dependent il1 signaling to enhance secretion of modulators of inflammation and immunity (pge2, tsg6, and stc1). *Stem Cells*. 2013;31:2443-2456
247. Zimmermann JA, McDevitt TC. Pre-conditioning mesenchymal stromal cell spheroids for immunomodulatory paracrine factor secretion. *Cytotherapy*. 2014;16:331-345
248. Potapova IA, Gaudette GR, Brink PR, Robinson RB, Rosen MR, Cohen IS, Doronin SV. Mesenchymal stem cells support migration, extracellular matrix

invasion, proliferation, and survival of endothelial cells in vitro. *Stem Cells*. 2007;25:1761-1768
249. Sart S, Tsai AC, Li Y, Ma T. Three-dimensional aggregates of mesenchymal stem cells: Cellular mechanisms, biological properties, and applications. *Tissue engineering. Part B, Reviews*. 2014;20:365-380
250. Chan HF, Zhang Y, Ho YP, Chiu YL, Jung Y, Leong KW. Rapid formation of multicellular spheroids in double-emulsion droplets with controllable microenvironment. *Sci Rep*. 2013;3:3462
251. Han HW, Hsu SH. Chitosan-hyaluronan based 3d co-culture platform for studying the crosstalk of lung cancer cells and mesenchymal stem cells. *Acta biomaterialia*. 2016
252. Yeh HY, Liu BH, Sieber M, Hsu SH. Substrate-dependent gene regulation of self-assembled human msc spheroids on chitosan membranes. *BMC genomics*. 2014;15:10
253. Zachman AL, Crowder SW, Ortiz O, Zienkiewicz KJ, Bronikowski CM, Yu SS, Giorgio TD, Guelcher SA, Kohn J, Sung HJ. Pro-angiogenic and anti-inflammatory regulation by functional peptides loaded in polymeric implants for soft tissue regeneration. *Tissue engineering. Part A*.19:437-447
254. Poole KM, Tucker-Schwartz JM, Sit WW, Walsh AJ, Duvall CL, Skala MC. Quantitative optical imaging of vascular response in vivo in a model of peripheral arterial disease. *Am J Physiol Heart Circ Physiol*.305:H1168-1180
255. Frangi AF, Niessen WJ, Vincken KL, Viergever MA. Multiscale vessel enhancement filtering. *Medical Image Computing and Computer-Assisted Intervention - Miccai'98*. 1998;1496:130-137
256. Canny J. A computational approach to edge-detection. *Ieee Transactions on Pattern Analysis and Machine Intelligence*. 1986;8:679-698